FACULDADE DE ENGENHARIA DA UNIVERSIDADE DO PORTO
INSTITUTO DE CIÊNCIAS BIOMÉDICAS ABEL SALAZAR DA UNIVERSIDADE DO PORTO


# Establishment of an Experimental Protocol for Assessing the Transport of Nanoparticles in Breast Cancer Spheroids

Marta Isabel Miguel de Miranda e Amaral de Avelar

Dissertation carried out under the Master's Degree in Bioengineering
Molecular Bioengineering

Supervisor: José das Neves, PhD

15th September 2022

# Resumo

O rastreamento de múltiplas partículas (MPT) é uma técnica que permite que o movimento de um grupo de partículas seja mapeado em tempo real e de forma individual em matrizes biológicas. A técnica fornece informação sobre que formulações de nanopartículas (NPs) são as mais eficazes para a penetração de tecidos, o que pode ter um impacto significativo no desenvolvimento de novas terapias.

Neste trabalho, o transporte de NPs (sem revestimento ou com poloxâmero) foi investigado em esferóides de cancro da mama compostos por células MCF-7, após diferentes tempos de incubação. Antes da análise por MPT, foi avaliada a viabilidade dos esferóides após congelação, bem como as caraterísticas das NPs. As partículas mantiveram o tamanho e carga de superfície ao longo de 5 dias, com valores de polidispersão que não ultrapassavam 0,1. Os ensaios de viabilidade foram realizados seguindo várias metodologias de congelamento, mas mantendo a compatibilidade do processo com a técnica de criosecção. Nenhuma das técnicas permitiu manter a viabilidade inicial do esferóide, com valores relativos abaixo dos 35% iniciais. Deste modo, a abordagem mais simples (isto é, incorporar os esferóides num composto de incorporação antes de serem colocados no crióstato e congelados) foi escolhida para proceder à criosecção dos esferóides e posterior execução de análise por MPT.

Devido à fraca viabilidade após congelamento, a avaliação do transporte de NPs foi conduzida em esferóides completos, isto é, sem congelamento prévio ou secção do mesmo. Porém, a interferência causada pela presença de várias camadas de células no percurso ótico não permitiu a aquisição de um número suficiente de trajetórias válidas para análise. Os resultados para os esferóides e criosecções foram semelhantes: as NPs incubadas por menos tempo com a matriz biológica evidenciaram um transporte mais desimpedido. De forma inesperada, as partículas sem revestimento apresentaram-se como mais móveis do que as revestidas com poloxâmero, e com um comportamento semelhante à de NPs revestidas de modo covalente com polietilenoglicol. Estes dados contrariam investigações anteriores conduzidas por outros investigadores em que se avaliou o movimento de partículas noutras matrizes biológicas complexas. O uso de criosecções permitiu ainda avaliar a mobilidade das NPs em diferentes camadas do esferóide. Os resultados sugerem que, para menores tempos de incubação, as NPs possuem maior mobilidade na zona nuclear dos esferóides do que nas mais periféricas.

Em conclusão, foi desenvolvido um protocolo que utiliza a técnica de MPT em matrizes biológicas complexas, nomeadamente esferóides. A metodologia desenvolvida permite obter informação relevante que pode ser útil para o desenvolvimento de NPs terapêuticas.

*(Page purposefully left blank)*

# Abstract

Multiple particle tracking (MPT) is a technique that allows for individual particles to be traced in complex biological matrices. It provides information on which formulations of nanoparticles (NPs) are most effective for tissue penetration, which may significantly impact the development of new therapeutics.

In this work, breast cancer spheroids comprised of MCF-7 cells were assessed for transport of bare and poloxamer-coated NPs with distinct incubation times. Before MPT analysis, the viability of spheroids after freezing was determined, as well as the characteristics of the NPs. These last were found to maintain size and surface charge over a 5-day period, with polydispersity index values below 0.1. Viability studies were performed after freezing spheroids through various methodologies while maintaining compatibility with the frozen section procedure. All tested variations to the freezing process had a significant impact on cell viability, reducing it to less than 35% of initial values. Thus, the simplest approach (i.e. simply placing the spheroids in embedding medium and transferring them into the cryostat for freezing) was chosen for cryosectioning spheroids before MPT analysis.

Due to the negative impact of freezing on spheroid viability, we also attempted to evaluate NP transport in whole spheroids, without freezing or sectioning. However, the low signal-to-noise ratio caused by the presence of multiple cell layers in the optical path did not allow for sufficient acquisition of valid trajectories for analysis. Results for whole and cryosectioned spheroids were similar: NPs with shorter incubation times with the biological matrix evidenced enhanced unhindered transport. Surprisingly, bare NPs were also found to be more mobile than those with poloxamer coating, and in the range of that found for NPs coated covalently with polyethylene glycol. These results contrast with previous data obtained by others evaluating the movement of similar particles in other complex biological matrices. Cryosectioning also allowed for the assessment of NP transport in different sections of the spheroid. In particular, NPs appeared to denote higher mobility at the core of the spheroids when incubated for shorter time periods.

Overall, a protocol was developed for the use of MPT in the analysis of NP transport in complex biological matrices, such as spheroids. The methodology enables the generation of relevant information that can be further used for developing new therapeutic NPs.

**Keywords:** Multiple Particle Tracking; Nanomedicine; Biotechnology; Transport Mode.

*(Page purposefully left blank)*

# Acknowledgements

First, I would like to thank my supervisor, Dr. José das Neves, and group leader Prof. Bruno Sarmento for accepting me as a master student to the research group of Nanomedicine and Translational Drug Delivery at i3S. Many thanks to this group, for welcoming me to their lab, mentoring me in various concepts, and their constant willingness to help. Thank you for listening to my panicked babbling, and providing different perspectives for new approaches to my work.

A sincere acknowledgement to i3S, FEUP and ICBAS for providing this opportunity through the masters in bioengineering (former integrated masters in bioengineering). My profound gratitude to the various professors who, throughout the years, not only fulfilled their teaching capacity, but also awakened a thirst for more knowledge and greater scientific curiosity.

A special thanks to Dr. José das Neves, for all the questions and emails answered, even during weekends, holidays, or vacation time. For the numerous hours-long meetings where despite little results being shown, was always available to provide new insights and ideas, solutions for problems I did not even think about.

Another special thanks to Helena, the person who taught me everything about MPT, the basis of this thesis. All the computer programs she explained to me (time and time again…), the questions she consistently knew the answers to, the hours spent in front of my computer (sometimes just to try to understand why the scale bars aren't working), the anxiety she calmed…

I would also like to thank my family, for all their love and support, every weekend or vacation where they gave me the space and time I needed to work on this thesis. My siblings, for taking my share of the housework, and my parents, for listening attentively to my ramblings about concepts that they were not familiar with.

And, last but not least, a major thanks to my friends, who are in the same boat as me, but were always able to make me wind down, relax, and laugh. I think I would have broken down without these random encounters through i3S, which always managed to happen exactly when I needed them the most.

Thank you, everyone. I could not have done this without your help and support.

*(Page purposefully left blank)*

*“It does not matter how slowly you go*
*as long as you do not stop”*

**-Confucius**

*(Page purposefully left blank)*

# Contents

# List of Figures

# List of Tables

# Abbreviations

| | |
|---|---|
| BC | Breast Cancer |
| BCSS | Breast Cancer-Specific Survival |
| BO | Before Observation |
| DDS | Drug Delivery System |
| DLS | Dynamic Light Scattering |
| DMEM/F-12 | Dulbecco's Modified Eagle Medium/Nutrient Mixture F-12 |
| DMSO | Dimethyl Sulfoxide |
| ECM | Extracellular Matrix |
| e.g. | *Exempli gratia* – for example |
| ELS | Electrophoretic Light Scattering |
| FBS | Fetal Bovine Serum |
| FCS | Fluorescence Correlation Spectroscopy |
| FFPE | Formalin-Fixed Paraffin-Embedded |
| FRAP | Fluorescence Recovery After Photobleaching |
| GLYC | Glycerine |
| HER2 | Human Epidermal Growth Factor Receptor 2 |
| i.e. | *Id est* – that is |
| IPOH | Isopropanol |
| LC-MS | Liquid Chromatography Coupled to Tandem Mass Spectrometry |
| MALDI-MSI | Matrix Assisted Laser Desorption/Ionization Mass Spectrometry Imaging |
| MCF-7 | Michigan Cancer Foundation-7 |
| MCTS | Multicellular Tumour Spheroids |
| MPT | Multiple Particle Tracking |
| MSD | Mean Square Displacement |
| MW | Molecular Weight |
| NP | Nanoparticle |
| OCT | Optimum Cutting Temperature Compound |
| P407 | Poloxamer 407 |

| | |
|---|---|
| PBS | Phosphate-Buffered Saline |
| PdI | Polydispersity Index |
| PEG | Polyethylene Glycol |
| PLGA | Poly(Lactic-co-Glycolic) Acid |
| PPG | Poly(Propylene Glycol) |
| PS | Polystyrene |
| PVA | Polyvinyl Alcohol |
| RLU | Relative Light Units |
| RT | Room Temperature |
| SD | Standard Deviation |
| SPT | Single Particle Tracking |
| SS | Since Seeding |
| TME | Tumour Microenvironment |
| TRE | Trehalose |

# List of Symbols and Variables

| | |
|---|---|
| $\alpha$ | Anomalous Diffusion Exponent |
| $\eta$ | Dynamic Viscosity of a Fluid |
| $D_0$ | Time-Independent Diffusion Coefficient |
| $D_{eff}$ | Effective Diffusivity |
| $D_W$ | Theoretical Diffusivity of Spherical Particles in Water |
| $k_B$ | Boltzmann Constant |
| r | Particle Position |
| R | Particle Hydrodynamic Radius |
| $\tau$ | Lag Time |
| t | Time |
| T | Absolute Temperature |
| $t_{trajectory}$ | Total Duration of the Trajectory |

# Chapter 1. Introduction

Multiple Particle Tracking (MPT) is a technique that allows for time resolved determination of the motion of particles in different media, including biological samples. Previous work found that it can analyse particle transport in native mucus and surrogates [1], as well as more complex environments such as brain tissue [2, 3] and breast tumours [4]. Understanding the behaviour of NPs in complex media can be crucial for effective therapies to be developed [5].

Cancer is the second leading cause of death worldwide, with breast being the most common cancer in 2020, and the fifth most lethal [6]. Alongside the available therapeutic armamentarium, new therapeutic approaches are being developed, several of them based on the use of nanoparticles (NPs) as drug carriers [7]. One of the most common platforms for drug testing is spheroids, as their 3D nature can mimic distinct cellular profiles found in tumours: the border represents the proliferative cells, the inner layer the quiescent cells, and the centre the necrotic core [8]. These differing environments may impact penetration of molecules, including therapeutic ones, and can alter the effectiveness of treatment regimens.

For effective treatment, NPs must behave as they are expected. Previous research using MPT analysis showed that the use of a dense coating of NPs with polyethylene glycol (PEG) – also referred to as dense PEGylation – may enhance their movement in tumours [2]. However, discrete measurement of tumour penetration suggests the opposite [9]. No previous work assessed time resolved transport of NPs in spheroids, merely their penetration [9, 10]. This leaves a large knowledge gap in NP application for cancer treatment.

## 1.1 Objective

This work aims to develop and validate a protocol capable of characterizing NP transport in complex biological matrices, namely breast cancer spheroids, using MPT analysis. Another objective was to determine the impact of the coating of NPs and their incubation time with the biological matrix on the transport of particles, including at distinct spheroid layers.

## 1.2 Document Organization

This dissertation comprises five chapters. The first presents the rationale of the work, as well as its objectives and how it is organized. Next, a literature review of relevant concepts and techniques is included, namely regarding methodologies that assess particle transport (with special emphasis on MPT), as well as protocols for tissue processing, focusing on cryosectioning. The materials used, as well as the different methodologies followed, are detailed in the third chapter. The results obtained, and their discussion, can be found in chapter four. Finally, chapter five contains the overall conclusions of this dissertation, as well as possible future work derived from this one.

# Chapter 2. Literature Review

## 2.1 Nanoparticle Transport Through Biological Samples

For years, nanotechnology-based approaches have been regarded as promising for the treatment of multiple diseases [11]. NPs are common in drug delivery and nanomedicine, due to the capability of encapsulating drugs and increasing their bioavailability and efficacy [12], despite reducing adverse effects and being less likely to induce drug resistance [13]. Additionally, they are an interesting venue due to the impact size, surface charge, coating and shape have on cellular uptake, biodistribution, elimination and target accumulation [14, 15]. Moreover, the deposition of a protein corona on the surface of the NPs may completely alter its properties and how it interacts with the surrounding environment, either guiding or hiding the particle from the target [16]. At the moment, various NP-based formulations are already available as treatment options for different pathologies, such as Doxil™, Lipoplatin™ and Abraxane™ [17], while numerous others are in clinical trials, mostly for cancer applications [7].

Despite the possibility of targeting specific organs, tissues or cells depending on the properties of nanoparticles, it is necessary to determine how they also affect the penetration of the intended biological matrix and/or cellular internalization, as it could have a significant impact on effective drug delivery [5]. For example, a study established that smaller gold NPs (2 nm) were more internalized in MCF-7 monolayers [18]. Yet, when assessing more complex biological matrices, particles around 2-6 nm in diameter stayed longer in MCF-7 spheroids and blood, and reached the tumour in greater quantities. Thus, depending on the desired effect of such therapeutic agent, the ideal size of the NP could vary.

One of the most common NP modifications is the coating with PEG, which creates a hydrated cloud that makes thermodynamically unfavourable associations that could alter this cloud, therefore precluding interactions with other nanoparticles or blood components, such as serum proteins [19]. Thus, PEG may hinder, or at least delay, the formation of a protein corona on the stealth NPs [20]. Moreover, when there is a dense coating of 5-20 kDa PEG molecules that guarantees a neutralization of the zeta potential, these particles are not only characterized as stealth, but also mucus-penetrating if their diameter does not surpass around 500 nm [21]. This process, PEGylation, could be performed by either covalent attachment of the PEG molecules to the nanocarrier surface or simply by adsorption [22]. PEGylation leads to an increase in the circulation half-life and stability of the nanocarriers, and may decrease their

toxicity [23]. Additionally, it is important to note that the characteristics of this process may also affect the behaviour of the nanocarriers.

As aforementioned, a dense coating of nanocarriers with PEG chains has been shown to increase their penetration in mucus, a biological barrier present at mucosae that is capable of trapping and removing most of the pathogens and nanoparticles it comes into contact with, either sterically or through electrostatic and hydrophobic interactions [24]. This has been established for fresh, undiluted human cervicovaginal mucus [25], fresh, undiluted human cystic fibrosis sputum [26], and different mucus surrogates [1], through NPs in the range of 100 nm (or less) and 500 nm in diameter, which could cross mucus in a nearly diffusive fashion.

However, the same was not true for more complex biological matrices, such as cells and spheroids. This was verified when Fujii and co-workers assessed the movement of NPs incubated for 3 hours in mouse and human colon cancer spheroids [9]. They determined that PEGylated NPs were incapable of penetrating spheroids, being found only at their border, whereas particles coated with zwitterionic betaine polymers or a positively charged polymer could be found throughout the spheroids. Even still, some of the zwitterionic polymers were not effective in improving NP transport. When attempting a coating composed largely of PEG with merely 10% of zwitterionic or positively charged polymers, it was shown that only poly(carboxybetaine methacrylate) could increase NP penetration, with greater particle concentration on the border and centre of the spheroids. Nonetheless, although PEG-NPs were neutrally charged, no information was available regarding the molecular weight (MW) of PEG nor its surface density. Previously, Ramamurthi *et al*. described that an increase in hydrophobic components in PEG-derived polymers in the coating of 40 nm polymeric particles contributed to DLD-1 spheroid penetration, as well as mice organ (e.g., spleen, liver) and tumour uptake [10]. On the contrary, some extent of hydrophilic elements in the NPs increased cellular internalization when these cells were in a monolayer and caused greater tumour deposition over time. Once more, though the surface charge of the NPs was around 0 mV, no data was found concerning the density of the coating. Therefore, the distinct NP transport in mucus and spheroids may be because, in these instances, stealth NPs were assessed instead of mucus penetrating particles.

There are multiple limitations to the PEGylation approach, such as: (1) the PEGylation process must be optimized to attain the desired prolonged circulation or increased mucus penetration with maintenance of therapeutic action; (2) the non-biodegradability and poor excretion of higher MW PEG molecules through the kidneys, which leads to accumulation in the liver; (3) the increase in size caused by PEGylation may induce greater uptake into the reticuloendothelial system, therefore accelerating drug release; (4) while there is an increase in mucus transport for mucus penetrating particles, intracellular uptake is adversely impacted; (5) PEG has been known to be immunogenic, thus inducing antibody production and consequent clearance of the therapeutic agent at a rate that limits its efficiency [27]. Moreover, there have been reports that PEGylation may fail in the presence of environments rich in proteins after a few hours [28], which may clarify the poor tissue penetration described previously.

Indeed, Perera *et al*. established that 15 nm gold NPs coated with PEG could still have adsorption of various peptides, especially when using higher MW PEG (i.e., MW = 30 kDa) that formed a ‘mushroom’ conformation [28]. As a matter of fact, after approximately 25 hours in the presence of the peptides, the maximum adsorption was already reached for all MW PEG molecules. Despite the low quantities adsorbed, it is possible that it may affect how the drug delivery system (DDS) interacts with cells. The same was observed using 250 nm nanocapsules in human plasma for 1 hour, i.e., a ‘brush’ conformation was preferential for stealth behaviour

and the reduction of cellular internalization [29]. Furthermore, it was also observed that PEG surface density and MW would influence which proteins adhered to the DDS surface. Another study described similar findings using poly(lactic-co-glycolic acid) (PLGA) and PLGA-PEG NPs, with 100 or 200 nm diameter, incubated in fetal bovine serum (FBS) for 30 min [30]. Altogether, the presence of PEG drastically decreased the adsorption of FBS components to the NPs, mostly of proteins with a mass over 118 kDa and, surprisingly, proteins involved in immunoregulatory processes, namely complement factors. However, none of these works evaluated mucus penetrating particles, only those with stealth coatings, something that was confirmed by the lack of neutral surface charge [28, 30] or the low MW of the PEG molecules [29].

### 2.1.1 Multiple Particle Tracking

Despite the observation of the penetration of NPs in tissues described above [9, 10], the techniques employed only allowed for the visualization of the particles at discrete time-points, not the time resolved assessment of their transport. However, there are various techniques available that can appraise the characteristics of particle movement, such as fluorescence recovery after photobleaching (FRAP), fluorescence correlation spectroscopy (FCS), dynamic light scattering (DLS), and MPT [1, 31]. These allow for greater information to be obtained: the identification of barriers to the particle diffusion in our sample, for example, or even the determination of the best surface characteristics in order to facilitate the desired movement of the particles [32].

In FRAP, the sample is first irradiated with a low-intensity laser to measure fluorescence, and then with a high-power beam to induce photobleaching [31]. Following a decrease in the illumination intensity, intact fluorophores diffuse back to the initial area, causing the rate of fluorescence recovery to be associated with their diffusivity. If molecules are immobile, they cannot recover to their initial fluorescence, which is detected and allows the inference of immobile particles as well. FRAP is widely available and has various possible modifications for the molecule of interest [33]. Nonetheless, it is difficult to assess the intrinsic fluorescence of the compounds and whether the movement of the sample is Brownian or not. The Brownian motion is one of the forces in a colloidal system, caused by the thermal motion of the medium, and is considered a diffusive process with random movement [34].

With FCS, a stationary laser beam will guarantee that only light from the focal spot is able to reach de detector for visualization [35]. Fluorescence variations are detected with high sensitivity and temporal resolution, which provides information about the timeframe between a particle entering and leaving the illuminated region. Therefore, an increase in NP mobility will result in brisker fluctuations. Although FCS experiments are relatively simple to perform, it still requires a very small volume with little particles, hence leading to long acquisition times [35, 36]. Furthermore, the small timespan that NPs are visible usually compels the observation of hundreds or thousands of particles.

Probably the most common technique for the assessment of particle size, DLS is fast, low-cost and non-invasive, and is capable of measuring the size of particles in solutions [37]. The fluctuations in the scattering intensity of a visible light laser will be dependent on the movement of the particles inside the sample and allow the determination of their mobility.

MPT, also referred to as single particle tracking (SPT), traces the movement of each individual particle in biological matrices, providing real-time information of particle transport, with an epifluorescence microscope [38]. Although the resolution of microscopes used in MPT

is at times not enough to observe the exact position of the NP, its location can be determined by finding the centre of the diffraction-limited spot [39, 40]. The positions are then linked into trajectories, following a function that calculates them assuming that they have Brownian motion, by choosing a link that minimizes the square distances of all particles [39]. This can provide information such as the mean square displacement (MSD) of the particles, a stepping stone to calculate other variables.

While there are microscopes capable of tracking the movement of particles in three dimensions, MPT is usually carried out using 2D microscopes, where the trajectories are the 2D projection of the 3D motion of the particles [41]. Fortunately, the 2D and 3D diffusion coefficients are equal if the biological matrix analysed is locally isotropic, even if not homogeneous [40, 42]. This gives rise to 2 consequences: (1) videos can be attained with acquisition time periods (a few milliseconds) that provide great temporal resolution while guaranteeing high spatial resolution in all dimensions; (2) even if the medium being assessed is heterogeneous, as long as it is locally isotropic, MPT is a viable strategy to calculate NP transport [42]. For instance, despite mucus being considered potentially anisotropic [43], in the scales at which tracing is performed, one may consider it as being isotropic [44]. A similar analysis has been made for other heterogeneous biological matrices – e.g., cytoplasm [45], brain tissue [2, 3], and tumoral tissue [2-4] – and could be applied to even more matrices, such as other tissues, or even spheroids.

MPT imparts a wealth of information about the movement of NPs. One such case is the time-averaged MSD (<MSD>), or ensemble MSD, calculated according to equation 1,

$$<MSD> = \langle \Delta r^2(\tau) \rangle = \langle [r(t+\tau) - r(t)]^2 \rangle \quad (1)$$

where $\tau$ is the lag time (time interval for which the particle movement is calculated), $r$ is the particle position at the time $t$, and the brackets relay an average [46]. Thus, MSD is the squared distance traversed by a particle in a given timeframe. While analysing the movement of NPs, it is usually measured in $\mu m^2$.

When considering a two-dimensional displacement, MSD can also provide information about the anomalous diffusion exponent ($\alpha$), according to:

$$MSD = 4D_0 t^{\alpha} \quad (2)$$

where $D_0$ is the time-independent diffusion coefficient, or the diffusivity of a particle that has simple diffusion and is usually presented in $\mu m^2.s^{-1}$. MPT, as established above, is included in such types of displacement due to the isotropic nature of biological media.

The aforementioned $\alpha$ can then be used to characterize the transport mode of particles, as depicted in Table 1. Figure 1 showcases the association between the anomalous exponent and the typical trajectories of NPs.

**Table 1** - Classification of the transport mode of particles according to their anomalous diffusion exponent [1].

| Transport Mode | $\alpha$ |
|---|---|
| Immobile | 0.000-0.199 |
| Sub-diffusive | 0.200-0.899 |
| Diffusive | 0.900-1.199 |
| Active | >1.200 |

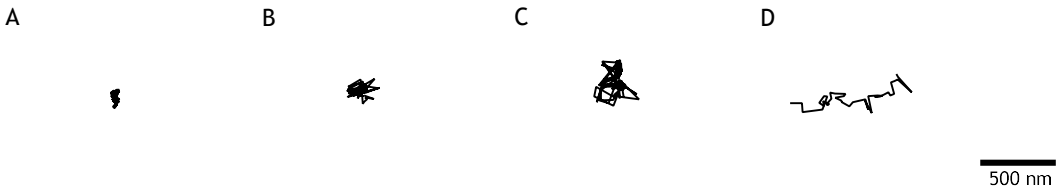


**Figure 1** - Representative portrayal of typical (A) immobile, (B) sub-diffusive, (C) diffusive and (D) active NP trajectories. Bar = 500 nm.

The MSD may also be used to calculate the effective diffusivity ($D_{eff}$) of particles in a simple viscous liquid, according to the following equation:

$$D_{eff} = \frac{MSD}{2n\tau} \tag{3}$$

where $n$ is the dimensionality (e.g., $n$ = 2 in two-dimensional systems) [46]. The effective diffusivity can also be compared to the theoretical diffusivity of spherical particles in water ($D_W$) for further detail. $D_W$ is the diffusivity of particles when they have a Brownian motion, as predicted by the Stokes-Einstein equation:

$$D_w = \frac{k_B T}{6\pi\eta R} \tag{4}$$

where $T$ is the absolute temperature, $k_B$ the Boltzmann constant, $\eta$ the fluid viscosity and $R$ the hydrodynamic radius of the particle (assuming a perfect sphere). The ratio between the theoretical and effective diffusivity, $D_W/D_{eff}$, provides information about how much the transport of the particle is slowed in a medium as compared to its theoretical movement in water.

Overall, MPT provides a wide variety of data, which enables the user to characterize diverse aspects of particle transport (Figure 2). These aspects are related and, based on the previous equations, more immobile particles (smaller anomalous exponent) will result in a decrease in MSD, which in turn causes a reduction in $D_{eff}$ and, therefore, an increase in the diffusivity ratio.

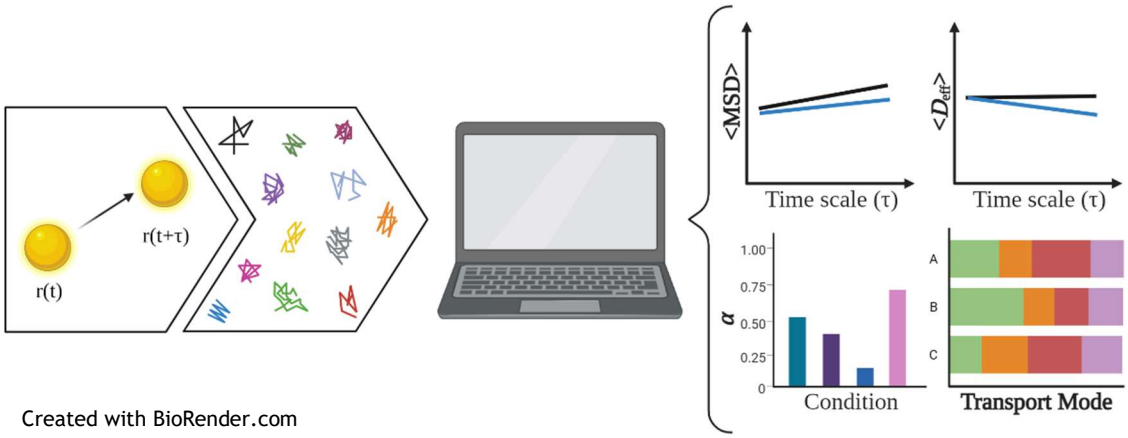


**Figure 2** - Schematic representation of MPT. Video with the movement of the NPs is analysed using software, in order to extract information about particle transport, such as <MSD>, <$D_{eff}$>, anomalous exponent and transport mode. Based on Avoiding a Sticky Situation: Bypassing the Mucus Barrier for Improved Local Drug Delivery, Zierden *et al.* [24].

Beyond particle tracking, MPT has many other applications, such as assessing the microrheology of biological samples [47], alterations to the biological matrix [48, 49] and pathogen mobility [50], among many others. It also has multiple benefits, the greatest of which is the ability to evaluate the movement of individual particles [39]. Additionally, and despite only assessing movement in two dimensions, particles may be 'recognized' if they leave and return to frames in a short interval (defined by the user), instead of being categorized as new particles. Furthermore, it is also possible to set a threshold for a minimum number of frames a particle must be present on, which discards non-essential data from the results.

Despite the multiple applications and advantages of MPT, this technique also has various limitations. For one, particle concentration must be sparse, in order to guarantee that NPs are not close enough for it to impact accuracy [51]. Moreover, there is an inherent bias against mobile particles, as they could leave the observed plane, while immobile NPs remain in the focal plane, impacting the <MSD> (and, therefore, all the variables calculated through it) [52]. If the sample is improperly prepared, there may exist drifting of the sample itself, which exaggerates the MSD. This variable can also be inflated due to the existence of static errors, attributable to microscope settings and capability of particle detection [53]. Lastly, the acquisition time has to be optimized, to allow sufficient sample irradiation to guarantee spatial accuracy, while minimizing dynamic errors - i.e., if the acquisition time is too long, then it is not the position of the particle that is determined, but, instead, its time-averaged position [52, 53].

Nonetheless, MPT is a truly relevant analysis, as it can detect if there are any alterations in particle transport caused by simply varying the characteristics of the NPs, the biological matrix, or even the protocol used. For instance, Crater *et al.* and Gabriel *et al.* found that carboxylated polystyrene (PS) NPs around 200 nm diameter had a nearly diffusive mode of transport in a mucus surrogate comprised of a mucin dispersion in phosphate-buffered saline (PBS) at 30 mg/mL [1, 54]. Both studies had similar values of anomalous exponent and diffusivity ratio, with the former having $\alpha$ = 0.81 and $D_W/D_{eff}$ = 11.6, and the latter $\alpha$ = 0.88 and $D_W/D_{eff}$ = 5.8, respectively. On the other hand, when evaluating the transport of NPs in cervicovaginal mucus, Hoang *et al.* determined that the bacterial composition of the cervicovaginal

mucus would greatly impact NP and HIV transport [55]. Certainly, mucus from patients with bacterial vaginosis had an increase in the mobility of both PEGylated and bare 100 nm PS NPs, as well as HIV virions, compared to samples with lower pH. Consequently, this study discovered that cervicovaginal microbiota with less *Lactobacillus crispatus* would enhance NP and HIV penetration, which could heighten the risk of HIV infection.

Similarly to what was established in mucus, it was recognized that densely PEGylated NPs with a hydrodynamic diameter around 100 nm also had increased transport in the cell cytoplasm [45]. Indeed, after microinjection of coated and uncoated particles into HeLa cells, NPs with PEG were more diffusive than those that remained bare, leading to the doubling of the average diffusivities. Dancy *et al*. found that dense coatings with low MW PEG enhanced the penetration of NPs in tumoral tissue [4]. In fact, when studying the behaviour of coated and non-coated NPs in MDA-MB-231 breast tumour slices from mice xenografts, both *ex vivo* and *in vivo*, PEGylated particles achieved further permeation than their uncoated counterparts. These results were also translated to brain tissue, as PEG-coated NPs were over 100 times more diffusive in 9L gliosarcoma, guaranteeing a greater, quicker and more homogeneous distribution compared to non-coated NPs [3]. Moreover, it was possible to determine that this tumoral tissue by itself is already more difficult for particles to move in as compared to normal brain tissue. Consequently, these investigations indicate that dense PEGylation of NPs is a viable approach in order to enhance transport inside cells, tissues and tumours.

Surprisingly, the MPT results for analysis of PEG-coated NPs in tissue were the opposite of what was found when assessing strictly the penetration of the particles after a set timeframe [3, 4, 9, 10]. This may be due to the PEGylation protocols used, as the latter studies had charged NPs despite the PEG layer (thus indicating only sparse coating), whereas reports utilizing the MPT technique were all neutral or near-neutral in surface charge. This could suggest that, for PEG-NPs to be able to be more mobile in tissue, the PEGylation protocol must guarantee the neutralization of the zeta potential of NPs (indicative of dense coating with PEG). Simply put, it is possible that a stealth coating is not sufficient for PEGylation to enhance NP transport in biological matrices - it has to comply with the characteristics of mucus-penetrating particles.

## 2.2 Breast Cancer

Cancer is the second leading cause of death in the world, with almost 10 million deaths in 2020 [6]. That year, there were more than 19 million new cases of cancer, over 2 million of which were female breast cancer (BC). Indeed, BC was, at that time, the most common cancer worldwide, surpassing lung cancer, with 11.7% of new cancer diagnoses in both sexes. It was also the fifth most lethal cancer, with nearly 685 thousand deaths (almost 7% of all cancer deaths). In women, it was both the most prevalent and mortal cancer type. Both incidence and mortality of BC have been increasing since 1990 [56], a trend that is expected to continue in the coming years [57]. Furthermore, BC treatment itself often has repercussions on the quality-of-life of patients, such as physical, psychological and social impairments, especially in women who have not yet reached menopause [58]. Some of the morbidities patients may suffer from

are weakness, stiffness, numbness, tingling, pain, poor range of motion/diminished mobility, skin fragility, swelling, lymphedema, brachial plexopathy, and neuropathic impairments, among others, depending on what their treatment regimen was [59]. These conditions usually appear within 12 months of surgery and may affect medical costs and days out of work.

There are different manifestations of BC, as there are various methods for the classification of its subtype. The four main intrinsic subtypes were determined by Perou *et al*. and Sørlie *et al*. over 20 years ago, based on the expression of genes that may be responsible for the phenotype of the tumour [60, 61]. During the two decades that have since passed, new work was able to confirm that the intrinsic subtypes grasp most of the biological diversity in BC [62]. The four subtypes are luminal A, luminal B, human epidermal growth factor receptor 2 (HER2)-enriched and basal-like BC [63].

The characterization of the intrinsic subtypes of BC is very relevant, as they are associated with different prognoses, overall survival and disease-free survival of the patients [61]. Despite luminal tumours being typically the most common, representing almost 70% of breast cancer manifestations [63], they usually have a better prognosis [64, 65]. Luminal B tumours are more likely to relapse, thus resulting in more severe disease courses [61]. Luminal A tumours, however, were found to have longer disease-free survival times, taking longer to form metastases [66]. On the other hand, HER2-enriched tumours account for 10-15% of the new diagnoses, and, due to the emergence of HER2-specific therapies, their prognoses have been greatly improved [63]. Finally, basal-like tumours comprise about 20% of breast cancer tumours, tend to be more aggressive and have worse prognosis.

Nonetheless, the effect on survival and prognosis is largely dependent on the application of adjuvant therapies. Engstrom *et al*. analysed the breast cancer-specific survival (BCSS) of women born between 1886 and 1928 in a county of Norway, when adjuvant therapy after surgery was rare, thus allowing for a near natural course of the disease [67]. From 909 patients they determined that, without treatment options other than surgery, the 5-year survival was lowest for HER2-enriched BC, around 50%. However, after those 5 years, no differences were found between BCSS of different intrinsic subtypes. Thus, if not for the employment of adequate adjuvant therapies, the expected survival of BC patients after 5 years would be similar, regardless of the initial tumour's intrinsic subtype.

The intrinsic subtype will also influence the therapeutic strategy [68]. Other than surgical intervention, there are 4 adjuvant (or neoadjuvant if administered before surgery) options in BC: radiotherapy, with localized effects; and hormone-, immune- and chemo-therapy, which have systemic impacts [69]. In short, surgery is the removal of the tumour (breast-conserving surgery) or the complete breast (mastectomy). The latter may also be used for prevention of BC. Radiotherapy, the irradiation of the tumour site with ionizing radiation, is strongly recommended for all BC subtypes after breast-conserving surgery. Chemotherapy consists in the administration of drugs that stop and/or kill cancer cells, and is recommended for all BC subtypes, except for most luminal A tumours. In hormone therapy, the biological processes stimulated by oestrogen are reduced, either by interfering with the hormone or its receptor, therefore being recommended in luminal tumours (which have hormone receptor overexpression) [70]. Immunotherapy consists in the administration of clonal antibodies, which will interfere with either the biochemical mechanisms responsible for cancer, or the immunosuppression in the tumour. The HER2-enriched subtype, though resistant to some forms of hormone and chemotherapy, has considerably improved survival when the latter is administered alongside HER2-targeted therapies, such as the antibody trastuzumab [71]. However, the clinical pathways may be

adjusted according to new research – e.g., there is compelling evidence that, in the future, if a patient has an excellent response to neoadjuvant therapy, surgery may be performed only if a local recurrence is found [72].

It is also relevant to elaborate on some of the nanotechnology-based treatments available for BC [73]. Some of these are specific for BC, while others are provided for numerous other cancer types. Nonetheless, the following examples all showcase the multiple benefits of nanoformulations, with an increase in blood circulation time and tumour uptake being prevalent in all cases. For instance, both Myocet™ and Caelyx™ are comprised of liposomal doxorubicin, only the latter is PEGylated. Indicated for metastatic BC, the encapsulation of the chemotherapeutic agent leads to a drop in cardiotoxicity. The more recent Pazenir™ is comprised of paclitaxel in albumin-bound NPs, which increase solubility, altogether with a decrease in severe toxicity. This protein-drug conjugate is approved for treatment of metastatic breast cancer and adenocarcinoma of the pancreas, and non-small cell lung cancer. Specifically for HER2-enriched BC, Kadcyla™ is an antibody-drug conjugate, consisting of the antibody trastuzumab (which targets HER2) and the cytotoxic DM1 (that acts by blocking cellular division) [73, 74]. Its nanoformulation yields higher selectivity and less toxicity. Similar effects are found when binding paclitaxel with albumin in the shape of spherical NPs, also known as Abraxane™, a product indicated for breast cancer, among other tumours [75].

## 2.2.1 Spheroids for Breast Cancer Research

Cell-based models are convenient tools not only to unravel basic molecular and cellular mechanisms of BC, but also for early screening of therapeutics. There are multiple cell lines available for each intrinsic subtype of BC [76]. For example: MCF-7 and BT-483 for luminal A; BT-474 and MDA-MB-361 for luminal B; SK-BR-3 and AU565 for HER2-enriched; MDA-MB-231 and BT-549 for basal-like. Due to the major effect the intrinsic subtype has on prognosis and treatment strategy, it is crucial to choose the most adequate cell line in accordance with the objective of the research [77]. Although there is an acceptable representation of the numerous molecular subgroups of BC, the fact is that some rarer subtypes remain without appropriate cell models.

After defining the most appropriate cell line, the cell models should be considered. While 2D cell cultures and animal models were initially the only available cancer models, 3D models (such as spheroids and organoids) started being developed at the end of the 20$^{th}$ century [78]. Whereas 2D cell cultures are simple to treat and analyse, they lack the structural, morphological and biochemical complexity of the tumour, thus being less biorelevant [79]. Though such detail is available in 3D models, these systems are more expensive, due to their complexity in maintenance and assessment.

Nevertheless, multicellular tumour spheroids (MCTS): (1) are capable of mimicking the lack of oxygen and nutrients inside the tumour (and, therefore, the altered metabolism, acidic pH and cell cycle arrest); (2) may be comprised of multiple cell types, including cancer stem cells; (3) simulate a 3D structure, which enables the deposition of extracellular matrix (ECM) and multiple cell-cell and cell-ECM interactions, creating physical barriers; (4) have gene expression levels and growth kinetics on par with those found in solid tumours [80, 81]. These properties provide spheroids with an internal structure comprised of distinct cell layers – an outer layer with proliferative cells, followed by an inner layer with quiescent cells, and the MCTS centre with necrotic cells (the necrotic core) [81]. Moreover, studies have shown that the

tumour microenvironment (TME) is crucial in determining the effects of a therapeutic approach, influencing how it interacts with the neoplastic cells. Indeed, previous works have determined that fibronectin, one of the components of the ECM, can protect cells from tamoxifen-induced cell death [82]. Thus, the TME can modulate tamoxifen resistance. Consequently, cell models capable of mimicking these characteristics are paramount to achieve tumour-like properties and, consequently, a closer appraisal of the effectiveness of various novel therapeutic approaches [83].

Spheroids have already been used to assess the feasibility of numerous potential therapeutic approaches, including those based on nanotechnology. For example, Bangde *et al*. prepared palladium NPs coated with trimethyl chitosan, attempting to achieve photothermal therapy while being biocompatible and muco/cell-adhesive [84]. These NPs were evaluated using 2D cell cultures and spheroids from MDA-MB-231 cells. Both models attested to the biocompatibility of the NPs when in the absence of a laser required for activation of the photothermal effect. Conversely, the same models were able to denote the ability to kill the tumour cells when laser irradiation occurred. This was found to be concentration dependent and more effective when spheroids were incubated with the NPs for 24 hours before laser treatment. Another work by Murphy and co-workers consisted of manganese dioxide NPs encapsulated in PLGA [85]. Their purpose was to reverse the lack of oxygen found inside the tumour, which limits the immune system's response – here evaluated as natural killer cell activation. The cellular uptake of the NPs was assessed using MCF-7 cells in monolayers and MCTS, but only the latter was tested for hypoxia reduction and cancer cell destruction. MCF-7 viability was similar in 2D and 3D cultures, and the NPs were not considered cytotoxic for natural killer cells either. The NPs were also able to penetrate spheroids and reduce hypoxia, which lead to metabolic alterations and increased penetration and death of the MCTS by immune cells. Finally, a new DDS was presented by Nieto and colleagues, where polydopamine NPs were loaded with paclitaxel and coated with trastuzumab [86]. It was foreseen that the intrinsic antineoplastic properties of polydopamine NPs would increase tumour cell death, acting synergistically with the loaded drugs. Indeed, both the DDS and comparable concentrations of free paclitaxel induced similar cell death in monolayers and spheroids of cell lines with overexpression of HER2. On the other hand, the DDS was much less harmful to stromal cells, thus reducing the adverse effects of free paclitaxel. Overall, the use of spheroids enriched these works, providing further information about the biorelevance of the formulated NPs, which could not be obtained simply through 2D cell models.

## 2.3 Histology Sample Preparation

Histology is the "branch of anatomy that deals with the minute structure of animal and plant tissues as discernible with the microscope" [87]. The analysis of histological images has been the base for much of our understanding of biological processes, with recent efforts vying to apply it on a molecular level, in order to uncover biochemistry mechanisms and the impact of toxins and therapeutics on organ function [88]. It has enormous consequences in medical diagnosis, identifying and characterizing pathologies from tumours to inflammatory diseases,

which could heavily influence the treatment strategy [89-91]. Additionally, histology may also be used for forensic investigations and autopsies, as well as in the education of students [92].

To visualize tissue, histological analyses overall follow a similar protocol: (1) fixation of the sample to maintain structure; (2) embedding and sectioning; (3) staining and observation [93]. Fixation is arguably one of the most important processes in histological sample preparation, as it preserves cells and their structure by stopping tissue decay [94]. This could be accomplished by physical fixation (such as heat and freeze-drying) or by chemical fixatives (cross-linking, coagulant, or compound). The most commonly used fixative, formalin, is a cross-linking fixative. The use of stains allows for greater contrast between important characteristics of the tissue, such as the nucleus or other parts of the cell (haematoxylin and eosin, the most commonly used stain) [95]. When sectioning tissues, there are mainly four distinct possibilities regarding the equipment to be used: microtome, ultramicrotome, vibratome and cryostat. Each of these instruments requires specific protocols and carries different advantages and drawbacks.

First and foremost, the microtome is used in formalin-fixed, paraffin-embedded (FFPE) specimens [96]. This technique starts with an initial fixation of the sample, followed by washing, dehydration, clearance (e.g., with xylol), and infiltration with the embedding medium paraffin. Once it has hardened, the paraffin block may now be cut using the microtome, and the resulting sections are adhered to microscope slides and stained. While this is the most common method of tissue processing, due to the consistent, inexpensive results, it has several limitations, such as the long processing time, damages to DNA caused by formalin, and obstructed access to antigens, which could affect immunohistochemistry assays [97, 98]. Nonetheless, protocols have already been developed for antigen retrieval methods [98].

The ultramicrotome is applicable for samples which were embedded in resin, a process which consists of the substitution of water (the major component of biological tissues) with a resin [99]. Once more, this sectioning procedure is only possible following the fixation of the tissue, whether it is chemical (e.g., glutaraldehyde) or physical (i.e., vitrification), as it allows for the maintenance of cellular morphology throughout the solvent exchange. Consequently, resin embedding remains a staple for ultrastructural investigation in electron microscopy, as it allows for thinner sections than FFPE with greater morphological detail. However, the stains available to the sections may be more restricted depending on the resin used, and it may be more difficult to detect antigens or isolate DNA [100, 101].

The vibratome trims specimens submerged in water, buffer or culture media using an oscillating blade, resulting in free-floating sections [102]. This technique can be used for fresh or fixed tissues, although unfixed samples will be significantly thicker than those that went through the fixation process [103]. A great variety of elements may be adjusted (e.g., vibration amplitude, blade speed and angle), which allows for the optimization of the sectioning. While generating high-quality, reliable sections can be made, these may be too thick, the process is considerably long and, depending on the tissue, may be quite complicated.

The cryostat is used for cryosectioning, a technique which will be addressed in greater detail in the following subsection.

## 2.3.1 Cryosectioning

Cryosectioning, or the frozen section procedure, was a technique developed in the late 19$^{th}$, early 20$^{th}$ centuries. During this time, longer anaesthetics and aseptic conditions allowed

for more complex surgical interventions, while other technological advances empowered multiple researchers to contribute to the conception of cryosectioning, a technique capable of rapid intraoperative diagnosis [104]. This would reduce the number of surgical interventions a patient was submitted to, therefore decreasing the risk of complications and/or side-effects [105]. Multiple researchers contributed to the conception and acceptance of this protocol, but some of the most well-known are: Dr. William H. Welch, Dr. Thomas S. Cullen, and Dr. Louis B. Wilson [106]. The latter, known as the father of the frozen section procedure, determined a protocol that became the most widespread in the US - not only due to the quick methodology and uniformly good results, but also an effective marketing strategy [107] and not citing contributors [104, 106].

Over time and scientific progress, further modifications were made to the cryosectioning protocol, and multiple variations were established for different purposes. Overall, this technique has a quite general protocol which requires few components: the tissue sample, an embedding medium, a cryostat, positively-charged microscope slides, and, if so desired, fixatives and stains (Figure 3) [108, 109].

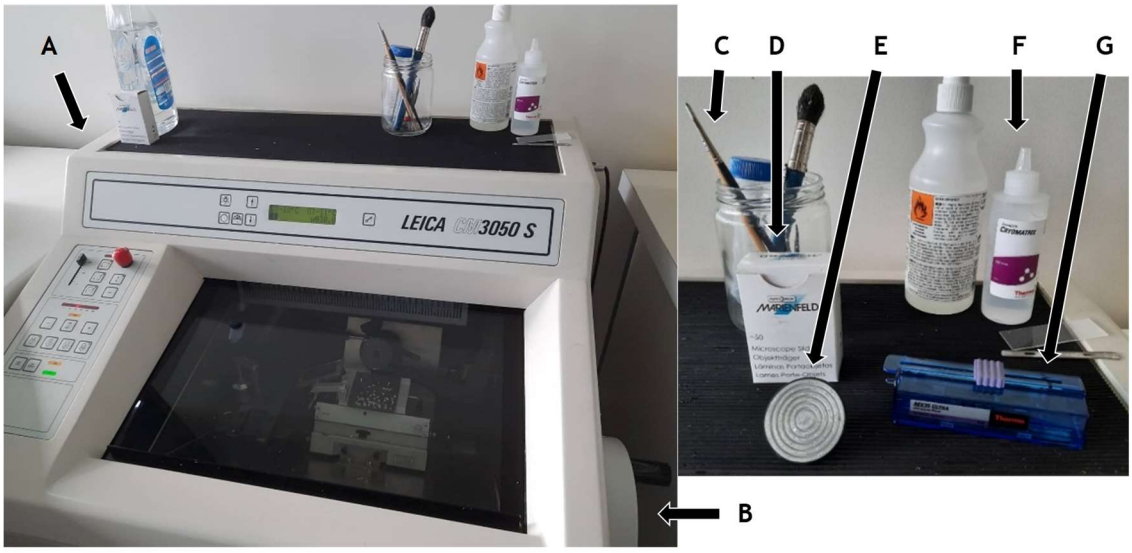


**Figure 3 -** Image of a (A) cryostat with its (B) handwheel, (C) brushes, (D) microscope slides, (E) chucks, (F) embedding media, and (G) stainless steel knife.

Briefly, the protocol is as follows [109]: the sample, after identification of the required macroscopic structures for correct tissue orientation, is placed on a metal chuck and submerged in the embedding compound. Its purpose is to maintain the structural integrity of the specimen after it is frozen, without penetrating the sample itself, thus providing a smooth cutting surface [110]. The embedding compound could be gelatine, agar or, more commonly, OCT (Optimal Cutting Temperature compound). OCT, a cryopreservative, is a mixture of glycols and resins, such as polyvinyl alcohol (PVA) and PEG, that is widely used due to being effective in preserving the morphologic and immunohistological characteristics of tissues for posterior evaluation [111]. After enclosing in the embedding compound, the chuck with the tissue is transferred to the cryostat. The cryostat is a microtome inside a cooling chamber, which allows for the maintenance of low temperatures necessary for rapid tissue freezing, thereby preventing the formation of ice crystals [112]. Subsequently, the chuck is mounted on the cryotome or

stage (the movement of which is controlled by a handwheel on the outside of the cryostat), in a parallel position to the stainless-steel blade. Following the trimming of the excess embedding compound, the thickness of the cut is chosen, and sectioning may begin. Each cryosection must be carefully guided from the knife edge (oftentimes, with the assistance of antiroll glass and brushes), to prevent roll-up [108]. The section is then quickly adhered to a room-temperature, positively-charged microscope slide – this property strengthens the attachment of the sample, due to the negative charge of the cells. The slides may be washed with PBS to remove the embedding compound, before the sample is fixed and/or stained, if so desired [113]. Finally, a coverslip is placed on the slide, and microscope observation may begin.

As previously stated, one of the main applications of the frozen section procedure is the intraoperative diagnosis. Indeed, cryosections enable the identification of the tissue type, if it is malignant, which type of tumour, where the surgical margins are, possible positive lymph node and the existence of metastases in other tissues, among other features [114, 115]. Despite the lower quality of the tissue sections against paraffin-embedded samples, the ability to guide the surgeon's course of action is a positive trade-off [115]. Furthermore, unlike cryosectioning, the standard processing associated with FFPE (e.g., fixation) may be prejudicial to subsequent experiments, which is the case of some enzymatic, lipid/carbohydrate histochemistry and immunohistochemistry assays [109, 116]. The staining of some tissues is likewise facilitated when conducted in frozen sections [116]. Nevertheless, the loss of morphological details compared to FFPE sections, along with the development of antigen retrieval and the creation of antibodies capable of reacting in FFPE samples, has decreased the usefulness of cryosectioning [117, 118].

Nowadays, biological samples analysed following a FFPE protocol can provide quick results, sometimes even on the same day. In spite of this, multiple works have shown that, while FFPE is usually the reference standard that yields the final diagnosis, the frozen section procedure has an overall reliability of over 90% in tumour detection and/or assessment, depending on tissue types and organ system [119-121]. Nonetheless, the accuracy and sensitivity of cryosectioning may be reduced in the detection of BC sentinel lymph node micro metastases [122], as well as in the diagnosis of borderline tumours, resulting in underdiagnosis [123, 124]. Overall, cryosectioning remains a staple in histochemistry, immunohistochemistry and intraoperative diagnosis [125].

As already outlined, cryosectioning has numerous applications. Various studies have established washing protocols in order to remove the signal from OCT (caused by ion suppression due to PEG) without affecting the outcome of various mass spectrometry assays in frozen sections, such as liquid chromatography coupled to tandem mass spectrometry (LC-MS) or matrix assisted laser desorption/ionization mass spectrometry imaging (MALDI-MSI) [126, 127]. Prior work has instead opted to snap freeze tissues, such as mouse liver, without an embedding compound, using OCT simply to adhere the sample to the cryostat stage, and preventing it from contaminating the frozen section [110]. Cryosections of 3D cellular models, i.e., embryoid bodies and organoids, have also been evaluated through immunohistochemistry and immunofluorescence studies [128, 129]. For spheroid cryosection followed by MALDI-MSI, the necessity of an embedding compound found OCT replaced by gelatine or foregone by utilizing ice-coated MCTS [130]. The viability of triple-culture spheroids modelling melanomas in early stages was confirmed by cryosectioning these 3D models, followed by immunofluorescence [131]. Finally, in Priwitaningrum *et al.*, spheroid frozen sections were made for immunohistochemistry assays and measurement of NP penetration [132].

# Chapter 3. Materials and Methods

## 3.1 Materials and Reagents

Michigan Cancer Foundation-7 (MCF-7) cells were kindly provided by Dr. Meriem Lamghari (i3S, Porto, Portugal). Penicillin-streptomycin solution was bought from Corning (Corning, NY, USA). Heat-inactivated FBS was purchased from PAN-Biotech GmbH (Aidenbach, Germany). Dulbecco's Modified Eagle Medium/Nutrient Mixture F-12 (DMEM/F-12) was purchased from ThermoFisher Scientific (Waltham, MA, USA). SeaKem® LE agarose was purchased from Lonza (Rockland, ME, USA). Micro-moulds 3D Petri Dish® (12-81-Large Spheroids) were from MicroTissues Inc. (Sharon, MA, USA). Fisherbrand disposable base moulds, 1.5 × 1.6 cm gene frames (65 µL), isopropanol (IPOH), sodium chloride and potassium dihydrogen phosphate were from Fischer Scientific (Hampton, NH, USA). D-(+)-trehalose dihydrate (TRE), dimethyl sulfoxide (DMSO), trypsin, and disodium hydrogen phosphate were purchased from Sigma-Aldrich (St. Louis, MO, USA). CellTiter-Glo® was from Promega (Madison, WI, USA). OCT and potassium chloride were purchased from VWR International (Radnor, PA, USA). Red fluorescent carboxylate-modified polystyrene (COOH-PS; FluoSpheres™) NPs with 100 nm nominal diameter were purchased from Molecular Probes (Eugene, OR, USA). Amicon Ultra-0.5 mL (100 kDa MWCO) centrifugal filters were from Merck Millipore (Burlington, MA, USA). Normafrost slides, silane pre-coated were from Normax (Marinha Grande, Portugal), Deckgläser microscope cover glasses were purchased from Waldemar Knittel Glasbearbeitungs GmbH (Braunschweig, Niedersachsen, Germany) and microtome blade C-35 from PFM Medical (Cologne, Germany). Poloxamer 407 (P407) – a poly(ethylene glycol)-poly(propylene glycol)-poly(ethylene glycol) (PEG-PPG-PEG; average MW of 9.8 to 14.6 kDa) - was a kind offer from BASF (Ludwigshafen, Germany). PS NPs were PEGylated in-house (5 kDa PEG was covalently bound to the surface of NPs by carbodiimide chemistry, courtesy of Helena Almeida) according to a previously described protocol [133]. All reagents and materials were of analytical grade or equivalent.

# 3.2 Methods

## 3.2.1 Cell Culture and Spheroid Production

MCF-7 cells were cultured in DMEM/F-12 media, supplemented with 10% FBS, penicillin (100 IU/mL) and streptomycin (100 mg/mL), further referenced as complete media. Cells were incubated under standard conditions (5% $CO_2$, 95% relative humidity, 37 °C), with media changed every other day. Cells were typically sub-cultured after reaching 80-90% confluence by dissociation with trypsin, centrifugation (1,200 rpm, 5 min), resuspension in complete medium and placement in new vessels at a sub-cultivation ratio of 1:3 to 1:6.

The protocol for spheroid development was adapted from Bauleth-Ramos, *et al.* [134]. For mould production, 0.9% NaCl (*w*/*v*) in ultrapure water and agarose were sterilized and mixed to a final polymer concentration of 2% (*w*/*v*). The solution was heated and 550 µL was cast onto each micro-mould to form agarose moulds with 81 homogenous recesses (Figure 4). After cooling and solidifying, the agarose moulds were transferred to a 12-well plate and incubated with approximately 2 mL of complete media to equilibrate the moulds for at least 2 h before cell seeding. Afterwards, a cell suspension of around 2.13 x $10^6$ cells/mL (around 5 000 MCF-7 cells per MCTS) was added to the moulds (190 µL per mould) and allowed to settle for 30 min. Finally, 2 mL of complete media was gently added to the wells, and the plates were placed in the incubator, with the media changed every 2 days.

MCTS were grown for at least 5 days before analysis, with cell culture media changed every other day. Spheroids typically present a necrotic core after this amount of time in culture [135].

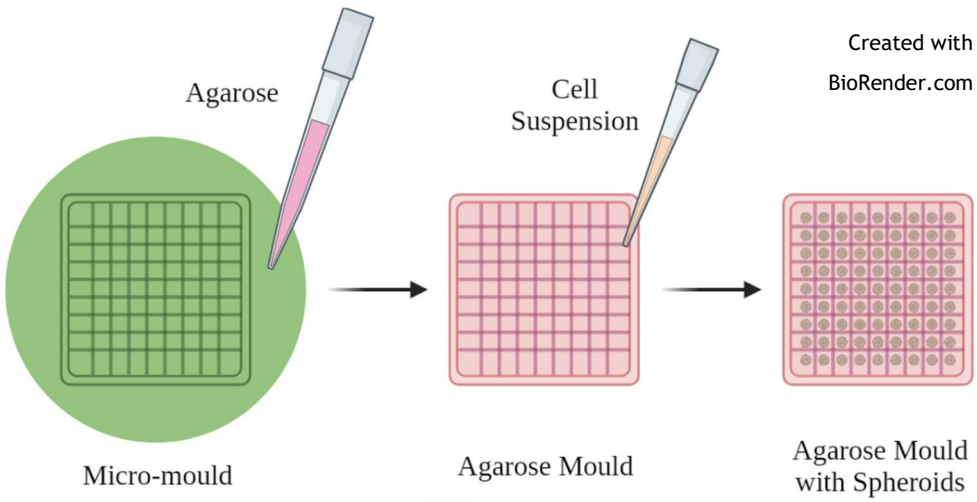


**Figure 4** – Schematic representation of the formation of the micro-mould and subsequent cell seeding.

## 3.2.2 Spheroid Viability After Freezing

Spheroid viability after freezing was assessed using the CellTiter-Glo® viability assay. Different freezing conditions were tested to maximize cell viability, as detailed in Table 2. In

short, DMSO and TRE were both diluted in complete media at various concentrations, and incubated with the spheroids for 10 min, before removal and inclusion of the moulds in OCT. In gradual cooling samples, MCTS were included in OCT, placed in an IPOH bath, and transported to the cryostat. Samples submersed in liquid nitrogen were previously placed in disposable base moulds and covered in OCT before being transferred to the cryostat after freezing. Different incubation time and temperature for removing the spheroids from the cryostat were tested to enable the best conditions for cells to recuperate after a freezing/defrosting cycle. Finally, the toxicity of OCT was determined after 15 min and 2 h of contact with spheroids.

**Table 2 -** Overview of the various freezing conditions.

| **Parameter Tested** | **Conditions** |
|---|---|
| Incubation Temperature (Thawing) | Room temperature (RT) |
| | 37 ºC |
| OCT Toxicity | 15 min |
| | 2 h |
| DMSO | 5% in complete medium |
| | 10% in complete medium |
| | 15% in complete medium |
| | 10% in OCT |
| Gradual Cooling (IPOH Bath) | IPOH |
| | IPOH + 10% DMSO |
| Extracellular Osmotic Regulators (TRE) | 5% |
| | 10% |
| | 15% |
| | 5% + 5% DMSO |
| Freezing in Liquid Nitrogen | 10 s |
| | 10 min |
| Incubation Time (Thawing) | 30 min |
| | 6 h |

Overall, cell medium was removed from the moulds and they were included in OCT before freezing. They were maintained inside the cryostat at around -20 ºC for 2 h before OCT was removed and the moulds were transferred to a 12-well plate. After incubation in complete

media for thawing, spheroids were removed from the moulds and placed in a 96-well plate, 2 spheroids per well in 100 µL of medium (*Annex, Figure A1*). CellTiter-Glo® (100 µL) was added to each well, plates were shaken (150 rpm) for 5 min, and incubated at RT for 25 min. As a control condition, spheroids remained in the incubator until CellTiter-Glo® application. The luminescence of the samples was measured using a SynergyMx™ MultiMode Micro-plate Reader from BioTek (Winooski, VT, USA). The viability of the MCTS was calculated as:

$$Viability\ (\%) = 100\ x\ (RLU_S - RLU_B)/(RLU_C - RLU_B) \quad (5)$$

where $RLU_S$, $RLU_B$ and $RLU_C$ are the relative light units of the samples, blank and control, respectively.

## 3.2.3 Processing of Nanoparticles

FluoSpheres™ were washed thrice with ultrapure water using centrifugal Amicon filters to remove the stabilizing agent sodium azide (4,000 rpm, 10 min). NPs were then resuspended in ultrapure water and stored in the dark, at 4 ºC until further use. For coating, NPs were incubated for a minimum of 12 h in a 1% (*w*/*v*) solution of P407 or in ultrapure water, further referred to as P407 and bare NPs, respectively. Finally, before usage, they were washed thrice as detailed above.

To assess the permanence of the adsorbed poloxamer coating, washed bare and P407 NPs were placed in a 10 mM solution of sodium chloride, at a final concentration of 0.01% (*w*/*v*). NPs were stored at 4 ºC in the dark, and samples were tested every day for 5 days using a ZetaSizer Nano ZS (Malvern Instruments, Malvern, UK). The size (hydrodynamic diameter) and polydispersity index (PdI) were determined through DLS, and surface charge (zeta potential) by Electrophoretic Light Scattering (ELS). Measurements were carried out at 25 ºC, with 3 runs per sample.

## 3.2.4 Cryosectioning Protocol

The moulds with spheroids were included in OCT after cell media was removed from the moulds. They were then transferred into the cryostat, frozen and sectioned into 50 µm thick slices (Figure 5). Then, the cryosections from the central plane of the MCTS were transferred to normafrost microscope slides and washed in PBS (137 mM NaCl, 2.7 mM KCl, 10 mM $Na_2HPO_4$ and 1.8 mM $KH_2PO_4$; pH 7.4) until agarose and OCT residues were removed as visible to the naked eye. Cell culture medium (60 µL) was added at RT to the samples before they were covered with a coverslip and incubated at RT for at least 30 min before microscopic observation.

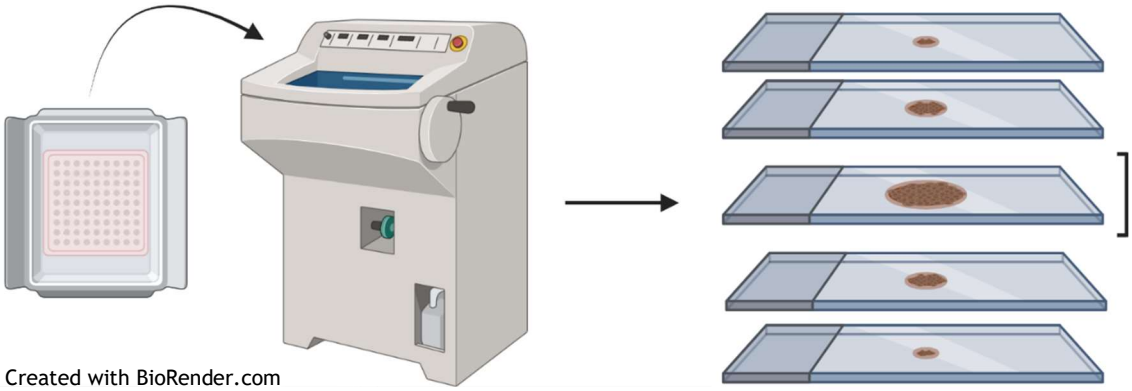


**Figure 5 -** Schematic representation of the cryosectioning protocol. The OCT-embedded mould is frozen inside the cryostat, cut and adhered to positively-charged microscope slides. Sections roughly around the centre of the spheroid were chosen for microscope visualization.

## 3.2.5 Nanoparticle Incubation and Multiple Particle Tracking Analysis

Spheroids were incubated with bare and P407 NPs either since initial cell seeding (SS) at a concentration of 0.0001% in complete cell medium or just 6 h before observation (BO) at the microscope at a concentration of 0.001%. FluoSpheres™ were also included at the aforementioned concentration when culture medium was replaced during MCTS development under the SS condition.

The transport of fluorescent NPs was assessed by analysing their trajectories in whole and cryosectioned spheroids. For whole MCTS, medium was replaced with complete medium without NP, before the spheroids were removed from the agarose mould and transferred to the microscope slide, which was then sealed with a coverslip. Cryosectioning of MCTS was performed as described above. The environment in the slides was airtight thanks to the gene frames, which also prevented the compression of the biological matrices (Figure 6). Samples featuring visible movement of spheroids or cryosections were discarded.

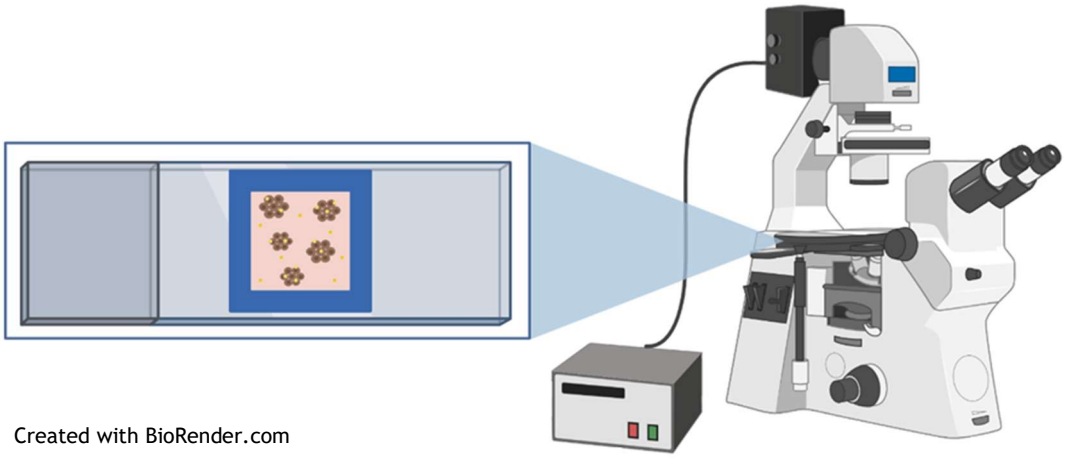


**Figure 6** - Schematic representation of video acquisition of NPs in whole and cryosectioned spheroids. Samples were in an airtight environment provided by the gene frames and were observed using an inverted epifluorescence microscope with a 63x immersion objective, under the TX2 filter.

Videos were recorded using a Hamamatsu ORCA-Flash4.0 digital CMOS camera (Hamamatsu, Japan) mounted on a Leica DMI6000 inverted epifluorescence microscope (Wetzlar, Germany) equipped with a 63×/1.30 NA glycerine (GLYC)-immersion objective and a TX2 filter set. Videos (512 × 512 pixels, 16 bit) were collected with the LAS X software at a temporal resolution of 66 ms for approximately 20 s (303 frames), and with a pixel resolution of 0.159 µm. Acquired video files (.lif format) were analysed using ImageJ/Fiji (v. 2.5.0, available at https://imagej.net/software/fiji/; last accessed 23 Jul 2022), and two-dimensional Cartesian coordinates of particle centroids were detected at subpixel resolution using the MosaicSuite 2D/3D single-particle tracking plugin developed by Sbalzarini and Koumoutsakos [136]. Data were exported as CSV files and analysed with the MPTHub software (v. 1.0.3) developed in-house for conducting MPT analysis [1].

A minimum of 3 independent spheroids per experiment were chosen based on morphology for both whole and cryosectioned MCTS, with sections likewise selected considering their size (and therefore, closeness to the central plane). Trajectories with at least 50 consecutive frames were considered valid for transport analysis but were discarded if the value of $\alpha$ was lower than zero. Three independent experiments were conducted, each tentatively collecting the trajectories of at least one hundred NPs. Additionally, MPT analysis was conducted on trajectories divided according to the sections of the MCTS where these were observed (i.e., border, inner layer or necrotic core).

### 3.2.6 Statistical Analysis

Results are presented as mean values ± standard deviation (SD). Statistical analyses were performed using one-way ANOVA with Tukey's multiple comparisons test, with a single pooled variance. The level of significance was set at probabilities of * $p < .05$, ** $p < .01$, *** $p < .001$ and **** $p < .0001$. All statistical analyses were conducted using GraphPad Prism (v. 8.4.3) (GraphPad Software, San Diego, CA, USA).

# Chapter 4. Results and Discussion

## 4.1 Spheroid Viability

Anticancer drugs must be able to reach solid tumours to successfully achieve diagnostic and/or treatment goals [137]. Long-standing opinion claimed that NPs are able to extravasate into the tumour through the large gaps between endothelial cells in tumour blood vessels [138]. However, recent evidence highlighted that the transport of NPs into and in tumours is much more complex, involving multiple mechanisms including diffusion and even active processes [139].

To guarantee that the movement of NPs in the cryosection was similar to their transport in the tumour, viability assays were performed, which measured the quantity of ATP in the spheroids as a proxy for viability. These tests sought to determine if the freezing of the MCTS had a negative impact on the cells, which could affect their ability to represent the native structure and behaviour of the biological environment, and, ultimately, affect the transport of particles. Thus, ensuring that spheroids maintained cell viability after a freezing protocol compatible with the process of cryosectioning would be paramount to guarantee that the MPT results were not describing changes induced by MCTS processing. The generated spheroids presented three distinct layers and had an average of 415 μm diameter, as expected from previous unpublished works by this group.

### 4.1.1 Incubation Temperature

Initially, the spheroids were frozen as described previously, and thawed in cell culture media for 30 min, to allow the cells to recuperate from the low temperatures. We first studied if the incubation temperature during thawing would impact cell viability. The conditions tested were spheroids incubated at RT and 37 ºC, based on previous studies [2-4].

Results determined that the cell viability drastically dropped after freezing, regardless of the incubation temperature (Figure 7). Indeed, viability was reduced to less than 20% when compared to the control spheroids. Additionally, it appears that the incubation temperature did not impact viability beyond the effect of freezing. Thus, aiming to simplify the cryosectioning protocol, it was decided that the standard freezing conditions (Standard OCT) would be those that culminated with incubation at RT.

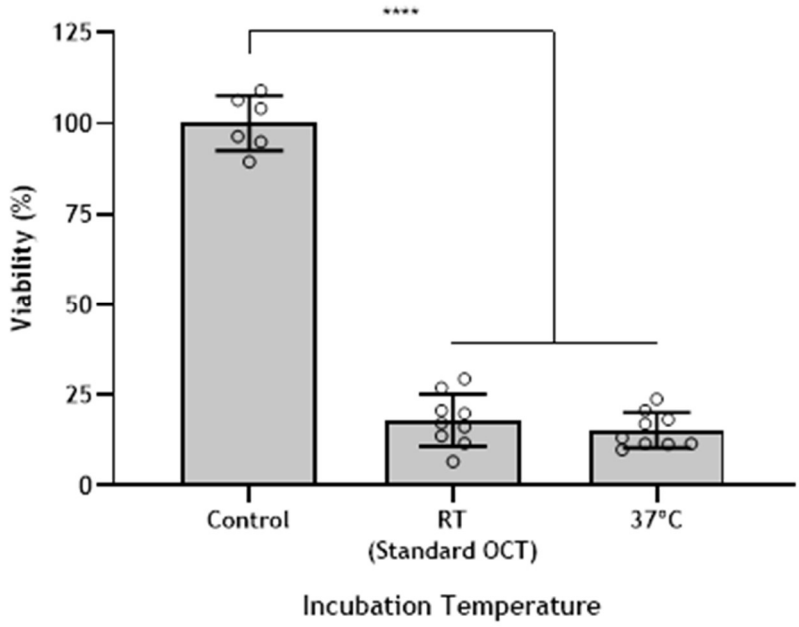


**Figure 7 -** Spheroid viability after freezing and recovering at different incubation temperatures. Viability declined to under 20% after freezing, and incubation temperature did not generate significant differences. Columns and bars represent mean ± SD, respectively, and symbols represent individual values ($6 \leq n \leq 9$). (****) denotes $p < 0.0001$.

Poor cell viability raised two hypotheses: (1) OCT was toxic to the cells, thus inducing their death; or (2) the process of freezing/defrosting the spheroids was killing cells. To appraise the former, the effect of OCT without subsequent freezing was evaluated on cell viability. To abbreviate the latter, we assessed the effect of cryoprotectants, gradual cooling, liquid nitrogen freezing and different incubation intervals on cell viability.

## 4.1.2 OCT

To guarantee that the lack of viable cells was not caused by the OCT compound, MCTS were incubated in it for 15 min or 2 h, without freezing, before cell viability was determined. As shown in Figure 8, OCT did not appear to affect spheroids, as cell viability remained constant, at both incubation times, and no statistically significant differences were found. Thus, the lack of viability previously determined seems to be caused by the freezing/defrosting process.

These are interesting results since cells were able to roughly maintain viability even without any source of nutrients during their incubation in OCT. While it could be argued that 15 min is too short a timeframe to cause significant cell death that could not be amended during the ensuing incubation in complete medium, the same seems to be more puzzling for 2 h. As previously noted, OCT is comprised of a mixture of glycols and resins, namely PVA and PEG [111], which are found at around 10% and 4%, respectively [140]. Prior research has found that both PEG and PVA coated NPs are biocompatible with a cell line from a human cervical carcinoma [141]. Indeed, a PVA-PEG hydrogel did not induce toxicity in human dermal fibroblasts or keratocytes [142]. Moreover, hydrogels are known to maintain cell viability and function when

encapsulating cells [143]. Thus, it is possible that OCT was able to function as a hydrogel and, by retaining humidity and oxygen diffusion, enabled the maintenance of spheroid viability.

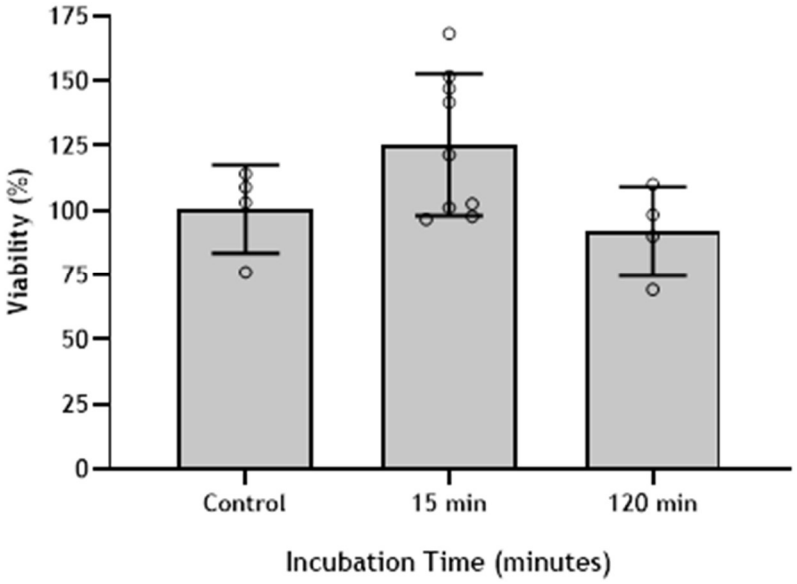


**Figure 8** – Spheroid viability after contact with the embedding compound OCT for 15 min or 2 h. Viability was not affected by OCT, and no significant differences were found. Columns and bars represent mean ± SD, respectively, and symbols represent individual values ($4 \leq n \leq 9$).

## 4.1.3 Dimethyl Sulfoxide

DMSO is a common cryoprotectant for animal cells, which penetrates the cellular membrane and stabilizes the intracellular osmotic pressure, preventing the formation of ice crystals when cells freeze [144]. Although generally used at a 10% concentration, previous work found that MCTS could require different concentrations of DMSO so as to guarantee its cryoprotective action [145, 146].

To determine the optimal concentration of DMSO, three dilutions of DMSO in complete media were tested – 5%, 10% and 15% (v/v). Viability results suggested that the most effective concentration was 10% DMSO in complete medium, which led to a value of 33% (Figure 9). Both a higher and lower concentration of DMSO caused an apparent decrease in the viability of the spheroids. However, no statistically significant differences were found between the various DMSO concentrations. These results were unexpected, as previous reports on MCTS viability using similar DMSO concentrations denoted values of around 80% [145, 146]. The significant discrepancy in cell preservation may be due to the different freezing temperatures (-20 ºC in the cryostat, in contrast to around -80 ºC followed by immersion in liquid nitrogen in previous works).

As the DMSO is not in contact with the MCTS while they are being frozen, another condition was evaluated, where DMSO was diluted in OCT (at a final concentration of 10%) instead of cell culture medium. This allowed for the continued presence of DMSO in the environment of the

spheroids during the freezing process. Nonetheless, there was no increase in cell viability. Indeed, values were similar to those found at 15% DMSO. Thus, it appears that the presence of DMSO in OCT does not increase spheroid viability as compared to its dilution in complete medium. Overall, a concentration of DMSO of 10% in medium provided the best cell protection, but still at unsuitable levels.

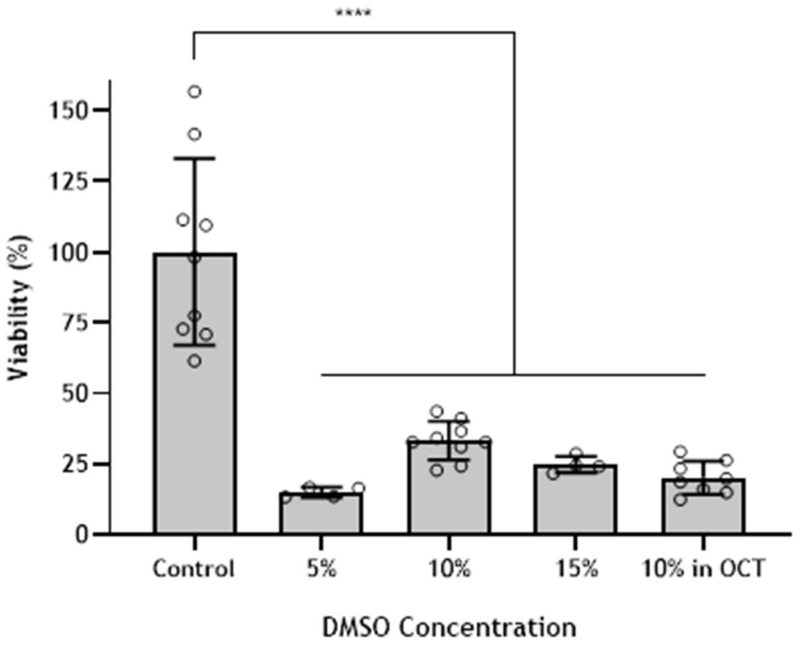


**Figure 9 -** Spheroid viability after freezing and including DMSO in medium. Spheroids were incubated for 10 min with DMSO 5%, 10% and 15% in complete medium, or frozen in a solution of 10% DMSO in OCT. Viability declined to under 35% of the control, with the highest values observed for samples incubated with 10% DMSO in complete medium. Variations in DMSO concentration did not generate significant differences. Columns and bars represent mean ± SD, respectively, and symbols represent individual values ($4 \leq n \leq 9$). (****) denotes $p < 0.0001$.

## 4.1.4 Extracellular Osmotic Regulators

Previous research has shown that extracellular osmotic regulators, such as the cryoprotectant TRE, could improve MCTS preservation, presumably by decreasing the freezing point of the spheroids [147]. Different TRE concentrations (5%, 10% and 15%) were assessed to ascertain if this sugar could indeed increase cell viability. Additionally, TRE and DMSO, extracellular and intracellular cryoprotectants respectively, were tested together to determine if any additive or synergistic effect occurred.

Results indicated that TRE could not improve cell viability beyond 16%, regardless of the presence of DMSO (Figure 10). These findings are in contradiction with past work reporting 30% to over 60% viability of spheroids after freezing in the presence of TRE [147]. Nonetheless, these MCTS were frozen in cryovials, and the temperature at which they were stored (-80 ºC for 4 h followed by transfer to the vaporous phase of liquid nitrogen at least overnight) was substantially different from the cooling at -20 ºC for 2 h tested in our experiments. Thus, it seems the presence of TRE does not increase spheroid viability, even with the addition of DMSO.

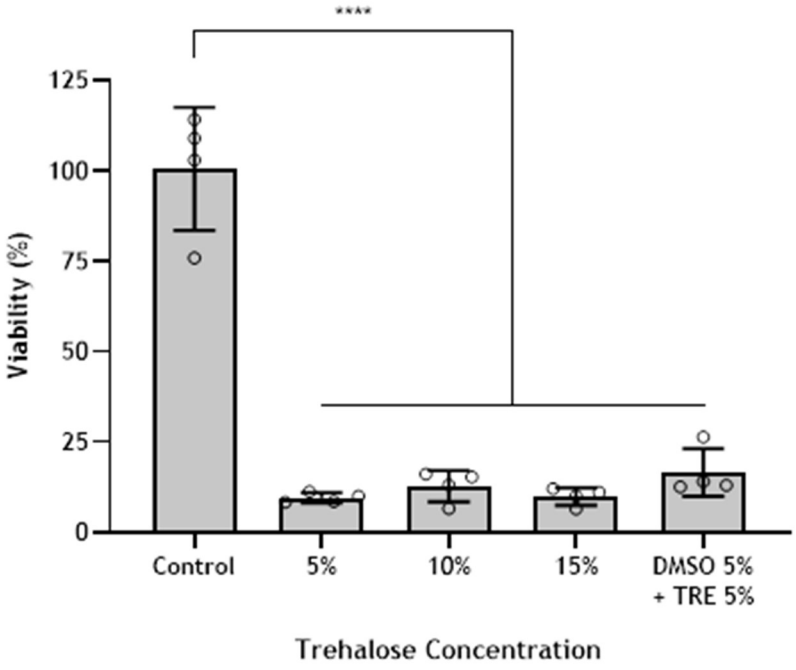


**Figure 10 -** Spheroid viability after freezing in the presence of various TRE concentrations and TRE with DMSO. Spheroids were incubated in complete medium with TRE 5%, 10% and 15%, and TRE 5% + DMSO 5% for 10 min. Viability dropped to less than 20%, and the only significant differences were between the control and the samples. Columns and bars represent mean ± SD, respectively, and symbols represent individual values ($n$ = 4). (****) denotes $p < 0.0001$.

## 4.1.5 Gradual Cooling during Freezing

IPOH allows for the cooling of the biological samples at an approximate rate of 1 °C per minute, which has been established as an effective cooling rate to preserve cells during freezing processes [148]. To determine if the gradual cooling could preserve cell viability, the samples were placed in an IPOH bath inside the cryostat. One of them was also previously incubated with 10% DMSO in cell culture media for 10 min, as cryoprotectants may circumvent cell damage during gradual cooling [149].

Unexpectedly, the gradual cooling did not help preserve MCTS viability (Figure 11). The IPOH bath reduced viability to less than 13%, and the addition of DMSO resulted in a value of around 18%. This last result contrasts with those found for MCTS incubated with the same concentration of DMSO under non-controlled cooling (roughly 33%). Overall, it seems that the IPOH bath was not useful in maintaining spheroid viability.

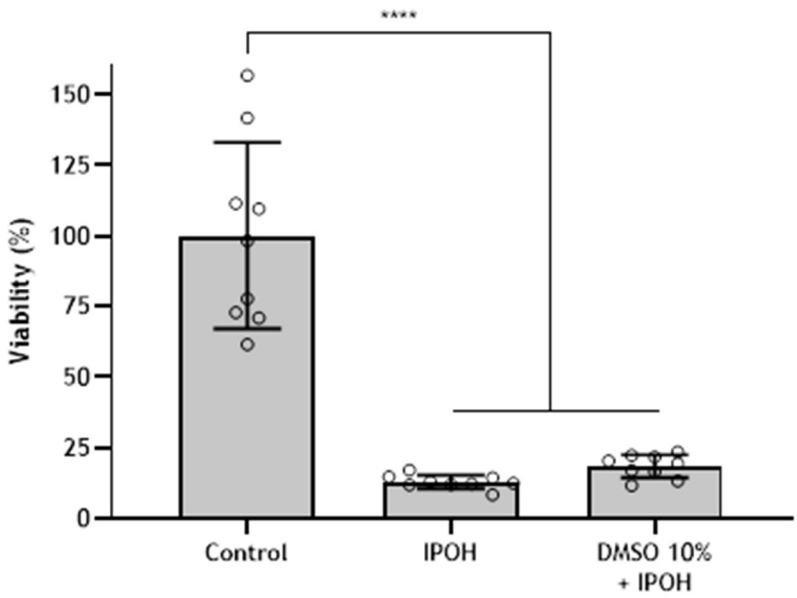


**Figure 11 -** Spheroid viability after temperature-controlled freezing in an IPOH bath. Spheroids were gradually cooled using an IPOH bath, with and without prior incubation with 10% DMSO in complete media for 10 min. Viability dropped to less than 20%, and the presence of DMSO did not cause significant differences. Columns and bars represent mean ± SD, respectively, and symbols represent individual values ($n$ = 9). (****) denotes $p < 0.0001$.

## 4.1.6 Ultra-Rapid Freezing in Liquid Nitrogen

There are two distinct practices to preserve cells in the frozen state: gradual cooling (e.g. in IPOH) and ultra-rapid (or snap) freezing [149]. The high rate of cooling in ultra-rapid freezing should prevent the formation of intracellular ice crystals, therefore minimizing damage to the cellular structure [148].

To assess if snap-freezing would allow for maintenance of cell viability, MCTS were submerged in liquid nitrogen for various time intervals before being transferred to the cryostat. Results demonstrate that viability dropped to less than 10%, regardless of immersion time (Figure 12). Moreover, there were no significant differences in viability between different incubation times. This could be due to the quick temperature transition between RT and -180 ºC undergone by spheroids, instead of the gradual cooling until -80 ºC before being placed in liquid nitrogen. Therefore, it seems that a swift cooling of the sample cannot increase cell viability.

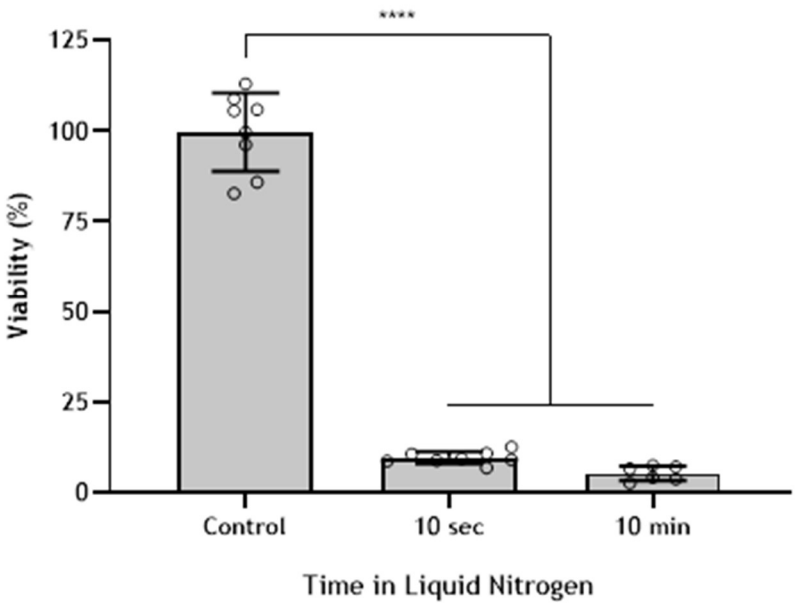


**Figure 12 -** Spheroid viability after snap-freezing at different immersion times in liquid nitrogen. Viability dropped to less than 10%, and no significant differences were found between different submersion intervals. Columns and bars represent mean ± SD, respectively, and symbols represent individual values ($6 \leq n \leq 8$). (****) denotes $p < 0.0001$.

## 4.1.7 Incubation Time After Defrosting

It was possible that the lack of viability calculated was not due to cell death, but instead because the spheroids were still quiescent after being frozen. To assess this possibility, different incubation times were tested, which should allow for cells to resume "normal" metabolic activity during this timeframe. MCTS were incubated at 37 ºC after thawing for 30 min or 6 h before performing the CellTiter-Glo® assay. Surprisingly, longer incubation was not only unable to increase spheroid viability, but indeed trended towards an even lower value (Figure 13). Thus, it appears that the low viability of the samples is in fact irreversible.

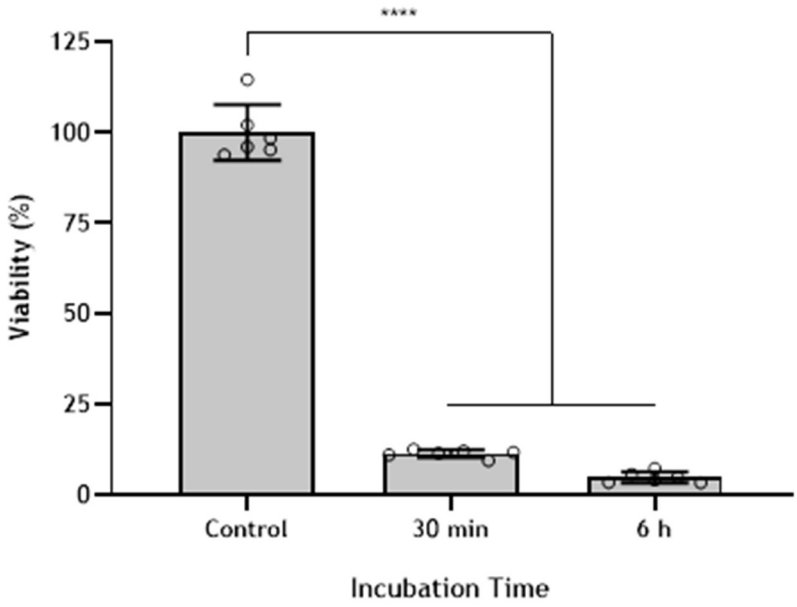


**Figure 13 -** Spheroid viability after different incubation times (30 min or 6 h) after thawing. MCTS were incubated at 37 ºC for the duration of the incubation. Viability dropped to less than 12%, and there were no significant differences between different incubation times. Columns and bars represent mean ± SD, respectively, and symbols represent individual values ($n$ = 6). (****) denotes $p < 0.0001$.

## 4.1.8 Overview on MCTS Viability Studies

Despite multiple efforts regarding OCT-mediated processing of MCTS, results showed that it was not possible to obtain usable sections without extensively affecting cell viability. At best, we were able to achieve a decrease of around 67% in viability when using 10% DMSO in complete medium before OCT incorporation and further freezing/defrosting. Although other freezing protocols could be assessed, the previous results appear to clearly demonstrate that cryoprotectants, gradual cooling/rapid freezing, and different incubation times and temperatures for thawing were unable to maintain cell viability. Though it could be argued that following strictly the usual protocol for cell cryopreservation (incubation in DMSO, gradual cooling until the sample reaches around -80 ºC, then transfer to liquid nitrogen) could perhaps improve cell viability, the different experiments shown have already discarded the possibility. Indeed, the initial steps of the cryopreservation protocol were modified to be compatible with the frozen sectioning procedure (i.e., removing liquids, as they would form ice crystals that would damage the integrity of the cryosection), and this sample (IPOH + DMSO 10%) had a viability of around 18%, which was similar to the standard OCT condition.

Overall, the most interesting condition to use for cryosectioning would be standard OCT (due to its simplicity). Despite the cryoprotectant having resulted in a mean higher value of viability, no significant differences were found when comparing tested conditions (Figure 14). Thus, the standard OCT procedure was chosen for cryosectioning MCTS samples intended for MPT analysis.

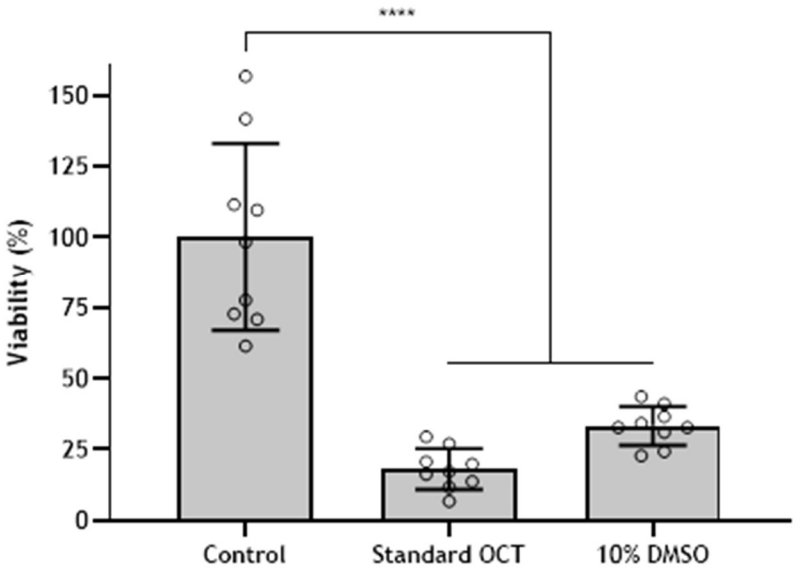


**Figure 14** – Summary of spheroid viability in samples included in OCT with and without prior incubation in 10% DMSO in complete medium for 10 min (please note that these data have been presented previously in Figure 9 and Figure 7, respectively). Columns and bars represent mean ± SD, respectively, and symbols represent individual values ($n$ = 9). (****) denotes $p < 0.0001$.

# 4.2 Characterization of Nanoparticles

The physicochemical attributes of NPs upon processing and after 5-day storage were analysed using DLS and ELS. Results are presented in Figure 15 and denote that properties were not affected for up to 5 days in storage. Mean hydrodynamic diameter values of bare NPs (around 106 nm) were close to nominal values for FluoSpheres™, while modification with P407 slightly increase the diameter to around 123 nm. This size range is considered adequate when NP-mediated drug delivery to tumours is intended [150]. Both bare and P407-coated NPs had low mean PdI values which did not surpass 0.1, therefore indicating a homogenous size distribution and considered acceptable in practice [151]. Successful dense coating of carboxylated NPs with P407 (a PEG-based co-polymer) was confirmed by the shift of markedly negative zeta potential values (around -51 mV) to near neutral ones (approximately -3 mV). Unlike a previous study [152], it was determined that the poloxamer coating persisted throughout the experiment. Maintenance of these values, as well as those for diameter, appear to support that P407 coating remains up to at least 5 days after modification. These results led us to speculate that P407 coating of NPs could potentially persist even when incubated during spheroid formation and growth.

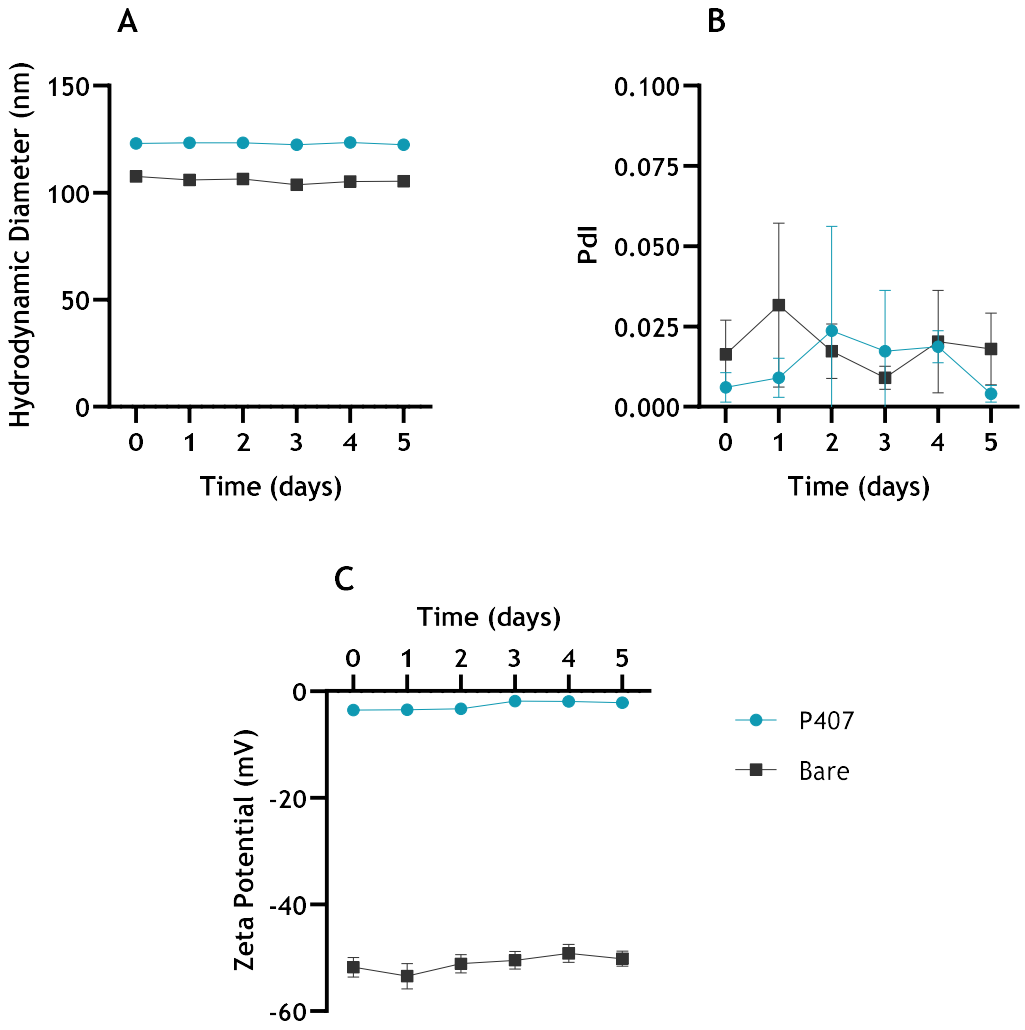


**Figure 15 -** Physiochemical characterization of NPs immediately upon processing and after storage (4 °C in the dark). Results are presented for (A) hydrodynamic diameter, (B) PdI and (C) zeta potential of bare and coated (P407) NPs over time. Symbols and bars represent mean ± SD (*n* = 1), respectively.

## 4.3 Multiple Particle Tracking Analysis

As previously stated, MPT is a technique used for tracking particles in isotropic samples, where the movement of the particle in the *xy* plane allows for extrapolating its transport in the *z* axis [40, 42]. However, MCTS taken as a whole are not considered isotropic samples, due to their complex nature and multiple components (namely cells and ECM) and the different layers (necrotic core, quiescent cells and proliferative cells). Nonetheless, the areas that are analysed by MPT are much smaller in scale, thus making it possible for even complex matrices such as tissues or spheroids to be considered locally isotropic [2-4]. Moreover, videos were acquired in order to contain only one particular layer of the spheroid, thus allowing subsequent analysis by different layers.

### 4.3.1 Whole Spheroids

We initially assessed the possibility of using MPT directly in videos captured from whole spheroids. One expectable limitation, of course, would be the limited visualization of NPs within deeper layers of spheroids due to the numerous cell layers present in the light path. This possibility was further brought forth due to its simplicity and the poor viability of cryosections, as presented above.

Whole spheroids previously incubated with bare and coated NPs were observed using the epifluorescence microscope. The spheroids were directly transferred to the gene frame in the microscope slide before observation. As anticipated, obtaining the goal of 100 trajectories for each condition was impossible in many cases due to the lack of fluorescence and/or signal interference caused by the bulky nature of the spheroid. The dense layer of cells created significant noise, which hindered data acquisition deep into the spheroids. Consequently, all trajectories obtained from different replicates were bundled together and analysed as a single group, for a total of 335, 260, 168 and 104 trajectories for bare NPs in SS conditions, bare NPs in BO conditions, P407 NPs in SS conditions and P407 NPs in BO conditions, respectively.

#### *SS Condition*

Ensemble (Figure 16A, B) and individual (*Annex, Figures A2* and *A3*) analysis of MSD and $D_{eff}$ values showcase a gradual increase of <MSD>, with a slight decrease of $<D_{eff}>$, for both types of NPs. Together, the average anomalous diffusion exponents and the diffusivity ratios reveal that bare NPs ($\alpha$ = 0.42, $D_W/D_{eff}$ = 473) tended to be more mobile than P407 NPs ($\alpha$ = 0.29, $D_W/D_{eff}$ = 508). Transport mode characterization following the aforementioned parameters (Table 1) confirmed that bare NPs had a smaller fraction of immobile NPs (Figure 16C). Over 90% of the P407-modified particles were either immobile or sub-diffusive. The frequency distribution analysis of the anomalous exponent (Figure 16D) determined that for lower values of $\alpha$ ($\alpha \leq 0.4$) there was a greater proportion of coated NPs. Bare NPs featured greater $\alpha$ values more frequently and reached values as high as 1.62, well within the active mode of transport.

Both the <MSD> and $<D_{eff}>$ graphs illustrate the similarity in behaviour of the NPs across the different conditions. The gradual increase of <MSD>, with a slope under 1, is characteristic of particles undergoing sub-diffusive transport [153]. Likewise, the decrease of $<D_{eff}>$ is an indicator of such transport mode [42].

Nonetheless, there were substantial differences between bare and P407 NPs. The anomalous exponent of bare NPs was larger than that of P407 particles, and the diffusivity ratio concurred, depicting that bare NPs were less hindered in their movement. This was compounded by the increase in immobile P407 particles compared to bare NPs, which may justify the larger anomalous exponent of bare NPs. The frequency distribution revealed that the smallest anomalous exponents were found in greater quantity in P407-coated particles, with bare NPs having more frequently trajectories with $\alpha \geq 0.4$. In fact, no P407 NPs had an $\alpha \geq 1.2$, though bare particles reached over 1.60. This type of active behaviour was also surprising, especially with such high values of anomalous exponents. Still, we cannot completely discard that this apparently active mode of transport ($\alpha > 1.20$) could have been induced by improper sample handling that allowed the whole spheroid to shift during video acquisition.

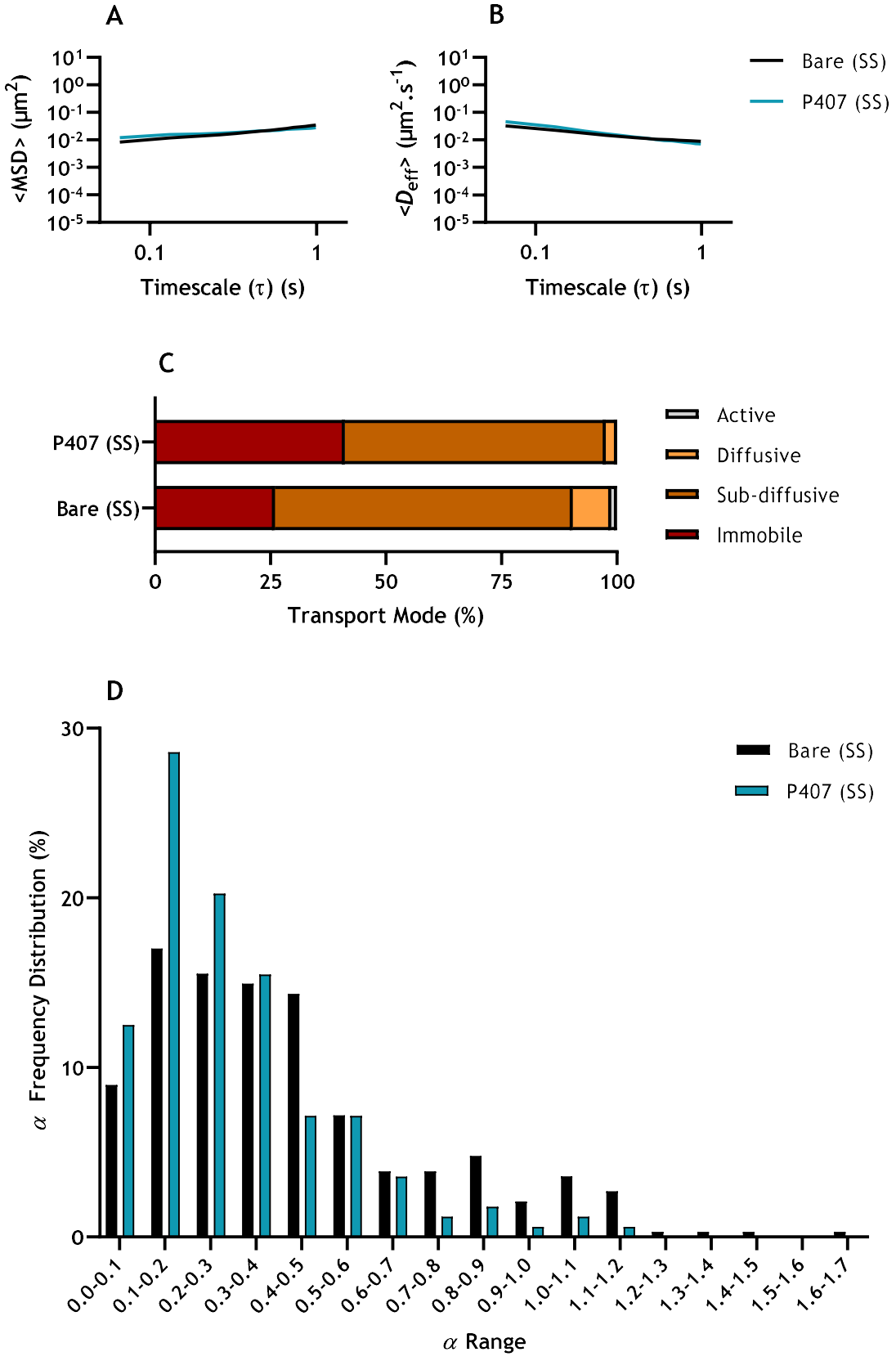


**Figure 16** - Transport behaviour of 100 nm bare ($n$ = 335) and P407 ($n$ = 168) NPs incubated with whole spheroids since cell seeding. Values for (A) <MSD> and (B) $\langle D_{eff} \rangle$ of NPs as a function of time scale. (C) Distribution of NPs according to transport mode. (D) Frequency distribution of anomalous exponents of NPs.

These were unexpected results because, as mentioned before, previous MPT works have overall found that densely PEGylated NPs are able to display enhanced transport and penetration in complex biological matrices, namely tumours [2-4]. However, some reports indicate that tissue penetration of PEGylated NPs can be impaired [9]. Another possibility has to deal with the inability of P407 NPs to maintain their PEG coating throughout incubation with cells and during the formation of the spheroid, despite our *in vitro* data pointing in the opposite direction. Indeed, cell culture media is much more complex than the simple sodium chloride solution used in our studies, with different peptides and proteins present, which have been shown to adhere to NP surface despite the presence of PEG [28]. No previous MPT studies performed in spheroids were found but works that analysed tissue have demonstrated that densely and covalently PEG-modified PS NPs are more mobile than bare ones [2, 4].

## *BO Condition*

Again, ensemble (Figure 17A, B) and individual (*Annex, Figures A4* and *A5*) analysis of MSD and $D_{eff}$ revealed a gradual increase of <MSD> values, with a slight decrease of $<D_{eff}>$ across all samples. Both the average anomalous diffusion exponents and the diffusivity ratios were greater in bare NPs ($\alpha$ = 0.48, $D_W/D_{eff}$ = 544) against coated NPs ($\alpha$ = 0.31, $D_W/D_{eff}$ = 488). The transport mode confirmed that immobile NPs more than doubled with the presence of P407, while there were around three times less active and diffusive coated NPs compared to bare NPs (Figure 17C). Regardless of the condition examined, over 85% of the particles observed were either immobile or sub-diffusive. The frequency distribution of the anomalous exponent (Figure 17D) showed that the adsorbed P407 increased over three times the number of coated NPs with $\alpha \leq 0.1$, with no particles having $\alpha \geq 1.3$. The anomalous exponent of bare NPs, on the other hand, reached over 1.8. There is no specific reason for this type of NPs to reach super-diffusive behaviour. As such, these discrete observations may be related to experimental error or one-off fluid flux within the observation field.

<MSD> and $<D_{eff}>$ graphs illustrate the resemblance in behaviour of the NPs. Once again, there was a gradual increase of <MSD>, and decrease of $<D_{eff}>$, probably because the particles have a sub-diffusive mode of transport. Despite these similarities, there were substantial differences between bare and coated NPs. The anomalous exponent increased 0.17 in bare NPs, which indicated slightly overall greater mobility. However, the increase in anomalous exponent was accompanied by an increase in $D_W/D_{eff}$ for bare NPs, which was unexpected. However, it is possible that the differences in $D_0$ caused by the distinct mean size of the NPs may be responsible for these variations. Nonetheless, the transport mode characterization compounded the conclusions from the anomalous exponent findings, as there was a greater proportion of sub-diffusive, diffusive and active bare NPs. The analysis of frequency distribution data also showed increased mobility of non-coated particles.

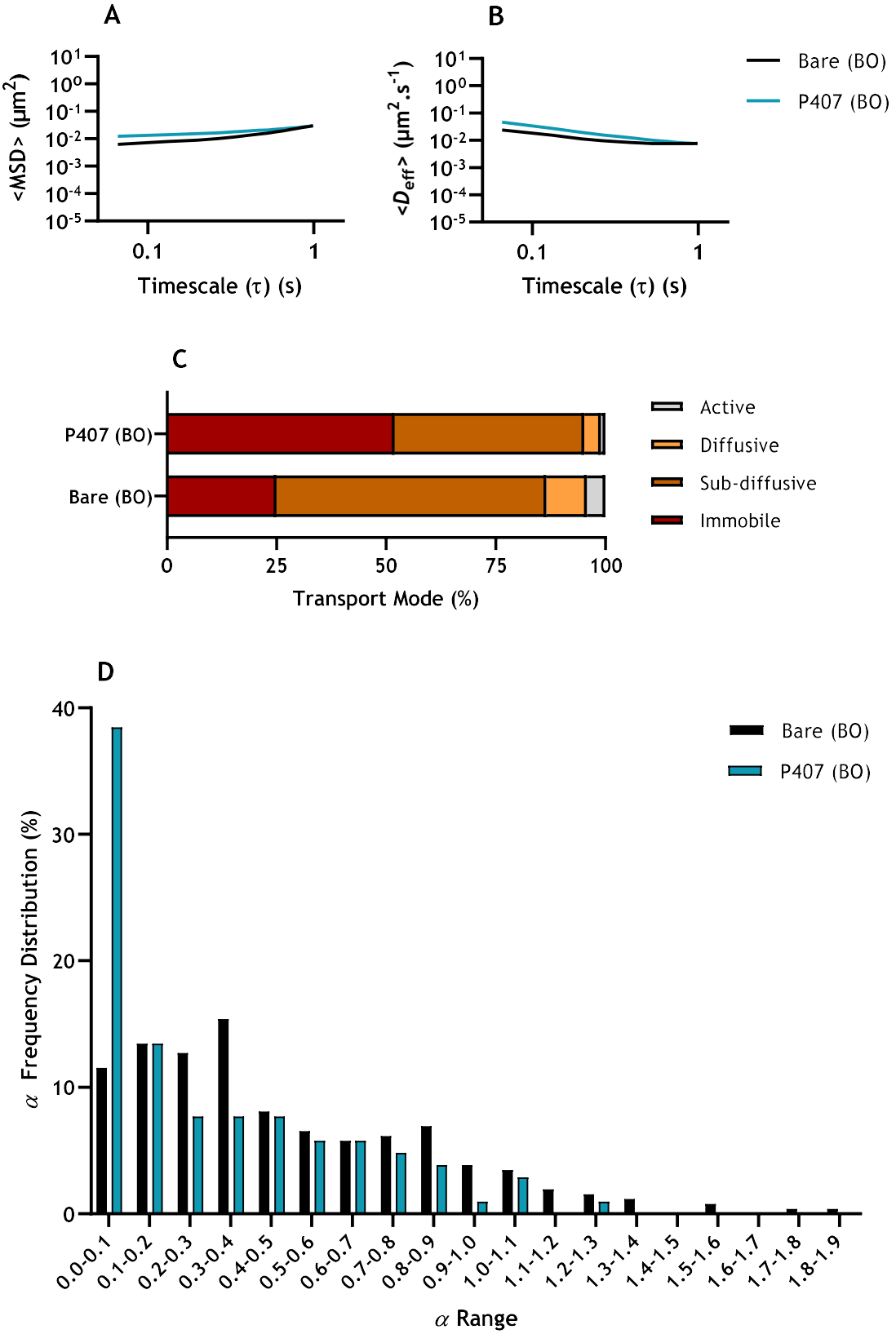


**Figure 17** - Transport behaviour of 100 nm bare ($n$ = 260) and P407 ($n$ = 104) NPs incubated with whole spheroids for 6 h before microscopic observation. Values for (A) <MSD> and (B) $<D_{eff}>$ of NPs as a function of time scale. (C) Distribution of NPs according to transport mode. (D) Frequency distribution of anomalous exponents of NPs.

### *SS vs. BO Conditions*

Results for <MSD> and <$D_{eff}$> under SS and BO conditions were, overall, similar. Still, NPs incubated after spheroid formation trended towards higher anomalous exponents, thus being more mobile (Figure 18). Even so, the transport of both types of NPs can be classified as markedly sub-diffusive.

The transport mode distribution validated the anomalous exponent results, with spheroids of the BO conditions possessing more active and diffusive NPs, even if in scarce numbers. Whereas those from P407 BO conditions also encompassed a greater fraction of immobile NPs compared to its SS counterpart, the increase in active and diffusive particles appeared to offset them. Despite these results, the frequency distribution revealed that most of the NPs with the lowest anomalous exponents are from shorter incubation times. This seems to be counterbalanced by the fact that for diffusive and active behaviour, NPs from the BO conditions were the most frequent.

The differences between movement hindrance in NPs with distinct incubation times may be caused by the protein and peptide adsorption to the NPs, as this phenomenon will exacerbate transport interference [154]. Longer contact with complete media and cells increases the likelihood of protein deposition on the particles, which could perhaps explain the tendency of NPs from BO conditions to be less immobile than particles with longer incubation times. On the other hand, the process of particles disentangling themselves is slow, and not compatible with the 6 h incubation period. A smaller timeframe could lead to trapped NPs not being able to get free, which could substantiate the greater presence of particles with very small anomalous exponents.

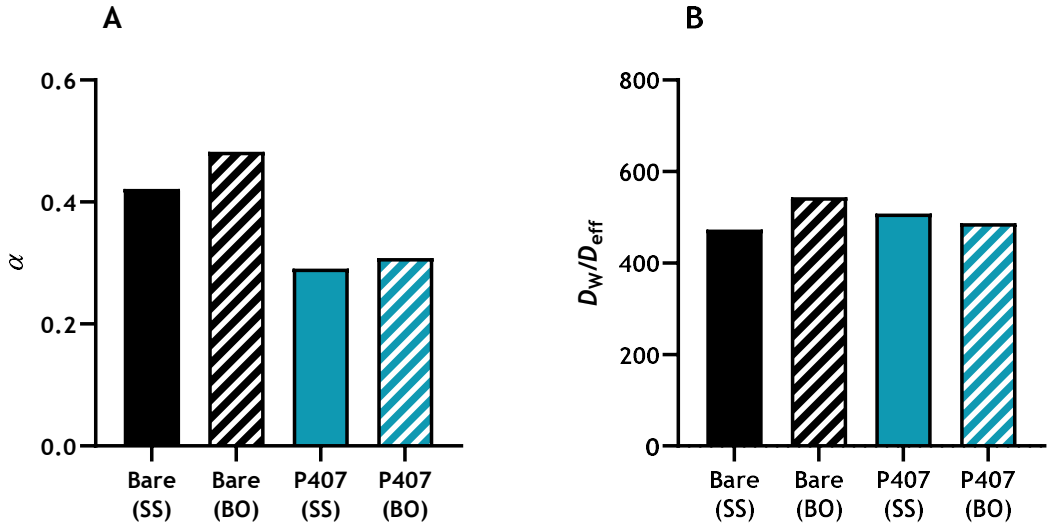


**Figure 18** - Summary of the values of (A) anomalous exponent and (B) diffusivity ratio of NPs in whole spheroids under different incubation conditions (SS or BO). Data presented as mean values ($n$ = 335, $n$ = 260, $n$ = 168 and $n$ = 104 for bare SS, bare BO, P407 SS and P407 BO conditions, respectively).

In short, despite MCTS under BO conditions having a tendency for slightly less immobile particles, this was overshadowed by the large difference between bare and coated NPs where,

despite expectations based on prior studies [3, 4], uncoated NPs appear to have greater overall mobility (Figure 19C-F). Indeed, there is a slight increase in the anomalous exponents of bare NPs, while the diffusivity ratios appear to be similar.

Presented data holds some limitations due to the substantial differences in trajectory number, or even the signal interference in the videos (which could affect the data extracted), as depicted in Figure 19A, B. Indeed, the great discrepancy in the number of trajectories for each condition is an important drawback, which could have affected the reliability of the results. Moreover, the presence of particles depicting active modes of transport may indicate that the samples were not static while being analysed, which may have influenced multiple trajectories. Finally, the interference caused by the numerous cell layers of the spheroids did not allow for the detection of trajectories deep inside the MCTS, merely at the border. Thus, spheroids should be processed to reduce the cell layers being observed, to improve the signal-to-noise ratio, as initially contemplated. Another possibility would be the use of confocal microscopy.

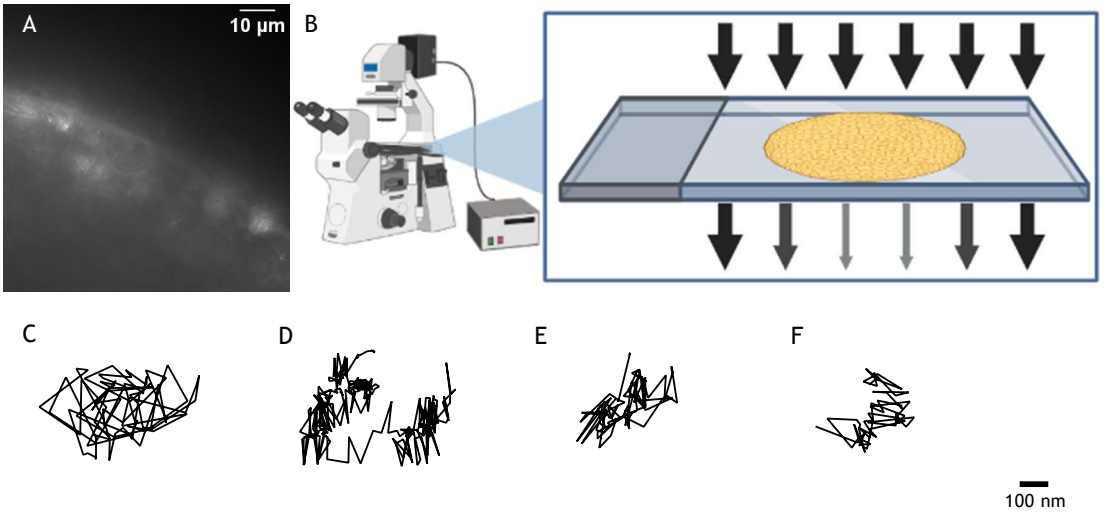


**Figure 19** - (A) Illustrative image of the videos acquired when using whole spheroids (bar = 10 µm). (B) Depiction of the signal interference by the spheroids. Representative trajectories of the (C) bare SS, (D) P407 SS, (E) bare BO and (F) P407 BO conditions in whole spheroids (bar = 100 nm).

## 4.3.2 Spheroid Cryosections

Despite reduced viability, MCTS cryosections were obtained to improve the signal-to-noise ratio by reducing the effect of multiple cell layers in deterring light transmission. Cryosections were chosen according to their closeness to the central plane of the spheroid, to allow for the distinction of three layers: border (proliferative cells), inner layer (quiescent cells) and centre (necrotic core). Due to the greater quality of the acquired videos, trajectories were obtained from each layer, allowing the assessment of differences in NP transport across the various microenvironments. It is also relevant to note that some cryosections had the centre damaged, presenting little to no cells. This could be caused either by the necrotic core of the MCTS having disintegrated in cell medium or from the cryosectioning protocol itself.

## *SS Conditions*

Both ensemble (Figure 20A, B) and individual (*Annex, Figures A6* and *A7*) analysis of MSD and $D_{eff}$ depict a gradual increase of <MSD> values, with a slight decrease of $<D_{eff}>$, regardless of coating. The average anomalous exponents indicate that bare NPs ($\alpha$ = 0.23, $D_W/D_{eff}$ = 3,427) were less immobile than P407 NPs ($\alpha$ = 0.15, $D_W/D_{eff}$ = 1,955), whereas the diffusivity ratio indicated otherwise. Transport mode characterization denotes an increase in sub-diffusive bare NPs in comparison with P407 NPs, which had a greater fraction of immobile NPs (Figure 20C). Regardless of the presence of coating, over 99% of the particles observed were either immobile or sub-diffusive, and no NPs with active transport were detected. The frequency distribution analysis of the anomalous exponent (Figure 20D) showed that P407 only featured a greater percentage for the group of NPs with $\alpha \leq 0.1$, as compared to bare NPs.

<MSD> and $<D_{eff}>$ graphs demonstrated the similarity in behaviour of the NPs across the different conditions, with the slopes of both indicating a sub-diffusive mode of transport. Nonetheless, P407 NPs appeared to have slightly higher <MSD> and $<D_{eff}>$, which indicate enhanced transport. This was in contrast to the anomalous exponent, which was higher for bare NPs, thus suggesting greater mobility. On the other hand, the diffusivity ratio concurred with the ensemble graphs, denoting that uncoated NPs were more hindered in their movement. This could be justified by the distinct $D_0$ values, as stated above. Nevertheless, the upsurge in immobile P407 NPs accedes with the anomalous exponent results. Furthermore, the frequency distribution showcased that coated particles have twice as many trajectories with $\alpha \leq 0.1$ when compared to bare NPs. Indeed, almost 50% of uncoated particles had $\alpha \geq 0.2$, contrasting with the only slightly over 25% of P407 NPs.

These results are in accordance with what was found for whole spheroids. However, the <MSD> and $<D_{eff}>$ plots indicate greater distinction between coated and non-coated NPs when cryosections were used. Additionally, anomalous exponent values were larger in whole MCTS, being almost twice as big in the case of P407 NPs. The frequency distribution and transport modes also showed a trend towards more diffusive and active behaviour when whole spheroids were used. In fact, over 70% of particles in MCTS had an $\alpha \geq 0.2$. Yet, the major distinction was found in the diffusivity ratios, as they were around four times higher in the cryosections. This corroborates the possibility that whole spheroids do not allow for a suitable MPT analysis.

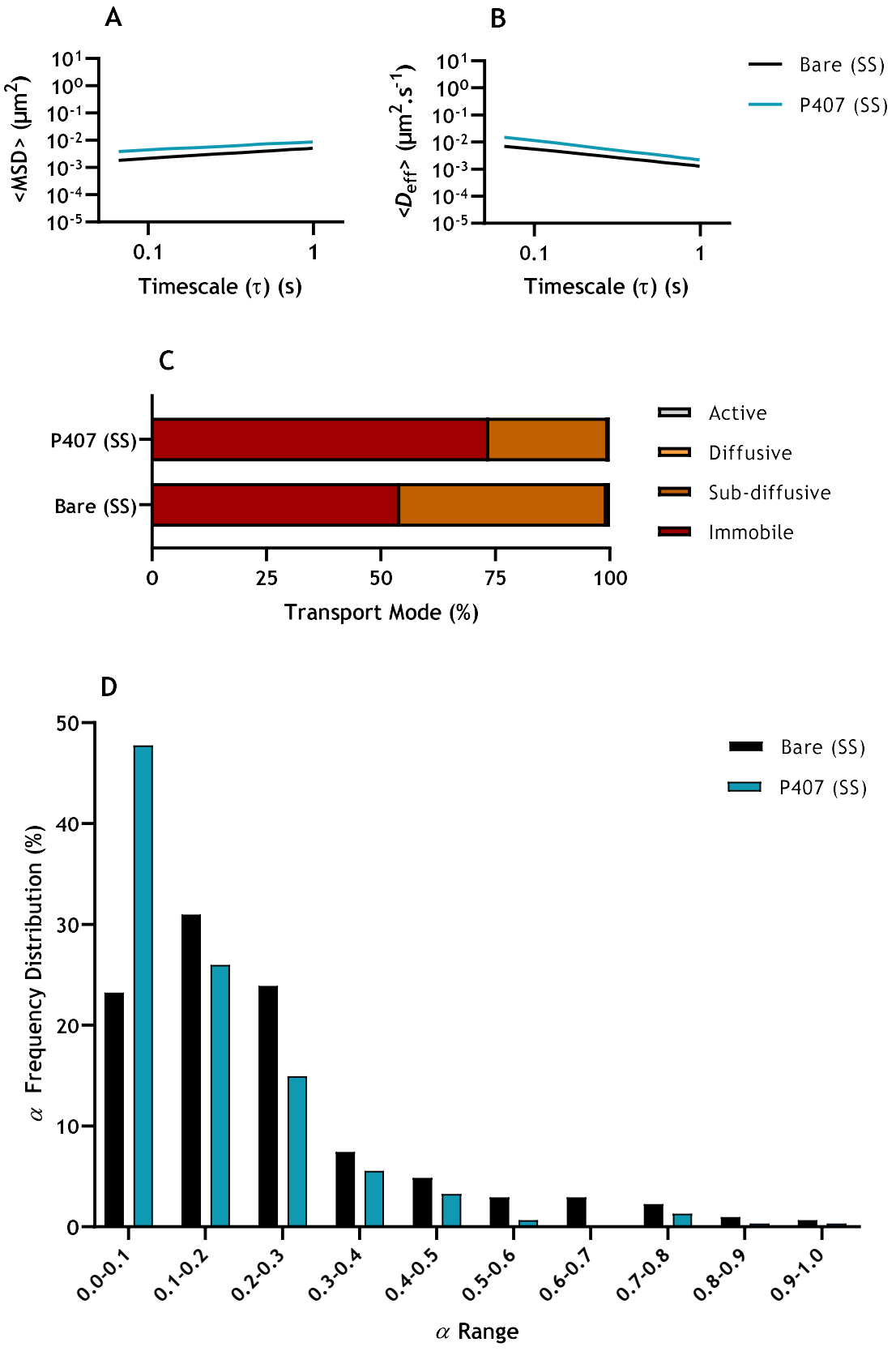


**Figure 20 -** Transport behaviour of 100 nm bare and P407 NPs in MCTS cryosections, after incubation with whole spheroids since cell seeding. Values for (A) <MSD> and (B) $<D_{eff}>$ of NPs as a function of time scale. (C) Distribution of NPs according to transport mode. (D) Frequency distribution of anomalous exponents of NPs. Data presented as mean values (≥100 tracked particles per experiment; *n* = 3).

## *BO Conditions*

Ensemble (Figure 21A, B) and individual (*Annex, Figures A8* and *A9*) analysis of MSD and $D_{eff}$ revealed a gradual increase of <MSD> values, with a very slight decrease of $<D_{eff}>$ in both samples. The average anomalous diffusion exponents and diffusivity ratios were larger in bare NPs ($\alpha$ = 0.27, $D_W/D_{eff}$ = 1,353) comparing to coated NPs ($\alpha$ = 0.20, $D_W/D_{eff}$ = 554). Analysis of the transport mode highlighted the high hindrance to transport, with less than 1% of NPs being diffusive (Figure 21C). The portion of immobile NPs almost doubled when coated with P407. The frequency distribution of the anomalous exponent (Figure 21D) showed that the P407 more than doubled the number of coated NPs with $\alpha \leq 0.1$.

<MSD> and $<D_{eff}>$ graphs depict a great similarity in transport of both types of particles. Once again, there was a gradual increase of <MSD>, and a small decrease of $<D_{eff}>$, which may suggest that while the NPs are sub-diffusive, they might be approaching the range of Brownian motion (diffusive movement). Despite these similarities, values of anomalous exponent were higher for bare NPs. Nonetheless, there was also a large increase in $D_W/D_{eff}$ for bare NPs, which may, once more, be justified by the $D_0$. The transport mode characterization concurred with the anomalous exponent findings, as there was a greater proportion of sub-diffusive bare NPs. Interestingly, the frequency distribution indicated that over 2% of P407 NPs had $0.8 \leq \alpha \leq 1.2$, more than the double of bare particles. Nevertheless, such a small population of NPs has little to no meaning in the overall particle transport. On the other hand, over 60% of P407 NPs had an $\alpha \leq 0.2$, which was probably responsible for the lower average anomalous exponent of these particles.

These findings corroborate the observations in whole MCTS, as P407 NPs were more hindered than bare NPs. The <MSD> and $<D_{eff}>$ graphs were also identical. Once more, the anomalous exponent was greater in whole spheroids, but still allowed to overall classify both types of particles as mostly immobile to sub-diffusive. On the other hand, though the diffusivity ratios of bare NPs in MCTS and P407 particles in spheroids and cryosections are nearly identical, uncoated NPs were more than twice less diffusive in cryosections.

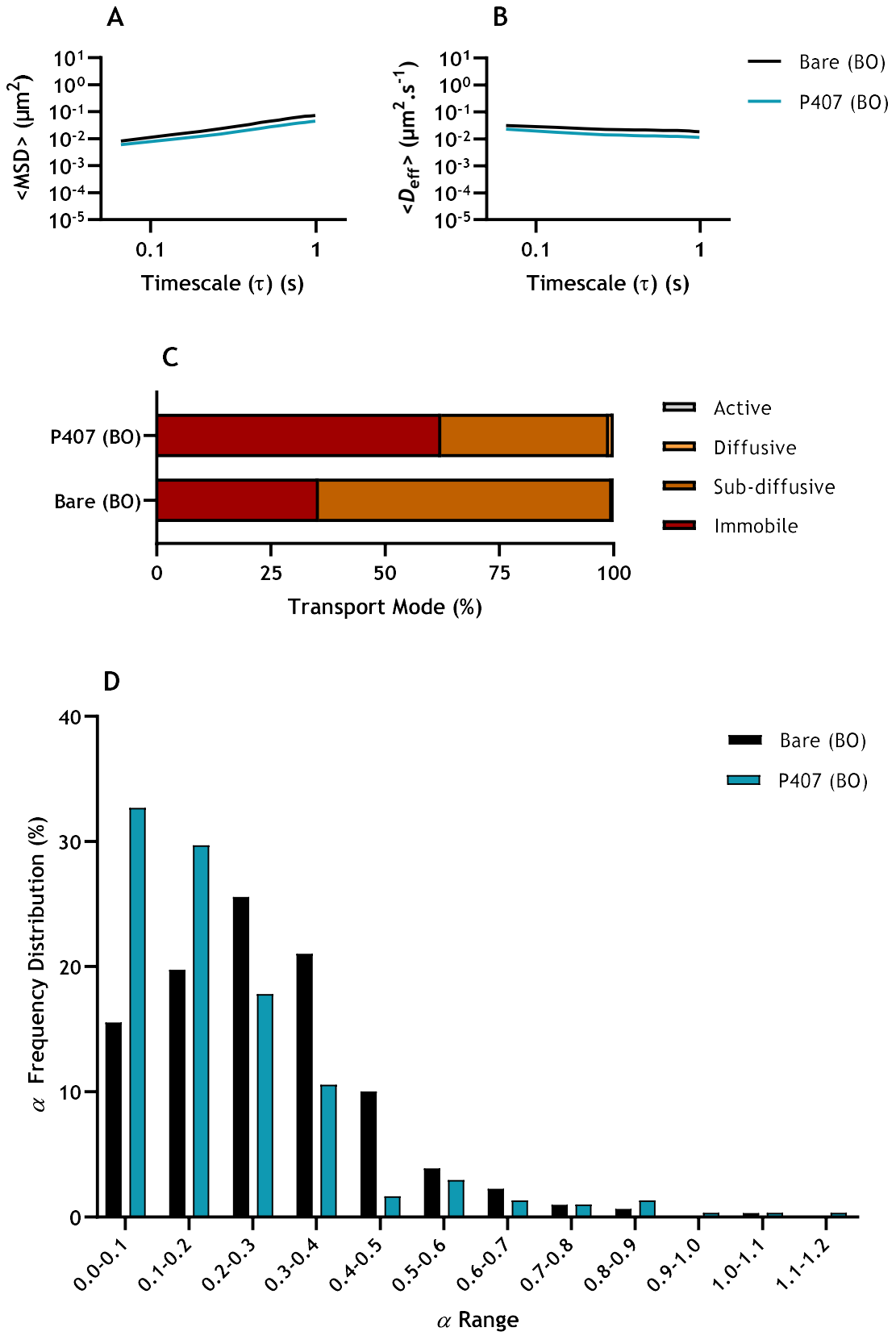


**Figure 21 -** Transport behaviour of 100 nm bare and P407 NPs in MCTS cryosections, after incubation with whole spheroids for 6 h before microscopic observation. Values for (A) <MSD> and (B) <$D_{eff}$> of NPs as a function of time scale. (C) Distribution of NPs according to transport mode. (D) Frequency distribution of anomalous exponents of NPs. Data presented as mean values (≥100 tracked particles per experiment; *n* = 3).

### *SS vs. BO Conditions*

When comparing NPs from both SS and BO conditions, although we observe comparable <MSD> and $<D_{eff}>$ values for every sample, these are systematically superior for NPs incubated for shorter periods of time. The anomalous exponents were also slightly higher, thus indicating a trend towards less immobile NPs, which are substantiated by the decrease in the diffusivity ratio of BO conditions (Figure 22). Analysis of the transport mode distribution validated these findings. Indeed, the two samples with the largest difference in anomalous exponent – P407 SS and bare BO – have a difference of around 40% more immobile particles for coated NPs. Heedless of incubation time, over 90% of P407 NPs featured $\alpha \leq 0.4$, whereas bare particles accounted for less than 85%. For $\alpha \geq 0.3$, almost all anomalous exponent ranges indicated that bare NPs were more frequent. These results can be justified according to the rationale used to explain data obtained using whole spheroids.

Moreover, the behaviour of the particles was similar in both whole MCTS and cryosections. All <MSD> and $<D_{eff}>$ had identical behaviour, even if with lower absolute values for cryosections. Consistently, the anomalous exponent of cryosections was smaller than those calculated for spheroids, while the reverse was true for the diffusivity ratios. An examination of the transport mode reveals similar trends for both biological matrices, despite the larger presence of sub-diffusive, diffusive and active NPs in cryosections. Finally, in complete MCTS, particles had anomalous exponents that reached values of 1.82, and all the conditions had particles that surpassed $\alpha = 1.2$. On the other hand, cryosections arrived at a maximum of $\alpha = 1.16$, with SS conditions capping at $\alpha = 1.0$.

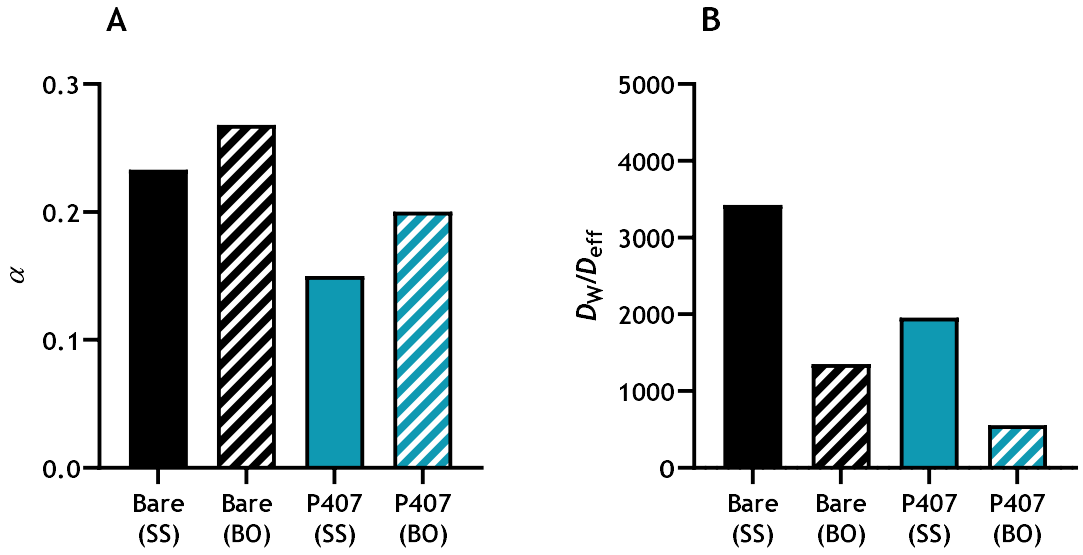


**Figure 22 -** Summary of the values of (A) anomalous exponent and (B) diffusivity ratio in spheroid cryosections under different incubation conditions (SS or BO). Data presented as mean values (≥100 tracked particles per experiment; $n = 3$).

### *Analysis at Different Spheroid Layers*

As stated earlier, cryosections allowed for the acquisition of NPs present at all layers of the MCTS (Figure 23). This allowed performing a sub-analysis of the behaviour of NPs at these different sites. The number of trajectories analysed for each condition can be found in *Annex, Table A1*.

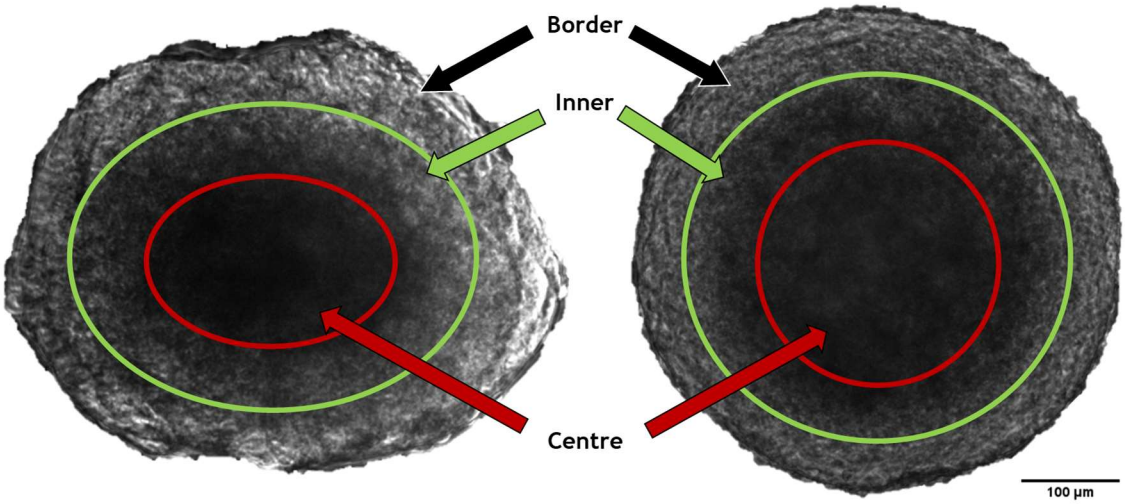


**Figure 23** – Representative microphotographs of two spheroids and their distinctive layers.

We considered both bare and P407 NPs as a whole in the analysis of different layers and $D_W$ of bare NPs for the purpose of calculating $D_W/D_{eff}$. The anomalous exponent tended to decrease deeper within the spheroid (Figure 24). In other words, the less immobile NPs were found in the outer layers. Despite the differences in anomalous exponent being mild, it was sufficient for particles in the necrotic centre of the MCTS to classify as immobile ($\alpha < 0.2$) rather than sub-diffusive. On the other hand, the diffusivity ratio also followed a similar trend, which was incongruent with the findings above. Nonetheless, the diffusivity ratio appeared to differentiate mainly between the border and inside of the MCTS, and its centre. Whereas the movement of particles at the border and inner layer was over 1,300 times slower than in water, it decreased to around 130 times slower than in water when assessing the centre. In other words, according to the diffusivity ratio, the centre had particles that were around 10 times less hindered than in the remaining layers. These results were contradictory and, therefore, we cannot verify which ones are in fact describing the mobility of the NPs without further information.

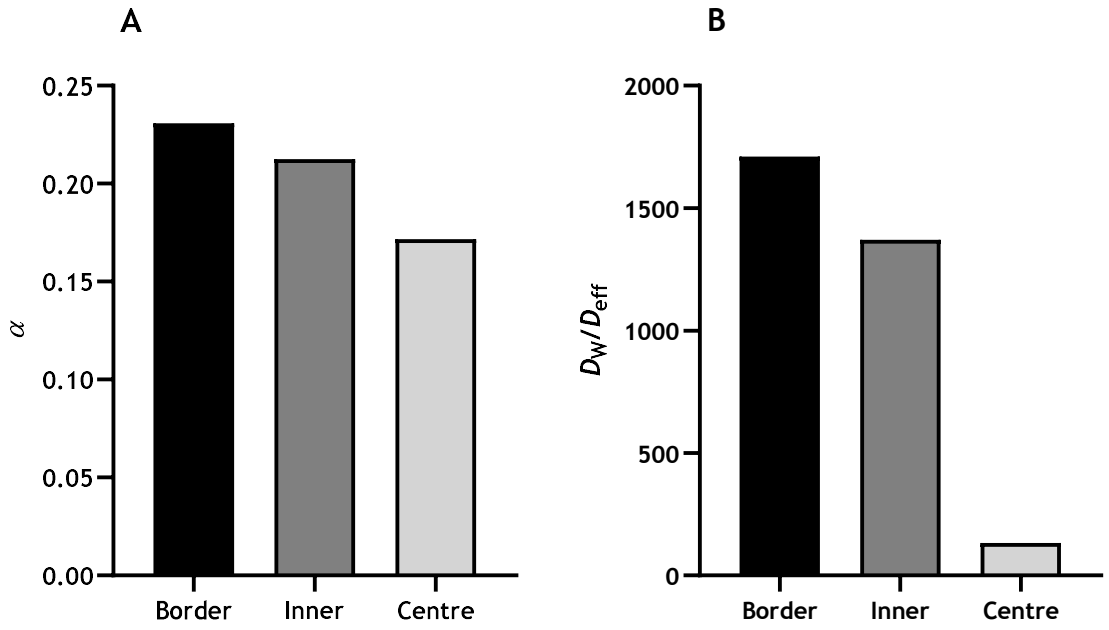


**Figure 24** - Transport behaviour of 100 nm bare or P407 NPs in spheroid cryosections (both SS or BO conditions considered). Distribution of (A) anomalous exponent and (B) diffusivity ratios of NPs across MCTS layers. The number of trajectories analysed in each condition is presented in *Annex, Table A1*.

Consequently, samples were assessed for the incubation time with NPs, in order to ascertain if it could affect particle mobility. Moreover, as it was already established that all samples were more mobile in BO conditions, this segregation in incubation time may provide more information about the veracity of the previous outcomes. As represented in Figure 25, NPs from the BO condition were more mobile, regardless of the spheroid layer, with the exception of the border of the MCTS, according to anomalous exponent values. In this case, the findings were in accordance, as particles incubated for 6 h had usually higher anomalous exponents and consistently lower diffusivity ratios. All samples had a sub-diffusive mode of transport, except for NPs incubated under SS conditions in the inner layer of the MCTS, which were clearly immobile according to the anomalous exponent. The anomalous exponent for NPs in the border and centre of spheroids was similar in both SS and BO conditions. Nonetheless, the diffusivity ratios indicated that particles in BO conditions had decreased movement hindrance across all MCTS layers when comparing to SS conditions. Incubation time notwithstanding, there was an increase in NP transport when assessing further into the cryosection, according to the diffusivity ratios. In fact, in the centre of the spheroid, particles incubated with the MCTS under SS conditions were over 78-times more obstructed in movement than when the incubation time was reduced to 6 h.

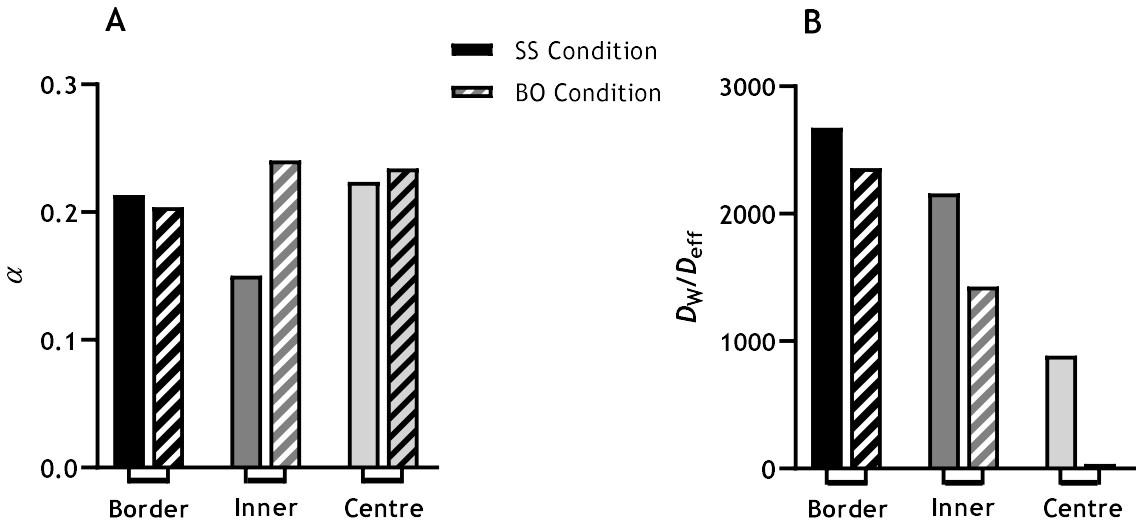


**Figure 25** - Transport behaviour of 100 nm bare or P407 NPs in spheroid cryosections after either SS or BO conditions. Distribution of (A) anomalous exponent and (B) diffusivity ratios of NPs from SS and BO conditions across MCTS layers. The number of trajectories analysed in each condition is presented in *Annex, Table A1.*

Finally, conditions were also discriminated regarding coating of NPs. This will determine the influence of the surface characteristics of NPs on their mobility in each spheroid layer. Ensemble MSD and $D_{eff}$ values (Figure 26) with gradual increase and slight decline, respectively, indicated that the movement of the particles was sub-diffusive and similar in all conditions, except for the centre of the spheroid, where NPs under BO conditions had greater mobility, approaching Brownian motion.

Further evaluation of the anomalous exponent and diffusivity ratios suggested that, akin to what was previously found, bare NPs had a higher anomalous exponent, despite having also generally displayed higher diffusivity ratios (Figure 27). Variations in the anomalous exponent of samples with the same coating were minute, except for P407 NPs in the centre of MCTS. On the other hand, the diffusivity ratios once more generally informed that bare NPs have their movement more hindered than those of coated counterparts, with the exclusion of P407 NPs in the inner layer of spheroids from the BO condition. Moreover, the BO condition in the centre of the spheroid had a very low diffusivity ratio (under 50), whereas the SS condition in the same layer had an increase to over 4,500-times for non-coated NPs. Indeed, only the border appeared to have similar transport for both BO and SS conditions.

Despite the contradictory nature of these findings, the previous <MSD> and <$D_{eff}$> plots, as well as the general conclusions from cryosections, appear to suggest that the anomalous exponent was the more accurate variable in this case. Indeed, based on these assays, the bare and/or BO conditions were more mobile than either P407 particles or spheroids incubated for longer timeframes. This coincides with the assessment of anomalous exponent in the spheroid layers, regardless of the observed layer. In spite of these outcomes, both the ensemble graphs and the diffusivity ratio also pointed to the BO condition on the centre of the MCTS to be much more mobile than other layers. However, this could have been caused by the great disparity in trajectories found in the centre of spheroids from the BO condition, which are less than a third of the trajectories assessed in any other cell layer, incubation time notwithstanding. At the same time, it is possible that the cryosection procedure caused damage to the spheroid layers.

In fact, the centre of some of the cryosections was damaged and had a scarcity of cells, which could be the result of either cell necrosis or an artifact due to the frozen section procedure. Determining the cause of the enhanced NP transport in the centre of cryosections of the BO condition will influence the validity of these findings.

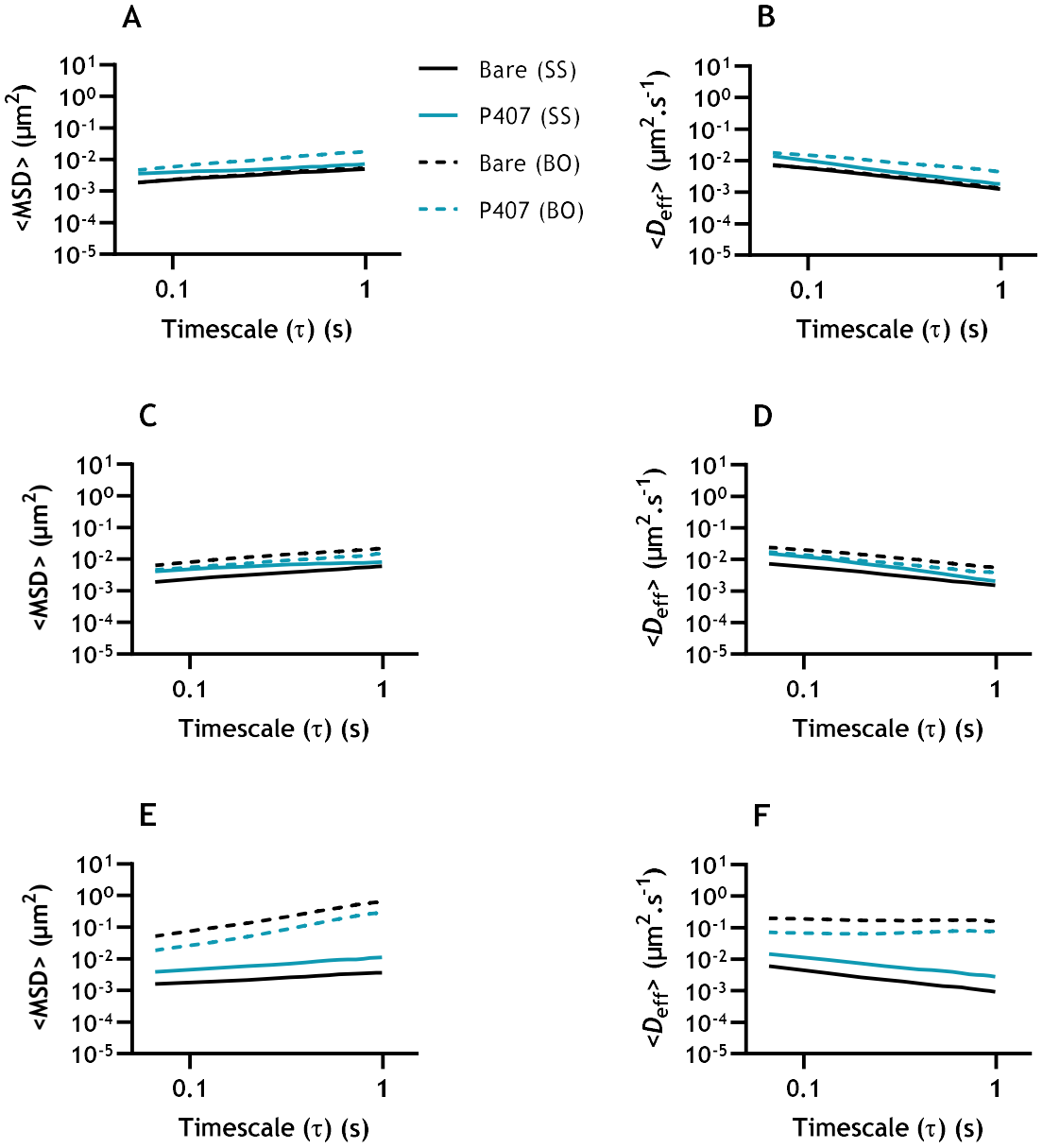


**Figure 26** - Transport behaviour of 100 nm bare and P407 NPs in distinct layers of MCTS cryosections. Values for <MSD> and $<D_{eff}>$ of NPs in the (A, B) border, (C, D) inner layer and (E, F) centre of MCTS cryosections, under SS and BO conditions and as a function of time scale. The number of trajectories analysed in each condition is presented in *Annex, Table A1*.

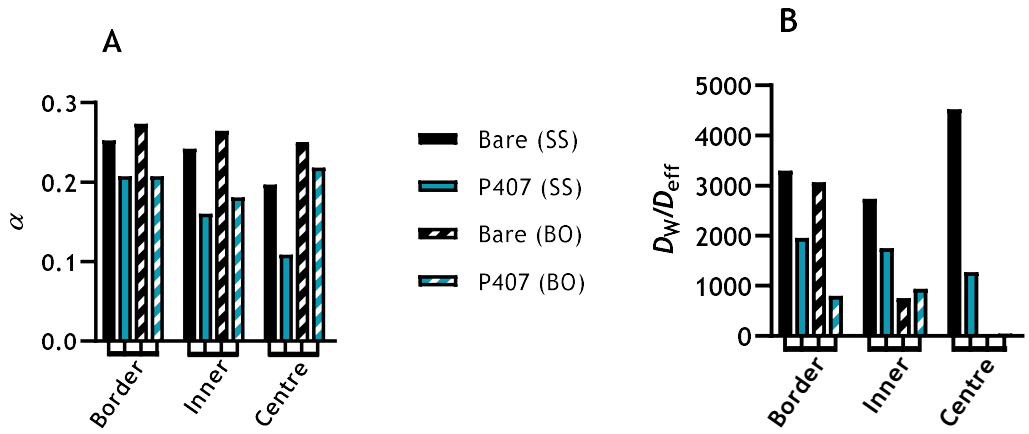


**Figure 27** - Transport behaviour of 100 nm bare and P407 NPs in distinct layers of MCTS cryosections. Distribution of (A) anomalous exponent and (B) diffusivity ratios of bare and P407 NPs from SS and BO conditions across MCTS layers. The number of trajectories analysed in each condition is presented in *Annex, Table A1*.

Overall, cryosections allowed the acquisition of videos with better quality (Figure 28A, B), which facilitated MPT analysis. It also allowed confirming many of the results achieved using whole spheroids, namely the apparently increased mobility of NPs under BO conditions and/or without P407 coating (Figure 28C-F). No particles presented active transport in data resulting from cryosections, which could have three motives: (1) the lack of interference caused by multiple cell layers removed some of the errors that were distorting trajectory data; (2) the proper isolation of the sample; and (3) the cryosection technique led to cell damage, which hindered NP mobility.

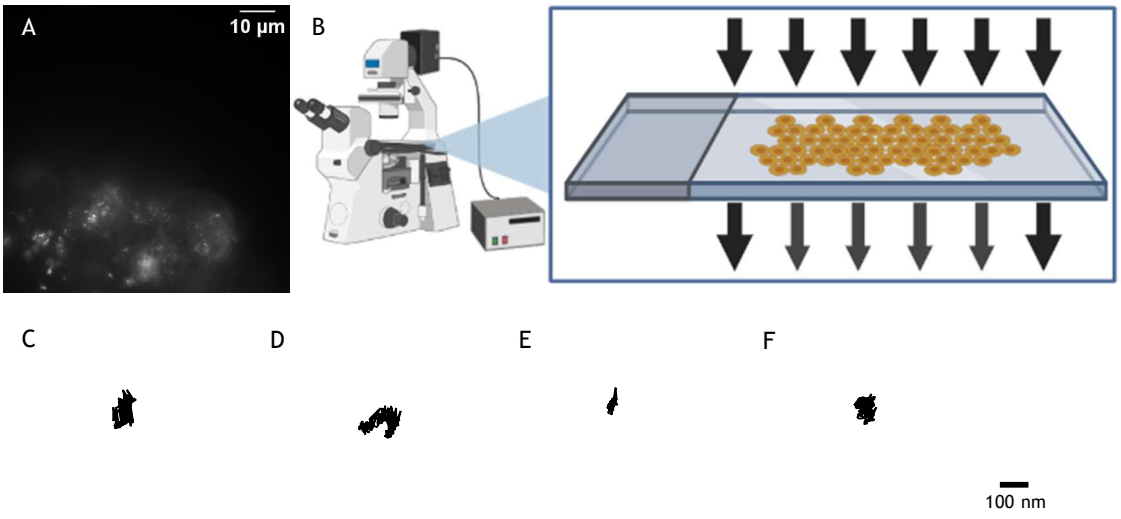


**Figure 28** - (A) Illustrative image of the videos acquired when using cryosections (bar = 10 µm). (B) Depiction of the signal interference by the cryosections. Representative trajectories of the (C) bare SS, (D) P407 SS, (E) bare BO and (F) P407 BO conditions in cryosections (bar = 100 nm).

Analysis of the trajectories according to spheroid layer did not allow for a clear conclusion, mainly due to the contradictory information emerging from anomalous exponent and diffusivity ratio. Nonetheless, bare NPs were yet again shown to be more mobile than their coated counterparts, regardless of spheroid layer. Furthermore, despite prior analysis suggesting that particles with shorter incubation times were more mobile, this was only the case when assessing the inner and central layers of the spheroid. Additional work that could provide a greater number of trajectories may allow the clarification of these questions.

### 4.3.3 Covalently PEG-Modified NPs

Finally, we wanted to confirm the possibility that results for P407 NPs were influenced by de-capping of the PEG-containing polymer. P407 NPs have been previously assessed as diffusive in a mucus surrogate [1], but not in a more complex environment containing cells or complete cell culture media, which may be capable of promoting the faster removal of P407 from the surface of NPs. Such an effect may be responsible for rendering NPs as sub-diffusive.

Contrary to the adsorption of poloxamers, covalent PEG coating of NPs has been shown persistent in biological media, namely in the presence of FBS [30]. To evaluate the hypothesis that P407 was removed from the surface of NPs (thus impairing transport), spheroids were incubated with covalently PEGylated NPs, followed by cryosectioning and observation on the epifluorescence microscope, similarly to what has been described for P407 NPs. PEGylated NPs had mean diameter (around 132 nm) and zeta potential (-4.95 mV) values similar to those of P407 NPs. Due to time constraints, only one series of experiments were conducted for PEGylated NPs: 72 and 54 individual particles were tracked under SS and BO conditions, respectively.

Preliminary data were determined through ensemble (Figure 29A, B) and individual (*Annex*, *Figures A10* and *A11*) analysis of MSD and $D_{eff}$ and suggested a slight increase in NP mobility under BO conditions. Still, both conditions had a gradual increase of <MSD> and decrease of $<D_{eff}>$ with time. Both the average anomalous exponents and diffusivity ratios supported the enhanced transport of particles for the BO conditions ($\alpha$ = 0.30, $D_W/D_{eff}$ = 109) as compared to the SS conditions ($\alpha$ = 0.19, $D_W/D_{eff}$ = 646). The distribution of transport modes reiterated this trend (Figure 29C). Nevertheless, transport was far from being diffusive. The frequency distribution of the anomalous exponents (Figure 29D) established that 90% of NPs under SS conditions presented $\alpha < 0.45$. This percentage was reduced to less than 80% under BO conditions.

Though there is still a decrease in $<D_{eff}>$, likely for the motives previously enumerated, these results appear to support the premise that particles incubated under BO conditions were less immobile in the spheroid than those under SS conditions. This, in turn, is concordant with the findings for P407 and bare NPs in cryosections. Indeed, the fraction of immobile NPs under SS conditions was around twice the fraction of immobile NPs as compared to those from BO conditions, which is reiterated by the breakdown of the frequency distribution of the anomalous exponents.

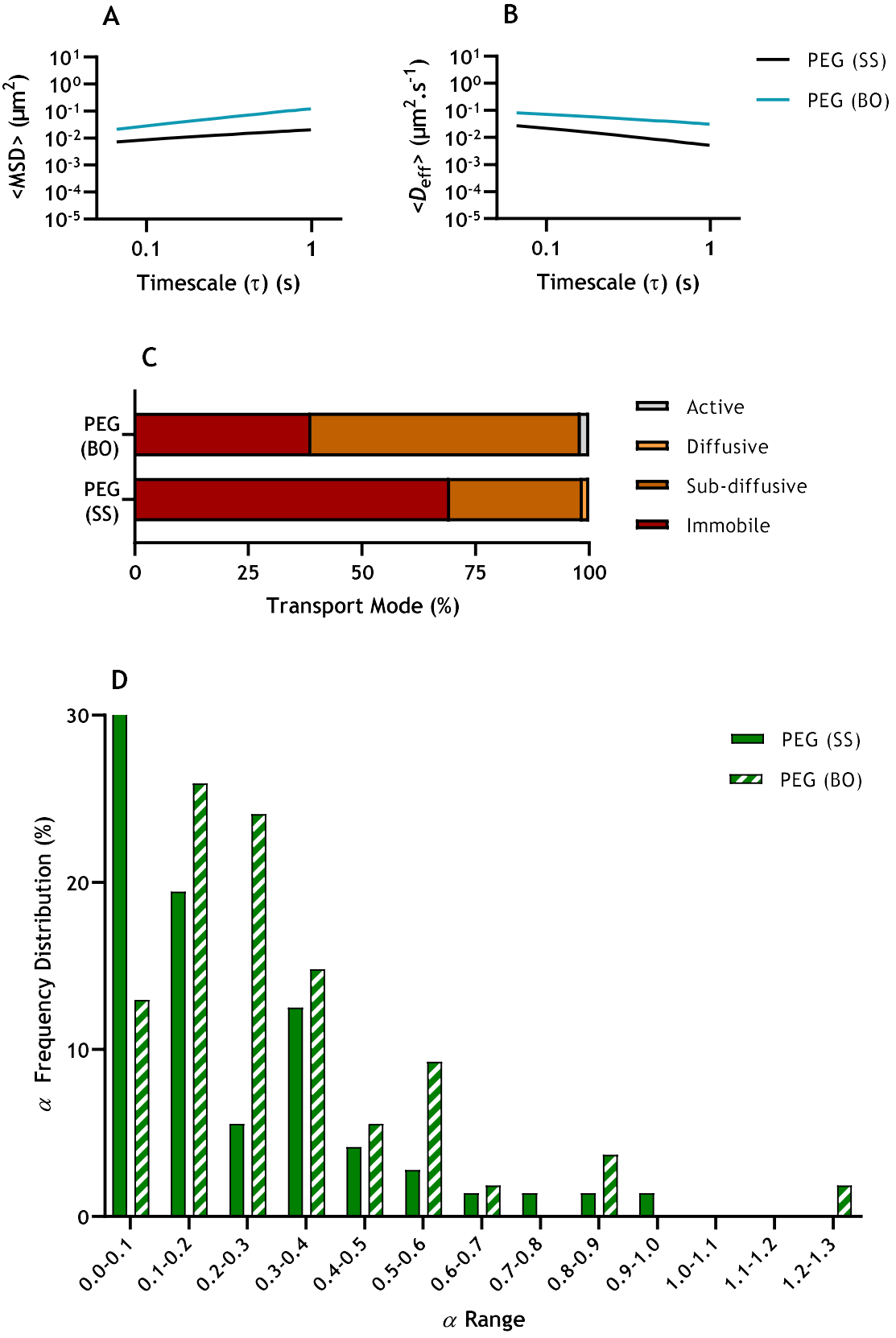


**Figure 29 -** Transport behaviour of 100 nm covalently-bound PEGylated NPs in MCTS cryosections after incubation under SS ($n$ = 72) or BO ($n$ = 54) conditions before analysis. Values for (A) <MSD> and (B) <$D_{eff}$> of NPs as a function of time scale. (C) Distribution of NPs according to transport mode. (D) Frequency distribution of anomalous exponents of NPs.

Importantly, comparison with data from bare and P407 NPs was not conclusive as to relevant difference in transport. Despite the anomalous exponent and the transport mode for PEGylated NPs indicating less mobility than for bare NPs, the diffusivity ratios suggest otherwise. In all cases, however, PEGylated NPs appeared to have increased mobility as compared to P407 NPs, which suggests that at least partial P407 shedding could indeed have occurred. In any case, these data cannot compare to the marked increase in mobility that similar PEGylated NPs had in brain tumour tissue as compared to bare NPs – over 100 times for PLGA NPs [3], and almost 2,400 times for PS NPs [2]. Thus, complementary data on PEGylated NPs is needed.

### 4.3.4 Summary of MPT Studies

The movement of bare and coated NPs in whole and cryosectioned spheroids after different incubation timeframes was evaluated. Regardless of the biological matrix, bare NPs and particles under BO conditions were only slightly more mobile than P407 NPs under SS conditions, respectively. However, the substantial variation in trajectory number, partially caused by the interference of multiple cell layers, which hindered particle detection, undermines more definitive conclusions. Moreover, it was not possible to observe particles in the inside layers of the spheroids, so all findings characterize mainly the mobility of NPs on the border, which may not be representative. Nevertheless, the employment of complete, viable spheroids guaranteed that cells retained the functions necessary for NP transport.

In order to reduce signal obstruction, MCTS were cryosectioned, which greatly increased the particle detail and signal-to-noise ratio of the videos, ensuring that all replicates had at least 100 trajectories for each condition. Nonetheless, the freezing of the spheroids greatly reduces cell viability, which could have a negative impact on the transport behaviour of NPs. Overall results obtained in cryosections indicated slower particle movement even if the overall trends found in whole MCTS were verified. This decrease could indicate that either cryosectioning impacted the movement of associated NPs or that signal interference in whole spheroid observation affected acquired videos and influenced output MPT analysis.

Assessing the impact of distinct spheroid layers only in NP movement led to largely inconclusive results. The incubation time did not seem to influence particle transport at the border of spheroids, but that was not the case over inside layers. The centre of the MCTS had particles that, while categorized as sub-diffusive, had diffusivity ratios under 50. For comparison, in mucus surrogates, NPs with diffusive mode of transport had diffusivity ratios around 10, and the slowest condition, with $\alpha$ = 0.39, had $D_W/D_{eff}$ = 250. Once more, the large discrepancy in the number of analysed trajectories could have altered the output of MPT analysis, and further replicates should be performed.

Finally, preliminary data for covalently-modified PEGylated NPs appears to support that at least partial shedding of poloxamer occurs in P407 NPs incubated with spheroids. Still, results contradicted previous reports that dense PEG-modification can substantially enhance transport in tissue [2-4]. More definitive results are needed to validate these preliminary findings. Nonetheless, there were several distinctions between this work and the indicated studies that could justify these unexpected outcomes, even without considering the biological matrix or the NPs used: (1) the freezing of the spheroids, which was not necessary for breast and brain tissue sectioning; (2) the incubation time of the nanoparticles with the biological matrix was at least

6 hours, in contrast to the minutes in the referred experiments; and (3) the nanoparticles were placed into contact with the tissue after sectioning, whereas the methodology herein described uses spheroids previously incubated with NPs.

# Chapter 5. Conclusions and Future Work

In this work, a protocol capable of characterizing NP movement through MPT analysis of breast cancer spheroids was developed.

Characterization of the NPs determined that they retained similar properties, even after 5 days in storage. Moreover, regardless of the methodology for freezing MCTS for cryosectioning, viability assays demonstrated that it was not possible to maintain cell viability. Consequently, we initially evaluated NP transport in whole spheroids. As expected, the observation of deeper cell layers of the MCTS was greatly restrained. On the other hand, cryosections allowed for visualization and video acquisition of NPs in all spheroid layers, which appeared to propose that the centre of the MCTS had increased NP mobility. Both whole MCTS and cryosections indicated that bare and covalently PEG-modified particles, as well as NPs in BO conditions, had less restricted mobility, but nevertheless presented a sub-diffusive mode of transport. These results support that adsorbed P407 was not entirely retained over time, but are inconsistent with various MPT studies in tumours [2-4].

Additional studies could provide more information regarding these outcomes. Validating the MPT results for whole spheroids may be achieved through confocal microscopy, which might demonstrate that cryosections offer an accurate representation of NP transport in complex biological matrices. Therefore, following an accessible protocol, MPT studies using epifluorescence microscopy could be performed in any kind of tissue. These could help in decoding the natural barriers for NP penetration in specific tissues, and how they may be affected by disease. For instance, this protocol could grant interesting insights regarding the effect of spheroids with multiple cell lines in NP transport. Likewise, studying MCTS representing different BC subtypes, or even other tumour types entirely, might determine whether similar NPs have distinct behaviours in various biological matrices. Moreover, the effect of drugs (either inside or outside the DDS) on NP transport may also be ascertained. In short, the findings achieved from such studies could have a direct impact on the formulations prepared by researchers.

Overall, MPT is a tool to advance the knowledge of NP transport in different biological matrices. The protocol described in this work allowed for the visualization of complex 3D environments, and is applicable to even more intricate biological matrices (e.g., skin, liver, kidneys, etc.). Further refinement, such as thinner cryosections, and the addition of cell staining, could increase the information obtained. Nonetheless, the developed protocol enabled the determination of NP transport in breast cancer spheroids, a new platform for the MPT technique. We were also able to discriminate the mobility of NPs with different coatings and incubation times, even in distinct spheroid layers.

# References


1. Gabriel, L., et al., *MPTHub: An Open-Source Software for Characterizing the Transport of Particles in Biorelevant Media.* Nanomaterials (Basel), 2022. **12**(11).
2. Nance, E.A., et al., *A dense poly(ethylene glycol) coating improves penetration of large polymeric nanoparticles within brain tissue.* Sci Transl Med, 2012. **4**(149): p. 149ra119.
3. Nance, E., et al., *Brain-penetrating nanoparticles improve paclitaxel efficacy in malignant glioma following local administration.* ACS Nano, 2014. **8**(10): p. 10655-64.
4. Dancy, J.G., et al., *Non-specific binding and steric hindrance thresholds for penetration of particulate drug carriers within tumor tissue*. J Control Release, 2016. **238**: p. 139-148.
5. Hanes, J., et al., *Gene Delivery to the Lung*. Drug Delivery System, 2008. **23**.
6. Sung, H., et al., *Global Cancer Statistics 2020: GLOBOCAN Estimates of Incidence and Mortality Worldwide for 36 Cancers in 185 Countries.* CA Cancer J Clin, 2021. **71**(3): p. 209-249.
7. Anselmo, A.C. and S. Mitragotri, *Nanoparticles in the clinic: An update*. Bioeng Transl Med, 2019. **4**(3): p. e10143.
8. Costa, E.C., et al., *3D tumor spheroids: an overview on the tools and techniques used for their analysis.* Biotechnol Adv, 2016. **34**(8): p. 1427-1441.
9. Fujii, S., et al., *Impact of Zwitterionic Polymers on the Tumor Permeability of Molecular Bottlebrush-Based Nanoparticles.* Biomacromolecules, 2022. **23**(7): p. 2846-2855.
10. Ramamurthi, P., et al., *Tuning the Hydrophilic-Hydrophobic Balance of Molecular Polymer Bottlebrushes Enhances their Tumor Homing Properties.* Adv Healthc Mater, 2022. **11**(12): p. e2200163.
11. Patil, M., D.S. Mehta, and S. Guvva, *Future impact of nanotechnology on medicine and dentistry.* J Indian Soc Periodontol, 2008. **12**(2): p. 34-40.
12. Goncalves, B.C., et al., *Antiviral therapies: advances and perspectives.* Fundam Clin Pharmacol, 2021. **35**(2): p. 305-320.
13. Cano, A., et al., *State-of-the-art polymeric nanoparticles as promising therapeutic tools against human bacterial infections.* J Nanobiotechnology, 2020. **18**(1): p. 156.

14. Baetke, S.C., T. Lammers, and F. Kiessling, *Applications of nanoparticles for diagnosis and therapy of cancer*. Br J Radiol, 2015. **88**(1054): p. 20150207.
15. Shen, Z., et al., *1 - PEGylated "stealth" nanoparticles and liposomes*, in *Engineering of Biomaterials for Drug Delivery Systems*, A. Parambath, Editor. 2018, Woodhead Publishing. p. 1-26.
16. Zein, R., W. Sharrouf, and K. Selting, *Physical Properties of Nanoparticles That Result in Improved Cancer Targeting*. J Oncol, 2020. **2020**: p. 5194780.
17. Ganesan, K., et al., *Targeting Engineered Nanoparticles for Breast Cancer Therapy*. Pharmaceutics, 2021. **13**(11).
18. Huang, K., et al., *Size-dependent localization and penetration of ultrasmall gold nanoparticles in cancer cells, multicellular spheroids, and tumors in vivo*. ACS Nano, 2012. **6**(5): p. 4483-93.
19. Yang, Q. and S.K. Lai, *Anti-PEG immunity: emergence, characteristics, and unaddressed questions*. Wiley Interdiscip Rev Nanomed Nanobiotechnol, 2015. **7**(5): p. 655-77.
20. Neagu, M., et al., *Protein bio-corona: critical issue in immune nanotoxicology*. Arch Toxicol, 2017. **91**(3): p. 1031-1048.
21. Huckaby, J.T. and S.K. Lai, *PEGylation for enhancing nanoparticle diffusion in mucus*. Adv Drug Deliv Rev, 2018. **124**: p. 125-139.
22. Sharma, R., et al., *Chapter 13 - Engineered nanoparticles as a precise delivery system in cancer therapeutics*, in *Engineering of Nanobiomaterials*, A.M. Grumezescu, Editor. 2016, William Andrew Publishing. p. 397-427.
23. Suk, J.S., et al., *PEGylation as a strategy for improving nanoparticle-based drug and gene delivery*. Adv Drug Deliv Rev, 2016. **99**(Pt A): p. 28-51.
24. Zierden, H.C., et al., *Avoiding a Sticky Situation: Bypassing the Mucus Barrier for Improved Local Drug Delivery*. Trends Mol Med, 2021.
25. Lai, S.K., et al., *Rapid transport of large polymeric nanoparticles in fresh undiluted human mucus*. Proc Natl Acad Sci U S A, 2007. **104**(5): p. 1482-7.
26. Suk, J.S., et al., *The penetration of fresh undiluted sputum expectorated by cystic fibrosis patients by non-adhesive polymer nanoparticles*. Biomaterials, 2009. **30**(13): p. 2591-7.
27. Hoang Thi, T.T., et al., *The Importance of Poly(ethylene glycol) Alternatives for Overcoming PEG Immunogenicity in Drug Delivery and Bioconjugation*. Polymers (Basel), 2020. **12**(2).
28. Perera, Y.R., et al., *Understanding the Adsorption of Peptides and Proteins onto PEGylated Gold Nanoparticles*. Molecules, 2021. **26**(19).
29. Li, M., et al., *Brush Conformation of Polyethylene Glycol Determines the Stealth Effect of Nanocarriers in the Low Protein Adsorption Regime*. Nano Lett, 2021. **21**(4): p. 1591-1598.
30. Partikel, K., et al., *Effect of nanoparticle size and PEGylation on the protein corona of PLGA nanoparticles*. Eur J Pharm Biopharm, 2019. **141**: p. 70-80.
31. Braeckmans, K., et al., *Measuring molecular dynamics by FRAP, FCS, and SPT*, in *Optical Fluorescence Microscopy*, A. Diaspro, Editor. 2010, Springer. p. 153-163.
32. Huang, F., et al., *Quantitative nanoparticle tracking: applications to nanomedicine*. Nanomedicine (Lond), 2011. **6**(4): p. 693-700.

33. Pincet, F., et al., *FRAP to Characterize Molecular Diffusion and Interaction in Various Membrane Environments*. PLoS One, 2016. **11**(7): p. e0158457.
34. Hao, T., *Chapter 6 - Physics of electrorheological fluids*, in *Studies in Interface Science*, T. Hao, Editor. 2005, Elsevier. p. 235-340.
35. Lenser, T., et al., *Chapter 1 - Fluorescence Fluctuation Microscopy to Reveal 3D Architecture and Function in the Cell Nucleus*, in *Methods in Cell Biology*, G.V. Shivashankar, Editor. 2010, Academic Press. p. 2-33.
36. Berglund, A. and H. Mabuchi, *Tracking-FCS: Fluorescence correlation spectroscopy of individual particles*. Optics Express, 2005. **13**.
37. Palazzo, G. and L. Paduano, *Chapter 10 - Diffusion measuring techniques*, in *Colloidal Foundations of Nanoscience (Second Edition)*, D. Berti and G. Palazzo, Editors. 2022, Elsevier: Amsterdam. p. 257-287.
38. Manzo, C. and M.F. Garcia-Parajo, *A review of progress in single particle tracking: from methods to biophysical insights*. Rep Prog Phys, 2015. **78**(12): p. 124601.
39. McGlynn, J.A., N. Wu, and K.M. Schultz, *Multiple particle tracking microrheological characterization: Fundamentals, emerging techniques and applications*. Journal of Applied Physics, 2020. **127**(20): p. 201101.
40. Kim, A.J. and J. Hanes, *The emergence of multiple particle tracking in intracellular trafficking of nanomedicines*. Biophysical Reviews, 2012. **4**(2): p. 83-92.
41. Savin, T., *Multiple Particle Tracking to Assess the Microstructure of Biological Fluids*, in *Department of Chemical Engineering*. 2006, Massachusetts Institute of Technology: Unpublished.
42. Suh, J., M. Dawson, and J. Hanes, *Real-time multiple-particle tracking: applications to drug and gene delivery*. Adv Drug Deliv Rev, 2005. **57**(1): p. 63-78.
43. Verdugo, P., *Mucus supramolecular topology: an elusive riddle*. Proc Natl Acad Sci U S A, 2012. **109**(44): p. E2956; author reply E2957.
44. Ensign, L.M., et al., *Ex vivo characterization of particle transport in mucus secretions coating freshly excised mucosal tissues*. Mol Pharm, 2013. **10**(6): p. 2176-82.
45. Suh, J., et al., *PEGylation of nanoparticles improves their cytoplasmic transport*. Int J Nanomedicine, 2007. **2**(4): p. 735-41.
46. Schuster, B.S., et al., *Particle tracking in drug and gene delivery research: State-of-the-art applications and methods*. Adv Drug Deliv Rev, 2015. **91**: p. 70-91.
47. Lai, S.K., et al., *Altering mucus rheology to "solidify" human mucus at the nanoscale*. PLoS One, 2009. **4**(1): p. e4294.
48. Daviran, M., et al., *Measuring the Effects of Cytokines on the Modification of Pericellular Rheology by Human Mesenchymal Stem Cells*. ACS Biomater Sci Eng, 2021. **7**(12): p. 5762-5774.
49. McKenna, M., et al., *Multiple Particle Tracking Detects Changes in Brain Extracellular Matrix and Predicts Neurodevelopmental Age*. ACS Nano, 2021. **15**(5): p. 8559-8573.
50. Lill, Y., et al., *Single hepatitis-B virus core capsid binding to individual nuclear pore complexes in Hela cells*. Biophys J, 2006. **91**(8): p. 3123-30.
51. Furst, E.M. and T.M. Squires, *Multiple Particle Tracking*, in *Microrheology*, E.M. Furst and T.M. Squires, Editors. 2017, Oxford University Press: Oxford.

52. Rose, K.A., et al., *Particle tracking of nanoparticles in soft matter*. Journal of Applied Physics, 2020. **127**(19): p. 191101.
53. Savin, T. and P.S. Doyle, *Static and dynamic errors in particle tracking microrheology*. Biophys J, 2005. **88**(1): p. 623-38.
54. Crater, J.S. and R.L. Carrier, *Barrier properties of gastrointestinal mucus to nanoparticle transport*. Macromol Biosci, 2010. **10**(12): p. 1473-83.
55. Hoang, T., et al., *The cervicovaginal mucus barrier to HIV-1 is diminished in bacterial vaginosis*. PLoS Pathog, 2020. **16**(1): p. e1008236.
56. Sharma, R., *Breast cancer incidence, mortality and mortality-to-incidence ratio (MIR) are associated with human development, 1990-2016: evidence from Global Burden of Disease Study 2016*. Breast Cancer, 2019. **26**(4): p. 428-445.
57. Ferlay, J., et al., *Cancer statistics for the year 2020: An overview*. Int J Cancer, 2021.
58. Feiten, S., et al., *Breast cancer morbidity: questionnaire survey of patients on the long term effects of disease and adjuvant therapy*. Dtsch Arztebl Int, 2014. **111**(31-32): p. 537-44.
59. Hayes, S.C., et al., *Upper-body morbidity after breast cancer: incidence and evidence for evaluation, prevention, and management within a prospective surveillance model of care*. Cancer, 2012. **118**(8 Suppl): p. 2237-49.
60. Perou, C.M., et al., *Molecular portraits of human breast tumours*. Nature, 2000. **406**(6797): p. 747-52.
61. Sorlie, T., et al., *Gene expression patterns of breast carcinomas distinguish tumor subclasses with clinical implications*. Proc Natl Acad Sci U S A, 2001. **98**(19): p. 10869-74.
62. Cancer Genome Atlas Network, *Comprehensive molecular portraits of human breast tumours*. Nature, 2012. **490**(7418): p. 61-70.
63. Lukasiewicz, S., et al., *Breast Cancer-Epidemiology, Risk Factors, Classification, Prognostic Markers, and Current Treatment Strategies-An Updated Review*. Cancers (Basel), 2021. **13**(17).
64. Dai, X.F., et al., *Breast cancer intrinsic subtype classification, clinical use and future trends*. American Journal of Cancer Research, 2015. **5**(10): p. 2929-2943.
65. Sotiriou, C., et al., *Breast cancer classification and prognosis based on gene expression profiles from a population-based study*. Proc Natl Acad Sci U S A, 2003. **100**(18): p. 10393-8.
66. Sorlie, T., et al., *Repeated observation of breast tumor subtypes in independent gene expression data sets*. Proc Natl Acad Sci U S A, 2003. **100**(14): p. 8418-23.
67. Engstrom, M.J., et al., *Molecular subtypes, histopathological grade and survival in a historic cohort of breast cancer patients*. Breast Cancer Res Treat, 2013. **140**(3): p. 463-73.
68. Prat, A., et al., *Clinical implications of the intrinsic molecular subtypes of breast cancer*. Breast, 2015. **24 Suppl 2**: p. S26-35.
69. Cardoso, F., et al., *Early breast cancer: ESMO Clinical Practice Guidelines for diagnosis, treatment and follow-updagger*. Ann Oncol, 2019. **30**(8): p. 1194-1220.
70. Lloyd, M.R., et al., *Next-generation selective estrogen receptor degraders and other novel endocrine therapies for management of metastatic hormone receptor-positive*

*breast cancer: current and emerging role*. Ther Adv Med Oncol, 2022. **14**: p. 17588359221113694.

71. Wang, J. and B. Xu, *Targeted therapeutic options and future perspectives for HER2-positive breast cancer*. Signal Transduct Target Ther, 2019. **4**: p. 34.
72. Heil, J., et al., *Eliminating the breast cancer surgery paradigm after neoadjuvant systemic therapy: current evidence and future challenges*. Ann Oncol, 2020. **31**(1): p. 61-71.
73. Rodríguez, F., et al. *Nano-Based Approved Pharmaceuticals for Cancer Treatment: Present and Future Challenges*. Biomolecules, 2022. **12**, DOI: 10.3390/biom12060784.
74. Lyseng-Williamson, K.A., *Trastuzumab Emtansine: A Review of Its Adjuvant Use in Residual Invasive HER2-Positive Early Breast Cancer*. Drugs, 2020. **80**(16): p. 1723-1730.
75. Green, M.R., et al., *Abraxane, a novel Cremophor-free, albumin-bound particle form of paclitaxel for the treatment of advanced non-small-cell lung cancer*. Ann Oncol, 2006. **17**(8): p. 1263-8.
76. Jiang, G., et al., *Comprehensive comparison of molecular portraits between cell lines and tumors in breast cancer*. BMC Genomics, 2016. **17 Suppl 7**: p. 525.
77. Holliday, D.L. and V. Speirs, *Choosing the right cell line for breast cancer research*. Breast Cancer Res, 2011. **13**(4): p. 215.
78. Zanoni, M., et al., *Modeling neoplastic disease with spheroids and organoids*. J Hematol Oncol, 2020. **13**(1): p. 97.
79. Ryan, S.L., et al., *Drug Discovery Approaches Utilizing Three-Dimensional Cell Culture*. Assay Drug Dev Technol, 2016. **14**(1): p. 19-28.
80. Nunes, A.S., et al., *3D tumor spheroids as in vitro models to mimic in vivo human solid tumors resistance to therapeutic drugs*. Biotechnol Bioeng, 2019. **116**(1): p. 206-226.
81. Shen, H., et al., *Recent Advances in Three-Dimensional Multicellular Spheroid Culture and Future Development*. Micromachines (Basel), 2021. **12**(1).
82. Pontiggia, O., et al., *The tumor microenvironment modulates tamoxifen resistance in breast cancer: a role for soluble stromal factors and fibronectin through beta1 integrin*. Breast Cancer Res Treat, 2012. **133**(2): p. 459-71.
83. Achilli, T.M., J. Meyer, and J.R. Morgan, *Advances in the formation, use and understanding of multi-cellular spheroids*. Expert Opin Biol Ther, 2012. **12**(10): p. 1347-60.
84. Bangde, P., et al., *Trimethyl chitosan coated palladium nanoparticles as a photothermal agent and its in vitro evaluation in 2D and 3D model of breast cancer cells*. Colloids Surf B Biointerfaces, 2022. **211**: p. 112287.
85. Murphy, D.A., et al., *Reversing Hypoxia with PLGA-Encapsulated Manganese Dioxide Nanoparticles Improves Natural Killer Cell Response to Tumor Spheroids*. Mol Pharm, 2021. **18**(8): p. 2935-2946.
86. Nieto, C., M.A. Vega, and E. Martin Del Valle, *Nature-Inspired Nanoparticles as Paclitaxel Targeted Carrier for the Treatment of HER2-Positive Breast Cancer*. Cancers (Basel), 2021. **13**(11).
87. Merriam-Webster, *Histology*, in *Merriam-Webster.com dictionary*. n.d.
88. Vachet, R.W., *More than a picture*. Nature Nanotechnology, 2015. **10**(2): p. 103-104.

89. Griffiths, A.M., *Challenging Question: Can We Diagnose Crohn's Disease without Histology?* Digestive Diseases, 2013. **31**(2): p. 202-206.
90. Garcia, J.G., M.M. Picken, and R.C. Flanigan, *The importance of histology and cytogenetics in decision making for renal cell carcinoma.* World J Urol, 2008. **26**(2): p. 155-60.
91. Regueiro, F., et al., *The importance of histology in the evaluation of pulmonary transplantation: carcinomatous lymphangitis.* Thorac Cardiovasc Surg, 2005. **53**(2): p. 122-3.
92. Alturkistani, H.A., F.M. Tashkandi, and Z.M. Mohammedsaleh, *Histological Stains: A Literature Review and Case Study.* Glob J Health Sci, 2015. **8**(3): p. 72-9.
93. Exbrayat, J.M., *Microscopy: Light Microscopy and Histochemical Methods*, in *Encyclopedia of Food and Health*, B. Caballero, P.M. Finglas, and F. Toldrá, Editors. 2016, Academic Press: Oxford. p. 715-723.
94. Miko, M. and I. Varga, *Chapter 6 - Histologic Examination of Peripheral Nerves*, in *Nerves and Nerve Injuries*, R.S. Tubbs, et al., Editors. 2015, Academic Press: San Diego. p. 79-89.
95. Cooper, J.A., et al., *4 - Assays for determining cell differentiation in biomaterials*, in *Characterization of Biomaterials*, M. Jaffe, et al., Editors. 2013, Woodhead Publishing. p. 101-137.
96. Pawlina, W., *Chapter 1 - Methods*, in *Histology : a text and atlas : with correlated cell and molecular biology*, M.H. Ross and W. Pawlina, Editors. 2016, Wolters Kluwer Health: Philadelphia. p. 1-22.
97. Mathieson, W. and G. Thomas, *Using FFPE Tissue in Genomic Analyses: Advantages, Disadvantages and the Role of Biospecimen Science.* Current Pathobiology Reports, 2019. **7**(3): p. 35-40.
98. Baskin, D.G., *Fixation and Tissue Processing in Immunohistochemistry*, in *Pathobiology of Human Disease*, L.M. McManus and R.N. Mitchell, Editors. 2014, Academic Press: San Diego. p. 3797-3806.
99. Heiligenstein, X. and M.S. Lucas, *One for All, All for One: A Close Look at In-Resin Fluorescence Protocols for CLEM.* Front Cell Dev Biol, 2022. **10**: p. 866472.
100. Rousselle, S.D., et al., *Histology Strategies for Medical Implants and Interventional Device Studies.* Toxicol Pathol, 2019. **47**(3): p. 235-249.
101. Krenacs, T., et al., *How we process trephine biopsy specimens: epoxy resin embedded bone marrow biopsies.* J Clin Pathol, 2005. **58**(9): p. 897-903.
102. Sousa, A.L., et al., *Chapter 2 - The Histo-CLEM Workflow for tissues of model organisms*, in *Methods in Cell Biology*, T. Müller-Reichert and P. Verkade, Editors. 2021, Academic Press. p. 13-37.
103. Abdelaal, H.M., et al., *Comparison of Vibratome and Compresstome sectioning of fresh primate lymphoid and genital tissues for in situ MHC-tetramer and immunofluorescence staining.* Biol Proced Online, 2015. **17**(1): p. 2.
104. Gal, A.A., *The centennial anniversary of the frozen section technique at the Mayo Clinic.* Arch Pathol Lab Med, 2005. **129**(12): p. 1532-5.
105. Bloodgood, J.C., *THE DANGER OF INCOMPLETE REMOVAL OF SMALL AND APPARENTLY INNOCENT LESIONS.* Journal of the American Medical Association, 1926. **87**(5): p. 344-345.

106. Wright, J.R., Jr., *The development of the frozen section technique, the evolution of surgical biopsy, and the origins of surgical pathology.* Bull Hist Med, 1985. **59**(3): p. 295-326.
107. Bloodgood, J.C., *WHEN CANCER BECOMES A MICROSCOPIC DISEASE, THERE MUST BE TISSUE DIAGNOSIS IN THE OPERATING ROOM.* Journal of the American Medical Association, 1927. **88**(13): p. 1022-1023.
108. Fischer, A.H., et al., *Preparation of Cells and and Tissues for Fluorescence Microscopy*, in *Basic methods in microscopy: protocols and concepts from cells : a laboratory manual*, D.L. Spector and R.D. Goldman, Editors. 2006, Cold Spring Harbor Laboratory Press: New York ; [Bloxham].
109. Fischer, A.H., et al., *Cryosectioning tissues.* CSH Protoc, 2008. **2008**: p. pdb prot4991.
110. Schwartz, S.A., M.L. Reyzer, and R.M. Caprioli, *Direct tissue analysis using matrix-assisted laser desorption/ionization mass spectrometry: practical aspects of sample preparation.* J Mass Spectrom, 2003. **38**(7): p. 699-708.
111. Vrana, M., et al., *An Optimized Method for Protein Extraction from OCT-Embedded Human Kidney Tissue for Protein Quantification by LC-MS/MS Proteomics.* Drug Metab Dispos, 2016. **44**(10): p. 1692-6.
112. Bullock, S., B. Balzer, and A.M. Marchevsky, *Guide to the Preparation of Frozen Sections*, in *Intraoperative consultation*, A.M. Marchevsky, F. Abdul-Karim, and B. Balzer, Editors. 2015, Saunders/Elsevier: Philadelphia, PA. p. 16-22.
113. Malakpour Permlid, A., et al., *Unique animal friendly 3D culturing of human cancer and normal cells.* Toxicol In Vitro, 2019. **60**: p. 51-60.
114. Brender, E., A. Burke, and R.M. Glass, *Frozen Section Biopsy.* JAMA, 2005. **294**(24): p. 3200-3200.
115. Lechago, J., *The frozen section: pathology in the trenches.* Arch Pathol Lab Med, 2005. **129**(12): p. 1529-31.
116. Spencer, L.T. and J.D. Bancroft, *7 - Microtomy: Paraffin and frozen*, in *Bancroft's Theory and Practice of Histological Techniques (Seventh Edition)*, S.K. Suvarna, C. Layton, and J.D. Bancroft, Editors. 2013, Churchill Livingstone: Oxford. p. 125-138.
117. Hira, V.V.V., et al., *Comparison of different methodologies and cryostat versus paraffin sections for chromogenic immunohistochemistry.* Acta Histochem, 2019. **121**(2): p. 125-134.
118. Pittaluga, S., T.S. Barry, and M. Raffeld, *Chapter 4 - Immunohistochemistry for the Hematopathology Laboratory*, in *Hematopathology*, E.S. Jaffe, et al., Editors. 2017, Elsevier: Philadelphia, PA. p. 41-52.
119. Maheshwari, A., et al., *Accuracy of intraoperative frozen section in the diagnosis of ovarian neoplasms: experience at a tertiary oncology center.* World J Surg Oncol, 2006. **4**: p. 12.
120. Winther, C. and N. Graem, *Accuracy of frozen section diagnosis: a retrospective analysis of 4785 cases.* APMIS, 2011. **119**(4-5): p. 259-62.
121. Adhikari, P., et al., *Accuracy of Frozen Section with Histopathological Report in an Institute.* JNMA J Nepal Med Assoc, 2018. **56**(210): p. 572-577.
122. Elshanbary, A.A., et al., *The diagnostic accuracy of intraoperative frozen section biopsy for diagnosis of sentinel lymph node metastasis in breast cancer patients: a meta-analysis.* Environ Sci Pollut Res Int, 2022. **29**(32): p. 47931-47941.

123. Ratnavelu, N.D., et al., *Intraoperative frozen section analysis for the diagnosis of early stage ovarian cancer in suspicious pelvic masses.* Cochrane Database Syst Rev, 2016. **3**: p. CD010360.
124. Hashmi, A.A., et al., *Accuracy of intraoperative frozen section for the evaluation of ovarian neoplasms: an institutional experience.* World J Surg Oncol, 2016. **14**: p. 91.
125. Lai, M. and B. Lü, *3.04 - Tissue Preparation for Microscopy and Histology*, in *Comprehensive Sampling and Sample Preparation*, J. Pawliszyn, Editor. 2012, Academic Press: Oxford. p. 53-93.
126. Zhang, W., et al., *Comprehensive proteome analysis of fresh frozen and optimal cutting temperature (OCT) embedded primary non-small cell lung carcinoma by LC-MS/MS.* Methods, 2015. **81**: p. 50-5.
127. Truong, J.X.M., et al., *Removal of optimal cutting temperature (O.C.T.) compound from embedded tissue for MALDI imaging of lipids.* Anal Bioanal Chem, 2021. **413**(10): p. 2695-2708.
128. Ferguson, R. and V. Subramanian, *Embryoid body arrays: Parallel cryosectioning of spheroid/embryoid body samples for medium through-put analysis.* Stem Cell Res, 2018. **28**: p. 125-130.
129. Xian, L., et al., *Genetic Engineering of Primary Mouse Intestinal Organoids Using Magnetic Nanoparticle Transduction Viral Vectors for Frozen Sectioning.* J Vis Exp, 2019(147).
130. Xie, P., et al., *Preparation of Frozen Sections of Multicellular Tumor Spheroids Coated with Ice for Mass Spectrometry Imaging.* Anal Chem, 2020. **92**(11): p. 7413-7418.
131. Klicks, J., et al., *A novel spheroid-based co-culture model mimics loss of keratinocyte differentiation, melanoma cell invasion, and drug-induced selection of ABCB5-expressing cells.* BMC Cancer, 2019. **19**(1): p. 402.
132. Priwitaningrum, D.L., et al., *Tumor stroma-containing 3D spheroid arrays: A tool to study nanoparticle penetration.* J Control Release, 2016. **244**(Pt B): p. 257-268.
133. Almeida, H., et al. *Exploring the MPTHub software for studying the transport of nanoparticles in native and surrogate mucus.* in *Oral and poster presentations at the 2022 Annual Meeting and Exposition of the Controlled Release Society.* July 11-15, 2022, Montreal, Canada.
134. Bauleth-Ramos, T., et al., *Colorectal cancer triple co-culture spheroid model to assess the biocompatibility and anticancer properties of polymeric nanoparticles.* J Control Release, 2020. **323**: p. 398-411.
135. Mukomoto, R., et al., *Oxygen consumption rate of tumour spheroids during necrotic-like core formation.* Analyst, 2020. **145**(19): p. 6342-6348.
136. Sbalzarini, I.F. and P. Koumoutsakos, *Feature point tracking and trajectory analysis for video imaging in cell biology.* J Struct Biol, 2005. **151**(2): p. 182-95.
137. Wilhelm, S., et al., *Analysis of nanoparticle delivery to tumours.* Nature Reviews Materials, 2016. **1**: p. 16014.
138. Jain, R.K. and T. Stylianopoulos, *Delivering nanomedicine to solid tumors.* Nat Rev Clin Oncol, 2010. **7**(11): p. 653-64.
139. Sindhwani, S., et al., *The entry of nanoparticles into solid tumours.* Nat Mater, 2020. **19**(5): p. 566-575.

140. Ruan, J.L., et al., *An improved cryosection method for polyethylene glycol hydrogels used in tissue engineering.* Tissue Eng Part C Methods, 2013. **19**(10): p. 794-801.
141. Jadhav, S.V., et al., *PVA and PEG functionalised LSMO nanoparticles for magnetic fluid hyperthermia application.* Materials Characterization, 2015. **102**: p. 209-220.
142. Ahmed, A.S., et al., *PVA-PEG physically cross-linked hydrogel film as a wound dressing: experimental design and optimization.* Pharm Dev Technol, 2018. **23**(8): p. 751-760.
143. Jabbari, E., *Hydrogels for Cell Delivery.* Gels, 2018. **4**(3).
144. Wohnhaas, C.T., et al., *DMSO cryopreservation is the method of choice to preserve cells for droplet-based single-cell RNA sequencing.* Sci Rep, 2019. **9**(1): p. 10699.
145. Dong, H., et al., *Cryopreserved Spontaneous Spheroids from Compact Bone-Derived Mesenchymal Stromal Cells for Bone Tissue Engineering.* Tissue Eng Part C Methods, 2021. **27**(4): p. 253-263.
146. Ma, X.H., et al., *Slow-freezing cryopreservation of neural stem cell spheres with different diameters.* Cryobiology, 2010. **60**(2): p. 184-91.
147. Ehrhart, F., et al., *A comparative study of freezing single cells and spheroids: towards a new model system for optimizing freezing protocols for cryobanking of human tumours.* Cryobiology, 2009. **58**(2): p. 119-27.
148. *Collection, Storage, Retrieval and Distribution of Biological Materials for Research.* Cell Preservation Technology, 2008. **6**(1): p. 3-58.
149. Campbell, L.D., et al., *Development of the ISBER Best Practices for Repositories: Collection, Storage, Retrieval and Distribution of Biological Materials for Research.* Biopreserv Biobank, 2012. **10**(2): p. 232-3.
150. Danaei, M., et al., *Impact of Particle Size and Polydispersity Index on the Clinical Applications of Lipidic Nanocarrier Systems.* Pharmaceutics, 2018. **10**(2).
151. Clarke, S.P. *Development of Hierarchical Magnetic Nanocomposite Materials for Biomedical Applications*. 2013.
152. Nunes, R., et al., *Surface modification with polyethylene glycol enhances colorectal distribution and retention of nanoparticles.* Eur J Pharm Biopharm, 2018. **130**: p. 200-206.
153. Suh, J., D. Wirtz, and J. Hanes, *Efficient active transport of gene nanocarriers to the cell nucleus.* Proc Natl Acad Sci U S A, 2003. **100**(7): p. 3878-82.
154. Guarnieri, D., et al., *Effect of serum proteins on polystyrene nanoparticle uptake and intracellular trafficking in endothelial cells.* Journal of Nanoparticle Research, 2011. **13**(9): p. 4295-4309.

# Annex

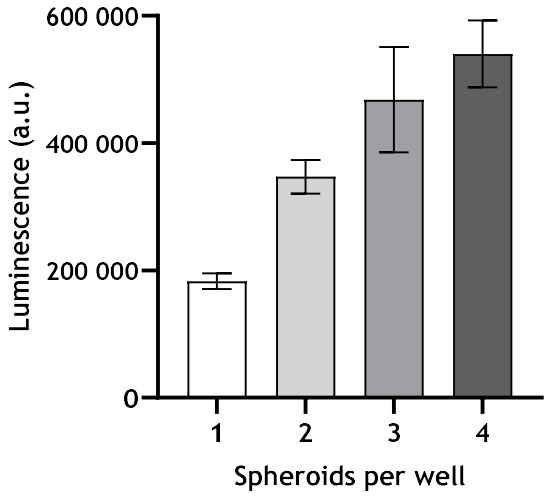


**Annex Figure A1** – Calibration curve of MCTS viability using CellTiter-Glo®. According to the manufacturer, there should be a linear increase between the number of cells and the luminescence captured, to guarantee no over/undersaturation. Though this linearity is present between 1 and 3 spheroids per well, 4 MCTS per well do not produce the expected signal. Therefore, 2 spheroids per well appears to be the best cellular concentration, as it guarantees a good signal while preserving linearity between cell number and luminescence.

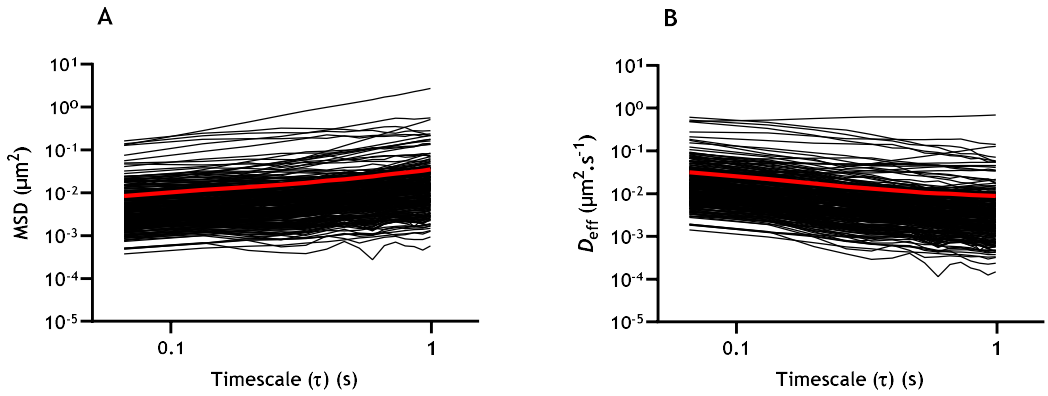


**Annex Figure A2** – Individual (A) MSD and (B) $D_{eff}$ of bare NPs (335 tracked particles) incubated with whole spheroids since cell seeding (bare SS), as a function of time scale. Ensemble values are also presented in red in both graphs.

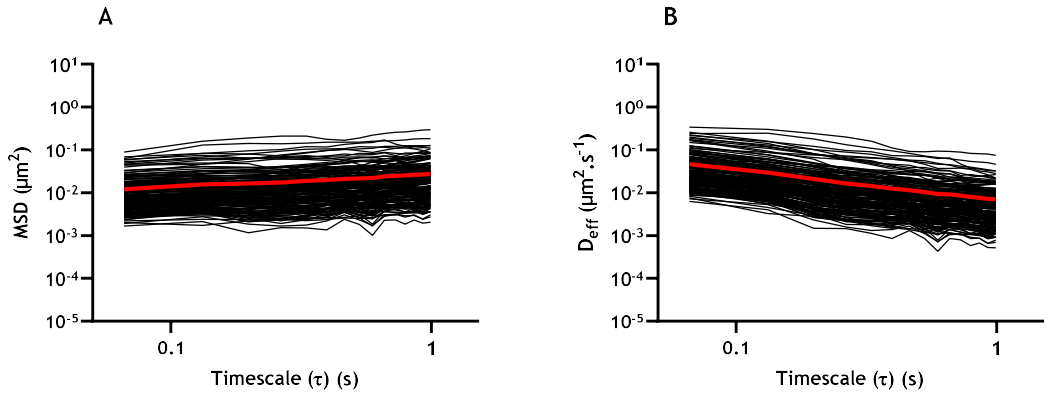


**Annex Figure A3** – Individual (A) MSD and (B) $D_{eff}$ of P407-coated NPs (168 tracked particles) incubated with spheroids since cell seeding (P407 SS), as a function of time scale. Ensemble values are also presented in red in both graphs.

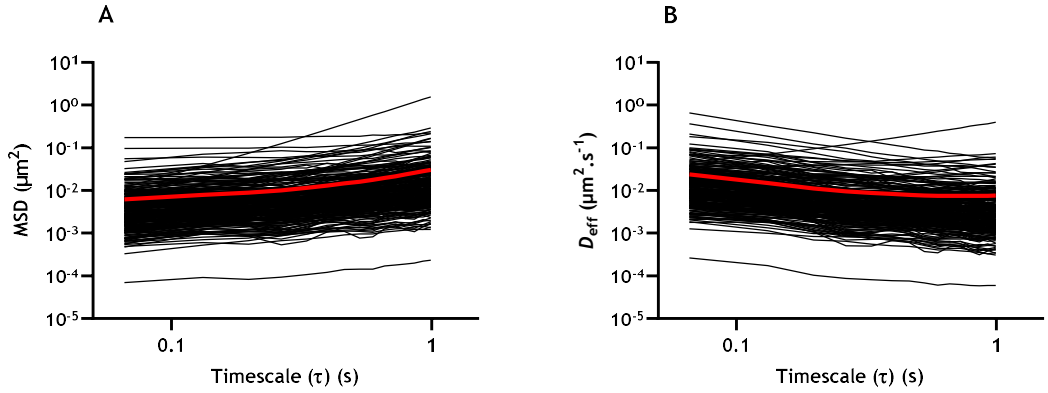


**Annex Figure A4** – Individual (A) MSD and (B) $D_{eff}$ of bare NPs (260 tracked particles) incubated with whole spheroids for 6 h before microscopic observation (bare BO), as a function of time scale. Ensemble values are also presented in red in both graphs.

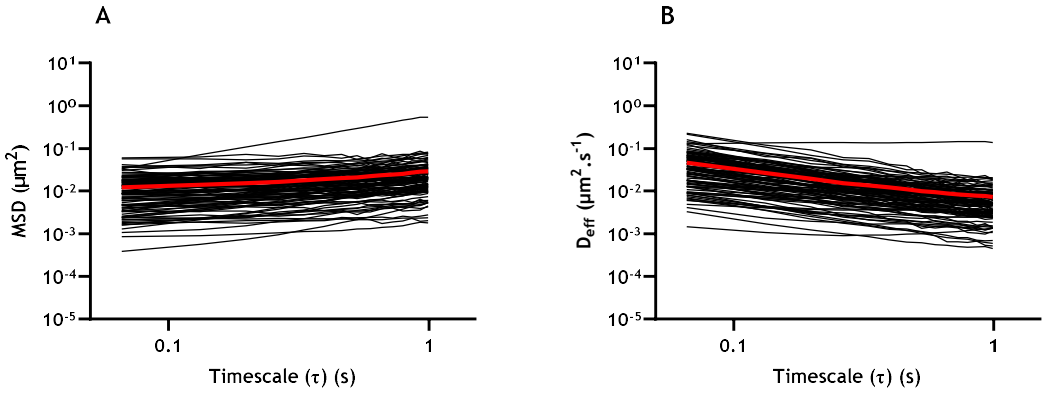


**Annex Figure A5** – Individual (A) MSD and (B) $D_{eff}$ of P407-coated NPs (104 tracked particles) incubated with whole spheroids for 6 h before microscopic observation (P407 BO), as a function of time scale. Ensemble values are also presented in red in both graphs.

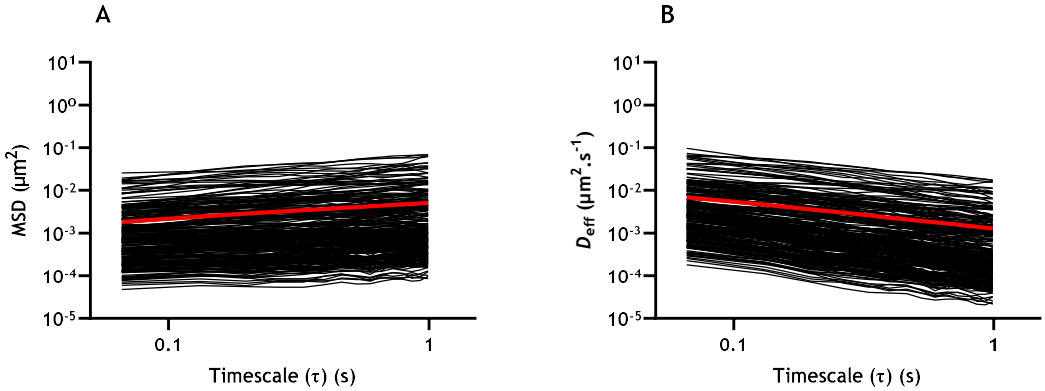


**Annex Figure A6** – Individual (A) MSD and (B) $D_{eff}$ of bare NPs (≥100 tracked particles per experiment, *n* = 3) in MCTS cryosections after incubation with whole spheroids since cell seeding (bare SS), as a function of time scale. Ensemble values are also presented in red in both graphs.

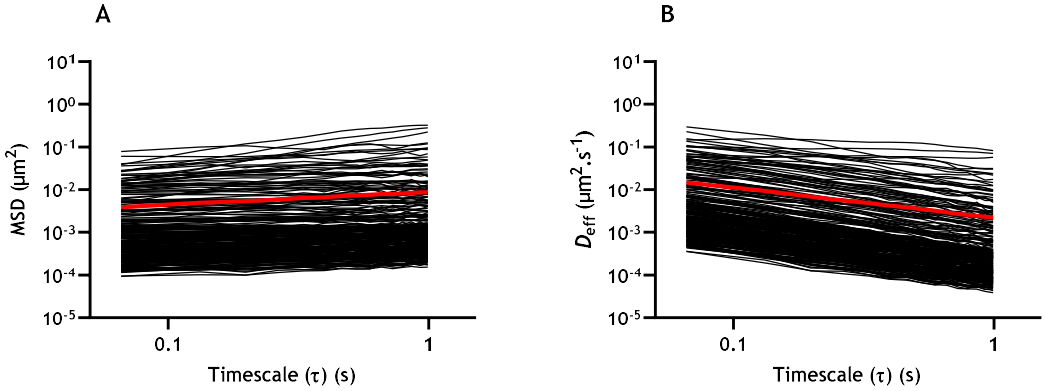


**Annex Figure A7** – Individual (A) MSD and (B) $D_{eff}$ of P407-coated NPs (≥100 tracked particles per experiment, *n* = 3) in MCTS cryosections after incubation with whole spheroids since cell seeding (P407 SS), as a function of time scale. Ensemble values are also presented in red in both graphs.

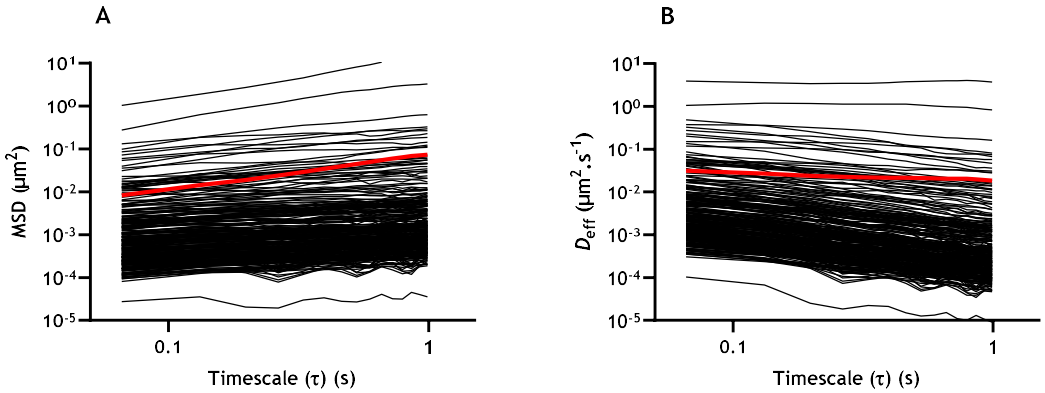


**Annex Figure A8** - Individual (A) MSD and (B) $D_{eff}$ of bare NPs (≥100 tracked particles per experiment, *n* = 3) in MCTS cryosection after incubation with whole spheroids for 6 h before microscopic observation (bare BO), as a function of time scale. Ensemble values are also presented in red in both graphs.

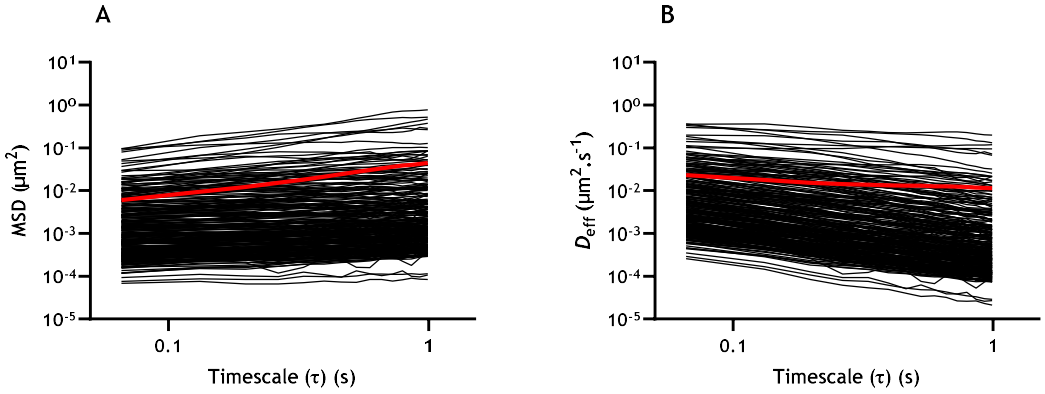


**Annex Figure A9** - Individual (A) MSD and (B) $D_{eff}$ of P407-coated NPs (≥100 tracked particles per experiment, *n* = 3) in MCTS cryosections after incubation with whole spheroids for 6 h before microscopic observation (P407 BO), as a function of time scale. Ensemble values are also presented in red in both graphs.

**Annex Table A1** – Number of trajectories analysed for each condition when assessing the movement of NPs in the distinct spheroid layers.

| Condition | NP | Spheroid Layer | | |
|---|---|---|---|---|
| | | Border | Inner | Centre |
| SS | Bare | 96 | 132 | 82 |
| | P407 | 102 | 114 | 92 |
| BO | Bare | 182 | 97 | 30 |
| | P407 | 181 | 92 | 30 |

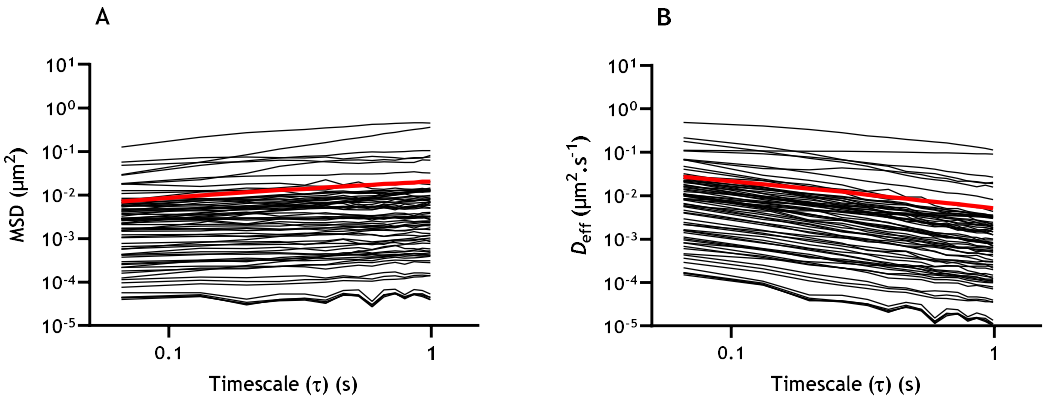


**Annex Figure A10** – Individual (A) MSD and (B) $D_{eff}$ of covalently-bound PEGylated NPs in MCTS cryosections after incubation with whole spheroids since cell seeding (PEG SS), as a function of time scale ($n$ = 72). Ensemble values are also presented in red in both graphs.

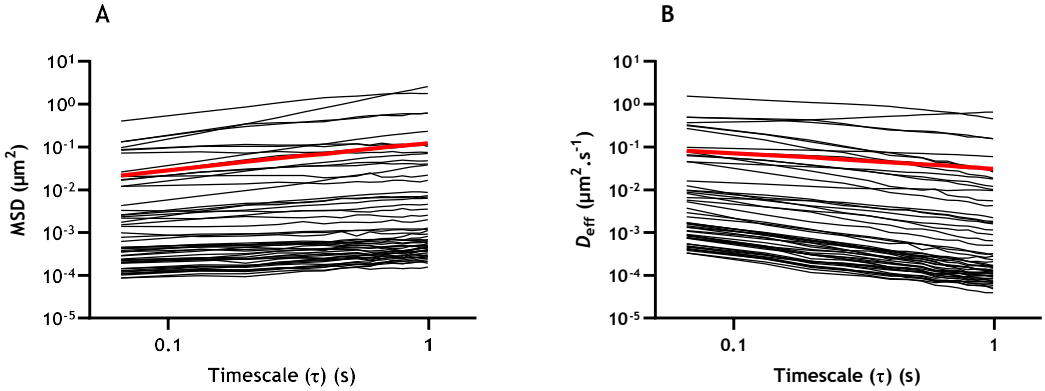


**Annex Figure A11** – Individual (A) MSD and (B) $D_{eff}$ of covalently-bound PEGylated NPs in MCTS cryosections after incubation with whole spheroids for 6 h before microscopic observation (PEG BO), as a function of time scale ($n$ = 54). Ensemble values are also presented in red in both graphs.